Biophysical Characterisation of LcrH, a Class II Chaperone of the Type III Secretion System

Sunny Kumar Singh

A thesis submitted for the degree of Doctor of Philosophy (Chemistry) at the University of Sussex

September 2015

Declaration

I hereby declare that this thesis has not been and will not be, submitted in whole or in part to another University for the award of any other degree.

Signed:

Sunny Kumar Singh, 18th September 2015

In memory of my Grandfather, Grandmother and Father

''It does not matter how slowly you go as long as you do not stop.''

- **Confucius**

Acknowledgements

First and foremost I thank my supervisor Prof Louise Serpell. I could not have come this far without your support and kindness. I am grateful to the University of Sussex for funding this project. I do not think I can thank Dr Ewan Main enough. Not because of the standard polite gratitude that needs to be given to PhD supervisors in acknowledgements but because I truly am indebted to you. You provided me with the opportunity to work, helped me get through the tough times of recurring illnesses and had the patience of letting me stick around for what now seems like centuries. I also acknowledge my co-supervisor Dr Darren Thompson for his support, laboratory equipment and amusing anecdotes.

I thank Prof Andrew Smith and his group in former lab 13, Chemistry, University of Sussex especially Dr Wendy Doyle for her advice on molecular biology which was instrumental in kick-starting my project. Additionally, I thank Dr Yalda Javadi, Dr Maria Karatsa-Dodgson and Dr Sarah Pannell for education on instrumentation, techniques and inspiration.

I have cherished the time spent both inside the lab and out with my dear friends Dr Jonathan (JJ) Phillips and Dr. Charlotte Millership both in Sussex and in London. I will never forget our culinary gatherings.

An enormous thanks to Dr Ruth-Sarah Rose for her support during my time at QMUL. She trained me for using various instruments and provided invaluable help in the composition of my thesis. Without her guidance I would not have accomplished this. I am grateful to Kelly Clark largely for her hospitality but also for the initiation into British culture.

I thank the members past and present of office 4.36 in G.E. Fogg building at QMUL especially Dr Erica Belgio, Anna Yates, Dr Helen Marks, Dr Tatiana Novoselova and Dr Christopher Duffy. There are many others, too numerous to mention but your contribution and support is no less significant. Also, the members of G35 in the Joseph Priestly Building at QMUL, in particular Dr Nadine Younan for her expertise regarding CD.

I am deeply indebted to my friends Inderjeet, Souvik, Anirban, Srijit, Mahesh and Tina. You made me feel at home away from home. Your companionship gave me the courage to fight against all odds and crawl out of deep despair. I would not have survived without you all.

Without my late Grandfather, this journey would not have been possible. It was his encouragement and sacrifice that allowed me to come to the UK and pursue my passion. I am overwhelmed by the selfless love from my mother who has taken care of me single-handedly in the absence of my father. I have no words to thank my little brother who has taken care of my family in Mumbai in my absence and has helped me pay all of my debts. The love from my cousins and extended family has continued to feed my enthusiasm for my career in science. No one has ever pursued science in my family so I thank you for your support, even if it does make it so much harder for me to explain what I've done. I hope I have made you proud.

Summary

The type three-secretion system (T3SS) is a large and complex protein nano-machine that many gram-negative pathogens employ to infect host cells. A key structure of this machine is a proteinaceous pore that inserts into the target membrane and forms a channel for bacterial toxins to flow from bacteria into the host cell. The pore is mainly formed from two large membrane proteins called “translocators”. Importantly, effective secretion and thus pore formation of the translocators depends on their binding to and being transported by small specialized chaperones after synthesis in the bacterial cytosol. Recent crystal structures have shown these chaperones are formed from modular tetratricopeptide repeats (TPRs). However, each crystal structure produced different homodimeric structures, suggesting flexibility in their topology that may be of importance to function.

Given the crucial role of the translocator chaperones, we investigated the conformational stability of the chaperone LcrH (*Yersinia pestis*). Mutational analysis coupled with analytical ultra-centrifugation and equilibrium chemical denaturations showed that LcrH is a weak and thermodynamically unstable dimer (K_D ≈ 15 μM, $\Delta \boldsymbol{G}_{H_2O}$ = 7.4 kcalmol^{-1}). The modular TPR structure of the dimer allows it to readily unfold in a non-cooperative manner to a one-third unfolded dimeric intermediate ($\Delta \boldsymbol{G}_{H_2O}$ = 1.7 kcalmol^{-1}), before cooperatively unfolding to a monomeric denatured state ($\Delta \boldsymbol{G}_{H_2O}$ = 5.7 kcalmol^{-1}). Thus under physiological conditions the chaperone is able to populate C-terminally unravelled partially folded states, whilst being held together by its dimeric interface. Such ability suggests a “fly-casting” mechanism as a route to binding their far larger translocator cargo.

Abbreviations

ABC	ATP binding cassette
Amp	Ampicillin
Amp^R	Ampicillin resistance
A. tumefaciens	*Agrobacterium tumefaciens*
AUC	Analytical ultracentrifugation
bp	base pair
CBD	Chaperone binding domain
CD	Circular dichroism
cm	Centimetre
DLS	Dynamic light scattering
dNTP	Deoxyribonucleotide triphosphate
DTT	$_{D\text{-}L}$-Dithiothreitol
E. coli	*Escherichia coli*
EDTA	Ethylenediaminetetraacetate
fl-LcrH	Full length LcrH
FPLC	Fast purification liquid chromatography
g	Grams
Gdm	Guanidinium
GPS	General secretory pathway
GST	Glutathione S-transferase
Hcp	Haemolysin coregulated protein

IM	Inner membrane
IPTG	Isopropyl-β-$_D$-thiogalactopyranoside
ITC	Isothermal titration calorimetry
kb	kilo base
LB	Luria-Bertani broth
lb/in^2	pounds per square inch
LcrH	Low calcium response protein H
L65E tr-LcrH	Truncated LcrH carrying the L65E mutation
LPS	Lipopolysaccharide
mdeg	Millidegree
MFP	Membrane fusion protein
MS	Inner membrane ring (T3SS)
OM	Outer membrane
OMP	Outer membrane pore forming protein
P. aeruginosa	*Pseudomonas aeruginosa*
PAGE	Polyacrylamide gel electrophoresis
PBS	Phosphate buffered saline
PCR	Polymerase chain reaction
PDB	Protein data bank
PP	Periplasm
SDS	Sodium dodecyl sulphate
SEC	Size exclusion chromatography

SRP	Signal recognition particle
T1SS	Type I Secretion System
T2SS	Type II Secretion System
T3SS	Type III Secretion System
T4SS	Type IV Secretion System
T5SS	Type V Secretion System
T6SS	Type VI Secretion System
Tat	Twin-arginine translocation
TEMED	N,N,N',N'-tetramethylethylenediamine
TPR	Tetratricopeptide repeat
Tris	Trizma base
tr-LcrH	truncated LcrH
T_m	Melting temperature
UV-Vis	Ultraviolet-visible
V. cholera	*Vibrio cholera*
Y. enterocolitica	*Yersinia enterocolitica*
Y. pestis	*Yersinia pestis*

Table of Contents

CHAPTER 1 INTRODUCTION....16

1.1 SYMBIOSIS, PATHOGENESIS & COMMENSALISM....16

1.2 GRAM POSITIVE AND GRAM NEGATIVE BACTERIA....17

1.3 PROTEIN SECRETION BY BACTERIA....18

1.3.1 SECRETION THROUGH THE INNER MEMBRANE....19

1.3.1.1 The Sec Pathway....19

1.3.1.2 Signal Recognition Particle (SRP)....20

1.3.1.3 The Tat System....20

1.3.2 GRAM-NEGATIVE BACTERIAL SECRETION SYSTEMS....20

1.3.2.1 Type I Secretion System (T1SS)....21

1.3.2.2 Type II Secretion System (T2SS)....22

1.3.2.3 Type III Secretion System (T3SS)....24

1.3.2.4 Type IV Secretion System (T4SS)....25

1.3.2.5 Type V Secretion System (T5SS)....26

1.3.2.6 Type VI Secretion System....28

1.3.3 TYPE THREE SECRETION SYSTEM IN DETAIL....31

1.3.3.1 The role of Chaperones in the T3SS....40

1.3.3.2 Class I Chaperones....40

1.3.3.3 Class II & III Chaperones....44

1.3.3.4 Structure and biophysical characterisation of Class II Chaperones....48

1.3.3.5 Structure and biophysical characterisation of Class III Chaperones....53

1.4 THESIS AIMS....56

CHAPTER 2 MATERIALS AND METHODS....57

2.1 MOLECULAR BIOLOGY METHODS....57

2.1.1 *FL-LCRH* GENE SYNTHESIS....57

2.1.1.1 Recursive PCR....57

2.1.1.1.1 Agarose Gel Electrophoresis....58

2.1.1.2 Polymerase Chain Reaction (PCR)....58

2.1.2 INSERTION OF SYNTHESISED *LCRH* GENE INTO A CLONING VECTOR....59

2.1.2.1 Cloning of *l-LcrH* gene into TOPO TA cloning vector....59

2.1.2.1.1 Poly-A tailing with Taq polymerase....59

2.1.2.1.2 Ligation for TOPO TA cloning....60

2.1.2.1.3 Transformation of Ligated *fl-LcrH* in chemically competent cells....60
2.1.2.1.4 DNA extraction and purification....61
2.1.2.1.5 Estimation of DNA concentration....61
2.1.2.1.6 Analytical Restriction Digestion with EcoRI....62
2.1.2.1.7 DNA sequencing....62
2.1.3 INSERTION OF SYNTHESISED *FL-LCRH* GENE INTO AN EXPRESSION VECTOR....62
2.1.3.1 Restriction digest of *fl-LcrH* gene....63
2.1.3.2 Purification of DNA from an Agarose Gel....64
2.1.3.3 Ligation....64
2.1.3.4 Transformation using Electro-competent cells....64
2.1.3.5 Confirmation of DNA Clones....65
2.1.4 SYNTHESIS & INSERTION OF TRUNCATED *LCRH* (*TR-LCRH*) GENE IN INTO PTRC-GST VECTOR....65
2.1.5 SYNTHESIS OF LE65 MUTANT OF TR-LCRH....66
2.1.5.1 Site Directed Mutagenesis....66
2.2 PROTEIN PRODUCTION AND PURIFICATION....67
2.2.1 PROTEIN PRODUCTION....67
2.2.1.1 Cell Lysis for Protein Extraction....68
2.2.1.1.1 Cell Lysis by Sonication....68
2.2.1.1.2 Cell Lysis by Homogenisation....68
2.2.1.2 Purification by Affinity Chromatography....68
2.2.1.3 Buffer Solutions....69

NAME OF BUFFER....**69**

HIS-TAG WASH BUFFER....**69**

HIS-TAG ELUTION BUFFER....**69**

GST WASH BUFFER....**69**

GST ELUTION BUFFER....**69**

2.2.1.4 Ni^{2+} Affinity chromatography and cleavage of His-tagged proteins....69
2.2.1.5 GST Affinity purification and cleavage of GST-tagged proteins....70
2.2.1.6 Purification using Size Exclusion Chromatography by AKTA FPLC....70
2.2.2 PROTEIN PURITY....70
2.2.2.1 Mass Spectrometry....71

SAMPLE AND MATRIX PREPARATION 71

2.2.2.2 SDS-Polyacrylamide Gel Electrophoresis 71

2.2.3 DETERMINATION OF PROTEIN CONCENTRATION 71

2.2.4 STORAGE OF PURIFIED PROTEIN 72

2.3 BIOPHYSICAL CHARACTERIZATION OF LCRH PROTEINS 72

2.3.1 MULTIMERIC STATE OF LCRH PROTEINS USING ANALYTICAL SIZE EXCLUSION CHROMATOGRAPHY (SEC) 72

2.3.2 ANALYTICAL ULTRACENTRIFUGATION (AUC) 73

2.3.3 DYNAMIC LIGHT SCATTERING (DLS) 75

2.4 SECONDARY AND TERTIARY STRUCTURE CHARACTERIZATION 76

2.4.1 CIRCULAR DICHROISM (CD) SPECTROSCOPY 76

2.4.2 FLUORESCENCE SPECTROSCOPY 77

2.5 EQUILIBRIUM STUDIES FOR MEASURING THERMODYNAMIC STABILITY 78

2.5.1 GENERAL BACKGROUND 78

2.5.2 EQUIPMENT AND GENERAL PROCEDURES 79

2.5.3 PREPARATION OF SAMPLES FOR EQUILIBRIUM CHEMICAL DENATURATION 79

2.5.3.1 Sample preparation for LcrH protein concentrations 1 to 12 µM 80

2.5.3.2 Sample preparation for LcrH protein concentrations 25 to 80 µM 80

CHAPTER 3 GENE CONSTRUCTION, PURIFICATION STRATEGY AND INITIAL BIOPHYSICAL CHARACTERISATION OF LCRH PROTEINS 81

3.1 INTRODUCTION 81

3.2 EXPERIMENTAL APPROACHES 81

3.3 RESULTS 82

3.3.1 FULL LENGTH LCRH (FL-LCRH) GENE CONSTRUCTION 82

3.3.2 PRODUCTION AND PURIFICATION OF FULL LENGTH LCRH (FL-LCRH) 83

3.3.3 TRUNCATED LCRH (TR-LCRH) 88

3.3.4 EXPRESSION & PURIFICATION OF TRUNCATED LCRH (TR-LCRH) 91

..... 91

3.3.5 CONSTRUCTION OF L65E TR-LCRH 92

3.3.6 EXPRESSION AND PURIFICATION OF L65E TR-LCRH 93

3.3.7 INITIAL CHARACTERIZATION OF LCRH CONSTRUCTS 94

3.3.7.1 Defining buffer & protein concentrations to maintain “native” oligomeric states of LcrH constructs 94

3.3.7.2 Far-UV circular dichroism of native LcrH constructs 97
3.3.8 Conclusion 98

CHAPTER 4 OLIGOMERIC STATE, FLEXIBILITY AND THERMODYNAMIC STABILITY OF LCRH PROTEIN CONSTRUCTS 99

4.1 Introduction 99
4.2 Experimental Approaches 99
4.3 Results 99
4.3.1 Oligomeric States of LcrH using Analytical Size Exclusion Chromatography (SEC) 99
4.3.2 Determination of Dimerization Dissociation Constant (K_D) using Analytical Ultracentrifugation (AUC) 102
4.3.2.1 Calculating percentage of dimer at a given protein concentration 103
4.3.3 Loss of LcrH's α-Helical Structure on N-terminal Deletion & Concentration Reduction 106
4.3.4 Equilibrium Unfolding and Thermodynamic Stability of LcrH 107
4.3.4.1 The Best Structural Probe to Monitor Chemical Denaturation 107
4.3.4.2 Determining the most suitable chemical denaturant 111
4.3.4.3 Minimum Equilibration Time for Equilibrium Chemical Denaturation 114
4.3.4.4 The Reversibility of Equilibrium Unfolding 115
4.3.5 Equilibrium Chemical Denaturation of LcrH's Protein Constructs 116
4.3.5.1 Biphasic Denaturations Show LcrH Unfolds via Partially Folded Dimeric Intermediate 118
4.3.5.2 Deletion of N-terminus Causes No Change in Equilibrium Unfolding 122
4.3.6 Thermodynamic stability of LcrH 122
4.3.6.1 Data analysis 123
4.3.6.2 Proposed equilibrium unfolding pathway: 126
4.3.6.3 Thermodynamic Stability of Monomeric vs Dimeric LcrH 127
4.3.7 Conclusion 129

CHAPTER 5 CONCLUSIONS 130

5.1 Future work 133

CHAPTER 6 BIBLIOGRAPHY 134

Chapter 1 Introduction

Life on earth can be categorised in numerous ways. One method classifies the diverse array of organisms on our planet through their biochemical characteristics. This method divides organisms into three distinct groups called domains:

(i) *Eukarya* (eukaryotes) – Eukarya consist of all macroscopic organisms including human beings as well as many microscopic, unicellular organisms such as yeast. The most important characteristic of *eukaryotes* is the presence of a well-defined nucleus within each cell.

(ii) *Bacteria* – These are unicellular organisms lacking a nucleus, and are referred to as *prokaryotes.* They constitute a large domain of prokaryotic microorganisms. Bacteria were among the first life forms to appear on Earth, and are present in most of its habitats.

(iii) *Archaea* – Carl Woese first discovered these organisms in 1977 and classified them as prokaryotes as they were bacteria-like. However, they are biochemically quite distinct from bacteria. These distinctions include: archaea have cell membrane containing ether linkages, cell walls that lack peptidoglycan and have genes and enzymes that behave more like eukaryotes. Thus they were reclassified as a domain of their own [1-3].

This thesis is concerned with the biochemical methods employed by certain bacteria to survive in and around higher multicellular organisms (humans).

1.1 Symbiosis, Pathogenesis & Commensalism

There are three distinct types of relationship between bacteria and higher multicellular organisms. They can live in symbiosis, as commensals or as pathogens. Symbiosis occurs when two organisms obtain a mutually beneficial relationship with one another [4-6]. For example, many bacteria are vital for the maintenance of homeostasis in higher organisms. The human gut hosts an estimated 500-1000 species of bacteria [1,3,7,8]. Here, the human intestine provides nutrients to the resident bacteria, whereas bacteria help in the digestion of food, absorption of nutrients, production of vitamins such as biotin and vitamin K, regulation of the immune system, and prevention of colonization of pathogenic microorganisms [4,6,9].

In contrast, pathogenesis occurs when one organism gains advantage to the detriment of the other. Bacteria are another excellent example of this interaction, with many attacking higher organisms by damaging cell tissues in the search for nutrients. For example, *Yersinia pestis* is the causative agent of bubonic plague and many *Shigella* species cause dysentery [7,8,10].

In between the two extremes of symbiosis and pathogenesis lie commensals. Commensalism is an association between two different species where one enjoys benefit and the other is not significantly affected [9,11]. Commensal bacteria are found on all animal body surfaces as part of normal microbial flora. However, under specific conditions such commensals can turn pathogenic and exert pathologic effects on the host organism [10,12]. For example, *Staphylococcus aureus* normally colonises human skin without causing any harm. However if the epidermis of the skin is broken they can cause skin infection and more serious complaints. Recently, there has been an emergence of antibiotic resistant forms of *S. aureus* (MRSA: Methicillin resistant *S. aureus*), making it a significant health risk [11,13].

1.2 Gram Positive and Gram Negative Bacteria

Bacteria can be separated into two groups on the basis of their Gram staining: Gram-positive and Gram-negative (Figure 1.1). This simple staining process has lasted into our high-technology era as a useful tool for identifying bacteria. The Danish physician Hans Christian Gram developed it in 1884. A smear of bacterial cells on a microscope slide is soaked in a violet dye and treated with iodine; it is then washed with alcohol and counterstained with saffranine (a red dye). Gram-positive bacteria retain the violet dye and appear blue to purple. The alcohol washes the violet stain out of Gram-negative cells; these cells then pick up the saffranine counterstain and appear pink to red. For many bacteria, the Gram-staining results compare roughly with the cell wall structure. In Gram-positive bacteria, peptidoglycan forms a thick layer outside the plasma membrane. Whereas, the Gram-negative cell wall has only one-fifth as much peptidoglycan. In order to provide additional protection for Gram-negative bacteria, outside the peptidoglycan layer, a second, outer membrane quite distinct in chemical

makeup from the plasma membrane surrounds the cell. Between the inner and outer membranes of Gram-negative bacteria is an additional periplasmic space. This space contains enzymes important in digesting specific molecules, transporting others, and detecting chemical gradients in the environment [2,12].

Interestingly, common causes of infections are Gram-negative bacterial pathogens. The prevalence and the rate of resistance among these pathogens to existing anti-microbial agents is on the rise [12,13]. The pathogenicity of gram-negative bacteria is often associated with the lipopolysaccharide (LPS) layer present in the outer membrane. The chemical structure of the LPS layer is often unique to particular bacterial strains (*i.e*. sub-species) and is responsible for many of the antigenic properties of these strains [2,14].

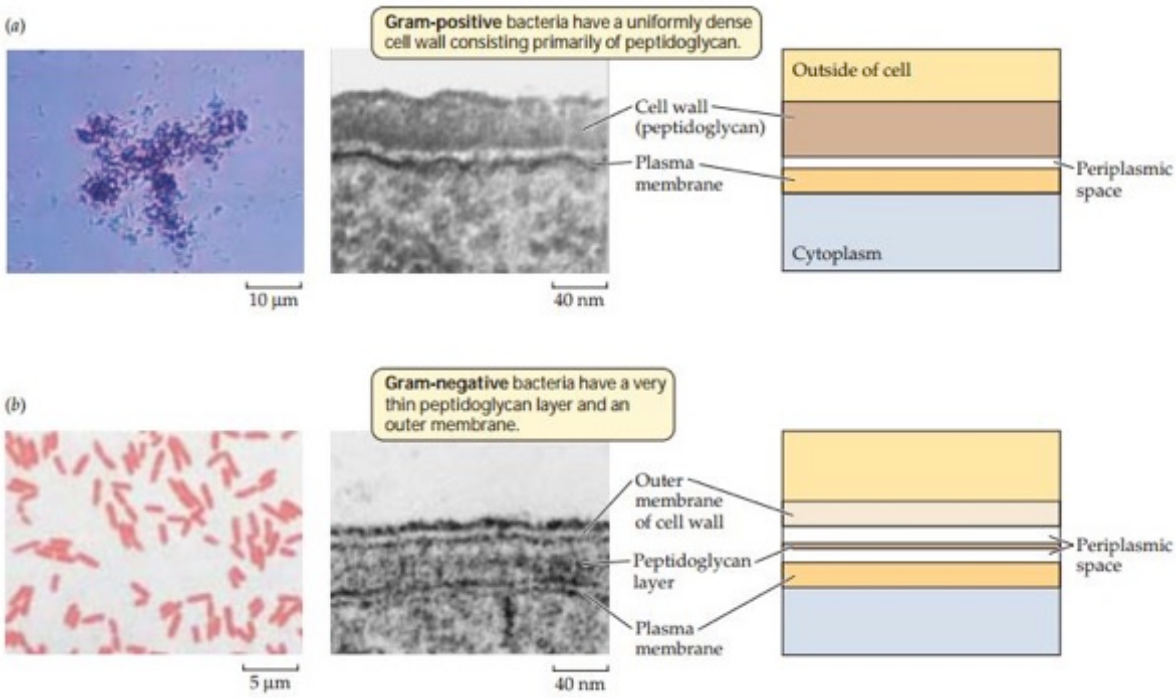

Figure 1.1 Gram staining and the bacterial cell wall: when treated with Gram stain, the cell wall components of different bacteria react in one of two ways. (a) Gram positive bacteria have a thick peptidoglycan cell wall that retains the violet dye and appears blue or purple. (b) Gram negative bacteria have a thin peptidoglycan layer that does not retain the violet dye, but picks up the counterstain and appears pink-red. Figure was taken from [12,15].

1.3 Protein secretion by bacteria

The cytoplasm of the bacterial cell is isolated from the external environment by a phospholipid bilayer termed as the plasma membrane. In order to interact with the environment and for its sustenance it becomes essential for the bacterium to export

elements from its cytosol to the external milieu and *vice versa*. Until the 1960s, protein secretion across the bacterial membrane was thought to be a rare phenomenon. It was believed that secretion occurred in a protein specific manner [14,16]. This view was dismissed following the discovery of numerous systems dedicated to the transport of proteins across the plasma membrane. Furthermore, in the case of Gram-negative bacteria, proteins are transported through the periplasm and the outer membrane. These secretory systems export proteins either to be attached outside the bacterial cell surface, released into the external environment, or in some cases even directly into the cytoplasm of other cells.

1.3.1 Secretion through the inner membrane

The first challenge faced by a bacterial cell is the transportation of protein molecules across the inner plasma membrane, irrespective of whether it a Gram-positive or Gram-negative bacteria. Protein molecules travel across this barrier with the help of membrane embedded protein transport systems. These proteins then enter the periplasm or they get inserted into the membrane. There is a remarkable array of protein transport systems found in bacteria, of which three are present in most bacterial species: The Sec (general secretory pathway or GSP), signal recognition particle (SRP) and twin-arginine translocation (Tat) pathways [15,17].

1.3.1.1 The Sec Pathway

The Sec pathway is formed by the interaction of a numerous proteins, which are conserved both in prokaryotes and eukaryotes (known as the Sec 61 complex, where it transports proteins across the endoplasmic reticulum [16,18]. In particular, the Sec system is involved in the secretion of unfolded proteins across the cytoplasmic membrane and the insertion of membrane proteins into the cytoplasmic membrane [17,19]. To perform the transport, three proteins SecY, SecE & SecG (SecYEG) form a heterotrimeric integral membrane complex. SecA is then recruited to the complex, by binding to SecY on the bacterial cytoplasmic side. SecA has ATPase activity and acts as a motor to drive secretion [18,20]. SecB binds the protein requiring transport and delivers it to SecA. Once bound to SecA, ATP is used to release the cargo of SecB to SecA and translocate the cargo through the membrane [19,21-23].

1.3.1.2 Signal Recognition Particle (SRP)

The SRP is very similar to the Sec pathway, in as much as they use the same complex SecY, SecE, SecG (SecYEG). However it does not use SecA and SecB to drive secretion or recruit cargo. Instead the SRP molecule is recruited to the ribosome to bind newly formed proteins that need to be membrane bound by ribosome-nascent chain (RNC) complex [20,24]. The SRP+RNC complex then targets the protein SRP receptor FtsY which in turn directs it to the SecYEG machinery [21-23,25].

1.3.1.3 The Tat System

The Sec pathway is the universally conserved pathway in prokaryotes. However, there also exists the Tat pathway. This system is found in some bacteria and has been identified as essential in only a few organisms. Nevertheless, the Tat system plays a significant role in some cellular processes such as iron and phosphate acquisition in *E. coli* and *Salmonella spp.* The Sec pathway is employed for the transportation of unstructured proteins across the bacterial plasma membrane. In contrast, the Tat pathway is used for the transportation of folded proteins. Proteins are identified for transport through the Tat system via a signal peptide containing a twin arginine repeat motif [24,26].

The Tat system comprises of two inner membrane integrated subunits *i.e.* TatA and TatC. In some bacterial systems, there are multiple copies of components of the Tat system. For example, *Bacillus subtilis* has two copies of *tatC* and three copies of *tatA* [25,27] whilst a few organisms such as *E. coli employ* an additional protein TatB.

1.3.2 Gram-negative Bacterial Secretion Systems

Secretion across the outer membrane is a process specifically undertaken by Gram-negative bacteria. In order to achieve this task Gram-negative bacteria have evolved a series of mechanisms which allow them to either export proteins as a two-step process, exploiting one of the methods mentioned above to export the protein across the inner membrane, or as a one step process, where the protein is exported from the cytosol to outside of the cell without any intermediate steps. The mechanisms available to accomplish this task are named, in a simple numerical manner. There are

at present six major systems that are well described: the type I-VI secretion systems. The following sections briefly describe each of those systems.

1.3.2.1 Type I Secretion System (T1SS)

Type-I secretions systems (T1SS) allow for the movement of proteins from the cytoplasm to outside of the cell in a one-step manner, utilising a simple system of just three proteins. These three proteins are an ATP-binding cassette (ABC) transporter, a membrane fusion protein (MFP) and an outer membrane pore forming protein (OMP) [26-28] (see Figure 1.2). The ABC protein consists of a cytoplasmically located nucleotide binding domain, and a transmembrane domain produced from six α-helices [27,29]. ABC proteins characteristically function as homodimers or trimers in producing a functional pore through which the secreted protein can pass through [27,28,30]. Additionally, ABC protein provides substrate specificity to the secretion machinery [29,31]. The MFPs interact in a trimeric fashion with the ABC proteins in order to create a periplasmic channel through which the secreted protein can traverse [30,32].

It has been suggested that the binding of substrates to the ABC protein leads to a conformational change in the MFP, such that it interacts with the OMP to complete the channel to the external environment [31,33]. However, the exact mechanism of this interaction remains unclear [32,34]. The OMP, as characterised by the TolC protein from *E. coli* exists as a trimer anchored in the outer membrane by a β-barrel structure [26,33]. It has been shown that the ABC and OM proteins can interact together directly, although this interaction *in vivo* requires the presence of the MFP [34-37].

There are a wide variety of proteins exported by T1SS machinery, from enzymes to toxins and adhesins [26]. Proteins secreted by T1SSs contain a C-terminal secretion system, most commonly in the terminal 15-30 amino acids [35-39], implying that the molecule must be secreted in a post-translational fashion. There is no specific consensus for this signal sequence, although it would seem that there is a preference towards certain amino acids (LDAVTSIF) [26,40,41].

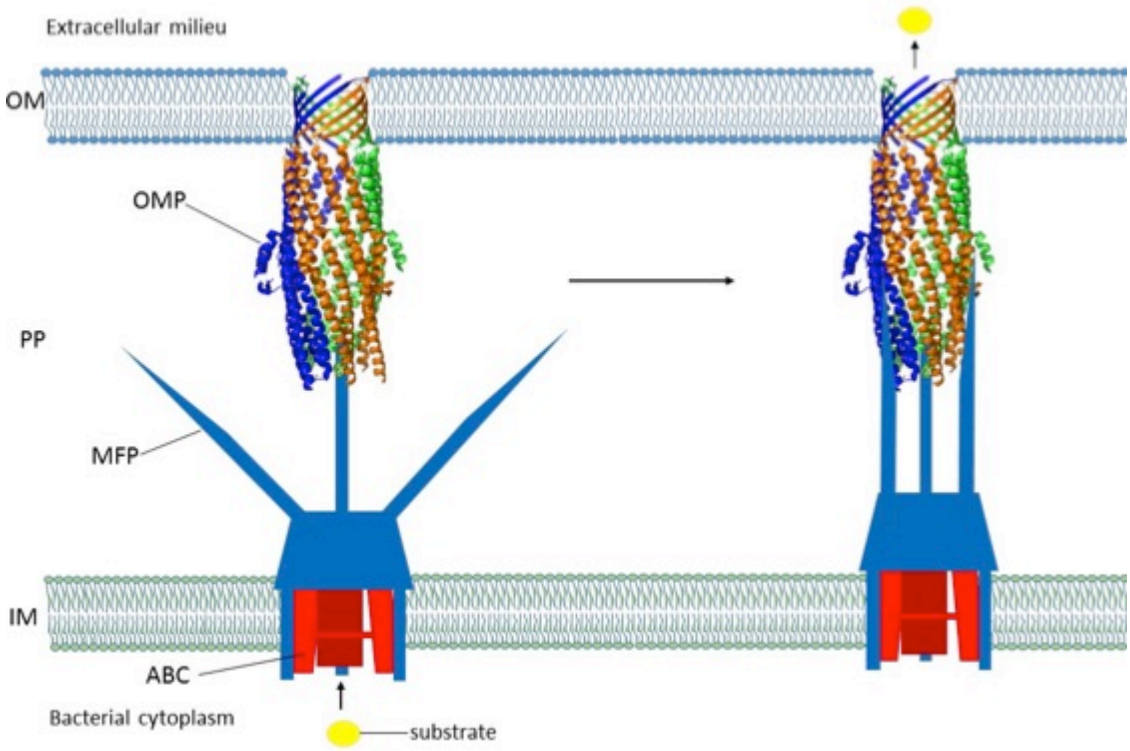

Figure 1.2 Schematic representation of the Type I Secretion System (T1SS). The position of the inner membrane (IM), periplasm (PP), outer membrane (OM) and the major components of the T1SS are shown: ABC – ATP Binding Casette (shown in red), MFP – Membrane Fusion Protein (shown in blue), OMP – Outer Membrane Protein. The structure of OMP is that of TolC (PDB entry 1EK9). The process displays the secreted substrate molecule (shown in yellow) binding to the ABC, which causes a conformational change in the MFP leading to its interaction with the OMP. The secreted substrate molecule is then subsequently translocated to the extracellular milieu.

1.3.2.2 Type II Secretion System (T2SS)

Compared to the T1SSs, type II secretion systems (T2SSs) are considerably more complex and are commonly employed in Gram-negative bacteria such as *Yersinia* spp and *Klebsiella spp*. In order to export proteins through the plasma membrane the Sec or Tat pathways is employed. Once in the periplasm, the protein is trafficked across the outer membrane using the T2SS. T2SSs employ 12 to 16 proteins for enabling secretion of folded proteins through the outer membrane. Perhaps surprisingly though only a couple of these are actually located in the outer membrane [38,39,42,43]. The majority of the proteins are located in the plasma membrane or in the periplasmic space (see Figure 1.3). For the T2SS, the general secretory pathway (Gsp) nomenclature is used, followed by a capital letter.

The cytoplasmic protein GspE is a hexameric ATPase, providing energy to drive the export of proteins [38,40,41]. GspE interacts with the inner membrane platform. This is composed of 4 core proteins (GspC, F, L and M) which anchor the ATPase to the pseudopilus apparatus [39,42-45]. The pseudopilus is composed of 5 proteins termed pseudopilins. The pseudopilins themselves are a group of proteins (GspG-K) that come together to form a large multimeric structure called the pseudopilus. The base of the pseudopilus is in the periplasm and interacts with the plasma membrane. Based on evidence from several experiments it has been hypothesised that the pilus may grow in order to push secreted molecules through the outer membrane complex, or alternatively as a cork to close off the outer membrane channel when not required [38,46].

The outer membrane complex of T2SS consists of two components, (i) the pore forming protein GspD, which exists as a multimer of 12-14 copies forming a pore in the outer membrane, and (ii) a lipoprotein GspS known as the ‘’pilotin’’, stabilises the GspD multimer in the outer membrane [44,45,47-49]. The pore formed by GspD is about 95 Å in diameter, a size large enough for proteins to pass through the T2SS assembly in a folded state [46,50,51].

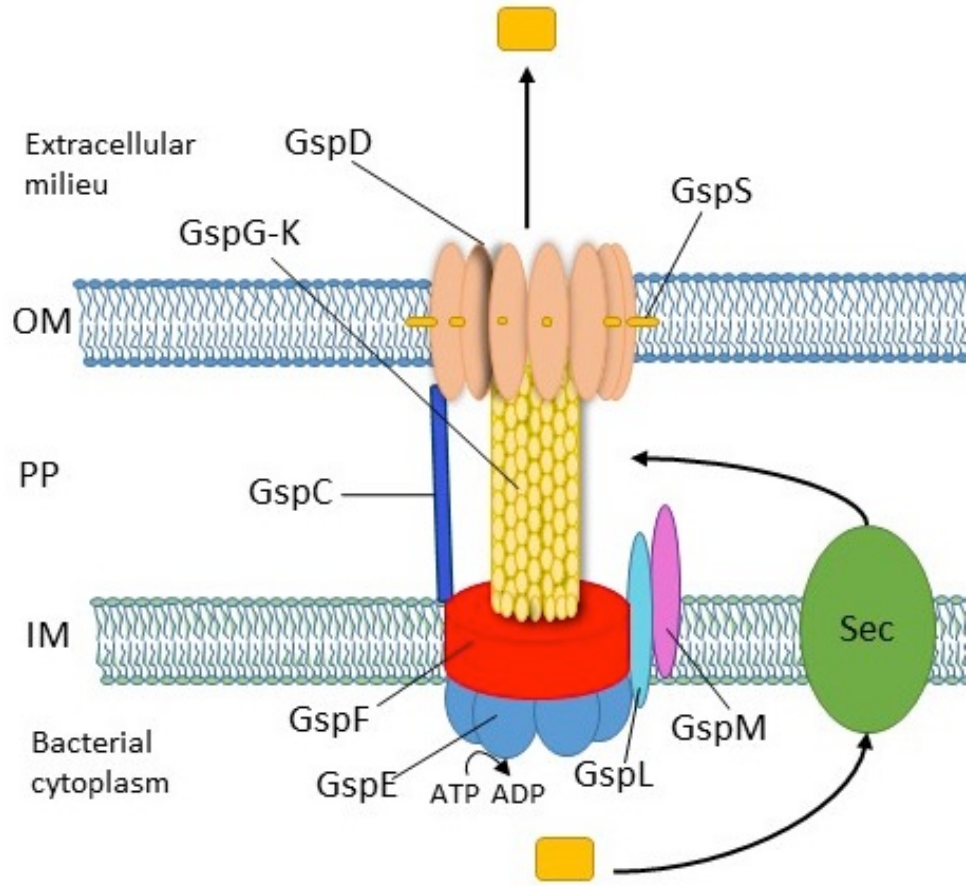

Figure 1.3 Schematic representation of the Type 2 Secretion System (T2SS). The position of the inner membrane (IM), periplasm (PP), outer membrane (OM) and the major components of the T2SS are shown. The cytoplasmic hexameric ATPase GspE (shown in blue) provides energy for protein export and interacts with the inner membrane platform composed of GspF, GspL, GsM and GspC (shown in red, light blue, purple and dark blue respectively). The inner membrane platform anchors the GspE hexamer to the pseudopilin (shown in yellow) comprising of GspG-K which links to the pore forming multimeric protein GspD (shown in light orange) in the outer membrane. GspS (shown in orange) stabilises the GspD multimer in the OM. The protein (shown as orange, rounded rectangle) is first transported from bacterial cytoplasm to periplasm using the Sec pathway (shown in green) and trafficked across the OM using the T2SS assembly.

1.3.2.3 Type III Secretion System (T3SS)

The type III secretion system (T3SS) is found in Gram-negative bacteria that interact with both plants and animal hosts, either as pathogens or symbionts [47-49,52]. The primary function of the T3SS machinery termed as the ‘’injectisome’’ is the delivery of effector proteins across the bacterial and host membranes into the cytosol of host cells to hijack host cell functions, including immune and defence responses [50-52]. This thesis is based on the T3SS of pathogenic *Yersinia pestis* and is described in detail in section 1.3.3.

1.3.2.4 Type IV Secretion System (T4SS)

In comparison to other secretion systems, the T4SS (Figure 1.4) is unique in its ability to transport a wide range of substrates such as single peptide molecules, protein-protein complexes and protein-DNA complexes. Furthermore, the T4SS is employed in the infection of a wide range of hosts ranging from higher eukaryotes such as animal and plant cells, to yeast and prokaryotes [52]. Many bacteria have homologous type IV secretion systems, including the pathogens *Agrobacterium tumefaciens* (VirB/D4), *Helicobacter pylori* (CAG/ComB) and *Pseudomonas aeruginosa* (TraS/TraB) [52,53]. Although T4SSs have garnered attention because of their significance in pathogenesis, it is important to point out that not all pathogenic bacteria have a T4SS.

There are several subclasses of T4SS, however the majority of the work to date, has focused on *Agrobacterium tumefaciens*. The VirB system from *A. tumefaciens* is capable of exporting DNA-protein complex from its Ti plasmid into the host [52,54]. Here, VirB4, VirB11 and VirD4 are cytoplasmic ATPases that generate the energy for the system, driving complex assembly followed by substrate translocation. VirB1 is a lytic transglycosylase responsible for making holes in the peptidoglycan layer thus allowing the formation of the protein channel [53,55]. VirB6-10 form a scaffold creating a translocation channel, connecting the plasma membrane to the outer membrane. This assembly enables the transport of the substrate directly from the cytoplasm to the extracellular milieu. The channel is a cylindrical structure with a diameter and length of 185 Å to allow for the exportation of folded protein molecules [54,56].

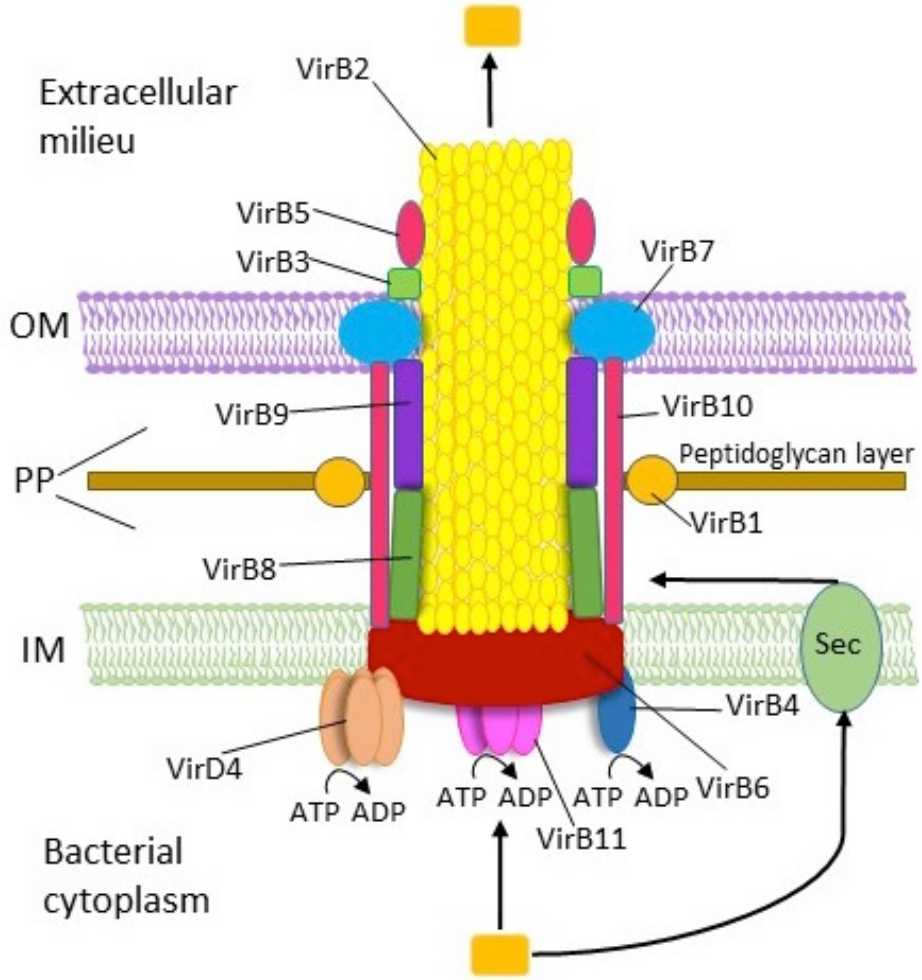

Figure 1.4 Schematic representation of the Type 4 Secretion System (T4SS). The inner membrane (IM), periplasm (PP), outer membrane (OM) and the major components of the T4SS are shown. The cytoplasmic proteins VirD4, VirB11 and VirB4 are ATPases providing energy for T4SS assembly and substrate translocation. VirB6-10 form a scaffold, spanning the bacterial cytoplasm to the extracellular milieu, creating a translocation channel for the substrate. VirB7 and VirB9 together form the pore in the OM for substrate translocation. VirB2 assembly forms the pilus connecting the IM to the OM. VirB3 and VirB5 interact with the pilus. VirB1 makes holes in the peptidoglycan layer allowing T4SS protein assembly. Substrate (shown in orange, rounded rectangle) is translocated either using the Sec-pathway from cytoplasm to the PP and then the extracellular milieu or directly from cytoplasm to the external environment using the T4SS.

1.3.2.5 Type V Secretion System (T5SS)

The type five secretion system (T5SS) (Figure 1.5) is typically referred to as the autotransporter system and is characterised by the requirement of SEC machinery and a β-barrel domain [14,55,57-59]. The process of transport from the plasma membrane to the outer membrane can be divided into three sub classes, monomeric autotransporter system (T5aSS), two partner secretion pathway (T5bSS) and trimeric autotransporters (T5cSS) [14,56-59]. The T5SS serves as a pathway for secretion of a

large number of proteins exceeding the number of proteins secreted by the T2SS. Over 500 proteins are secreted through the T5aSS class alone. The majority of the T5SS secreted proteins that have been characterised to date are responsible for the virulence of animals or human pathogenic bacteria [14,57-59].

The T5SS proteins are produced with an N-terminal signal peptide, which exports them into the periplasm using the Sec pathway. The bacterial proteins secreted via the T5aSS typically comprise an N-terminal passenger domain from 40 - 400 kDa in size and a conserved C-terminal domain which forms a β-barrel [14,57-60]. The β-barrel is able to insert into the outer membrane and is needed for translocation of the passenger domain into the extracellular milieu. In some cases, such as adhesins, the passenger domain remains attached to the β-barrel and the protein remains attached in the outer membrane. In other cases, the passenger domain is cleaved from the β-barrel to form a toxin or hydrolytic enzyme. Recently, detailed structural studies have suggested that the barrel is not capable of transporting the passenger domain by itself. It has been hypothesised that a helper protein, Omp85/YaeT enables the transportation across the outer membrane [57,59]. Proteins secreted via the T5aSS include IgA protease from *Neisseria meningitidis* and Pertactin from *Bordetella pertussis* [14,60].

A second class of proteins secreted via the T5SS is called T5bSS proteins. In contrast to T5aSS, the passenger and translocator functions in T5bSS are located on separate polypeptide chains. T5bSS contains a pair of proteins in which one of the proteins carries the β-barrel domain, and the other is the secreted protein (passenger polypeptide). This process is called two partner secretion (TPS) [57,61]. The mechanism of transport of the passenger polypeptide of the T5bSS is similar to the passenger domain transport in T5aSS. T5bSS (TPS) secreted proteins include adhesins such as HecA/HecB of the plant pathogen *Dickeya dadantii (Erwinia chrysanthemii)* and cytolysins such as ShlA/ShlB of *Serratia marcescens* [14,62].

The third sub-class of T5SS proteins, called T5cSS are trimeric autotransporters, in which a single β-barrel is formed by contributions from each of the three monomeric subunits. In contrast to the monomeric T5aSS, they are usually adhesins and don't exhibit enzymatic function. However, the method of transportation of the passenger

domain is identical to that in T5aSS. An example of T5cSS protein is YadA, the *Yersinia* adhesin A of *Yersinia enterocolitica* [61,63-68].

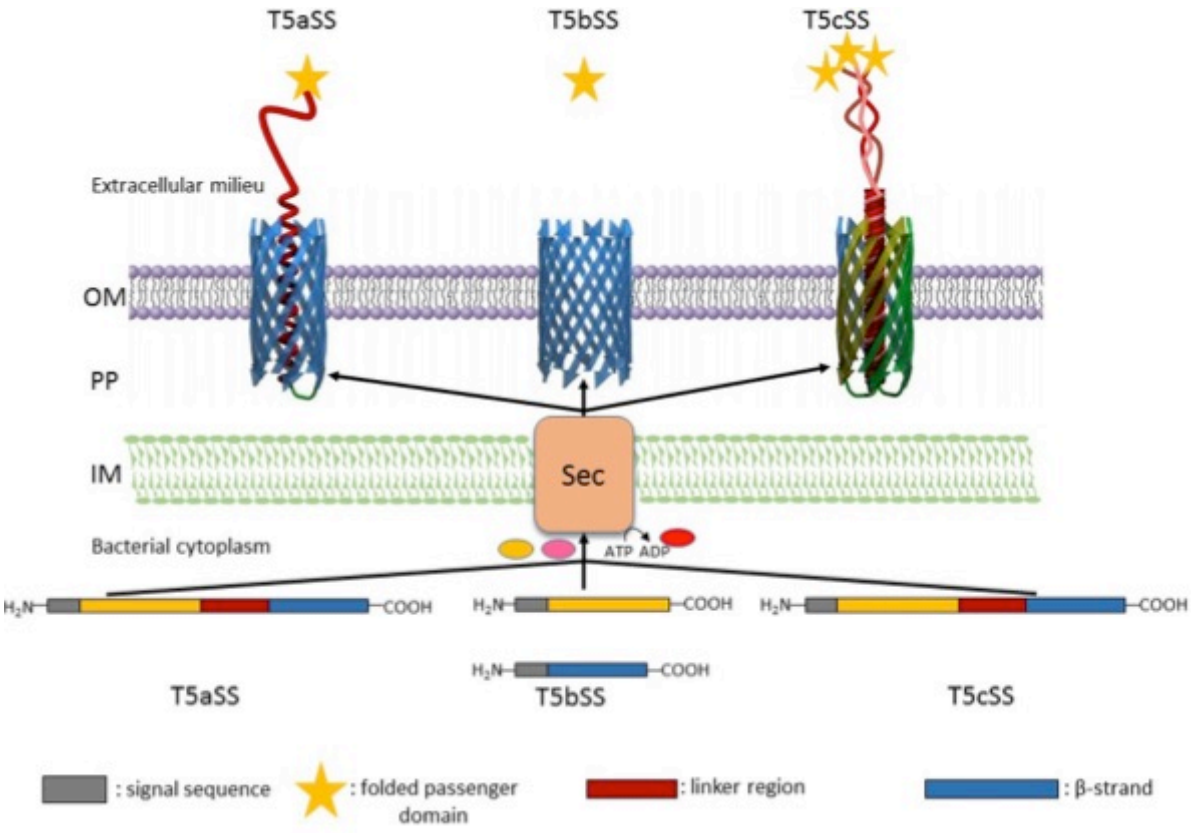

Figure 1.5 Schematic representation of the Type 5 Secretion System (T5SS). Inner membrane (IM), periplasm (PP), outer membrane (OM) and the major components of the T5SS are shown. The secretion pathway of the monomeric autotransporter system (T5aSS) is depicted at the bottom left, the two-partner system (T5bSS) is displayed in the centre, and the trimeric autotransporters (T5cSS) is shown on the right. The four functional domains of the proteins are shown: the signal sequence, the passenger domain, the linker region, and the β-domain. The autotransporter proteins are synthesised and exported through the cytoplasm across the IM via the Sec machinery. Once, through the IM, the signal sequence is cleaved and the β-domain inserts into the OM in a β-barrel structure forming a pore in the OM. The passenger domain then inserts into the pore and is tranlocated across the OM to the extracellular milieu.

1.3.2.6 Type VI Secretion System

The type VI secretion system (T6SS) is the most recently identified Gram-negative bacterial secretion system. The name T6SS was first coined in 2006, when it was identified in *Vibrio cholera* [62,69-71]. T6SS is highly conserved and is found in nearly 25% of all Gram-negative bacteria such as *Pseudomonas*, *Escherichia*, *Agrobacterium*

and *Helicobacter spp*. [63-68,72]. It is a large complex composed of 13 core components that span from the cytoplasm, to the extracellular milieu and the target cell. These proteins collectively assemble a structure reminiscent of an upside-down bacteriophage-like structure anchored to the bacterial cell envelope [69-71,73]. T6SS machinery is capable of delivering effector proteins directly into the host cell cytoplasm in a single-step, independent of the Sec and Tat pathways [72,74].

The T6SS core components can be grouped into the base plate complex, sheath, tube and spike. In both *V. cholerea* and *P. aeruginosa*, the base plate complex comprises of TssE (type six subunit E), TssF, TssG, TssJ, TssK, TssL, TssM and TssA. TssEFG are located in the cytosolic side of the bacterial inner membrane and in close proximity to the tube complex [73,75-77]. TssL is anchored in the inner bacterial membrane, TssM is bound to the inner membrane and extends outwards interacting with TssJ, an outer membrane lipoprotein [74,78]. The roles of TssF, TssG and TssA are unclear although they are universally conserved [73,75-77]. The formation of the base plate assembly is followed by the haemolysin coregulated protein (Hcp) tube formation. The Hcp tube undergoes polymerisation and emerges from the base plate complex spanning the bacterial cytosol to the extracellular milieu [78,79]. Then the VipA/VipB sheath polymerises around the growing Hcp tube. TssK is an essential cytoplasmic protein, which interacts with membrane bound TssJ-TssL-TssM complex as well as the tube and sheath components of the T6SS [73]. Analogous to phage, a conformational change in the sheath structure causes contraction. This propels the Hcp tube out of the cell and across the target cell membrane. This contraction event enables the delivery of effectors loaded onto the VgrG (valine-glycine repeat G)/PAAR (proline-alanine-alanine-arginine motif containing proteins) spike complex or the distal end of the Hcp tube [79,80]. The contraction process disassembles the unsheathed Hcp tube; parts of the tube that are not expelled from the cell are recycled within the cytosol. The contracted sheath is remodelled by the ATPase activity of ClpV, restoring the pool of available sheath subunits. Sheath components VipA/VipB interact with ClpV that is associated with the baseplate components in the bacterial cytosol. The naked baseplate complex is then either recycled or disassembled, depending on the

requirement and activation state of the T6SS [7,73]. The T6SS assembly is shown in Figure 1.6.

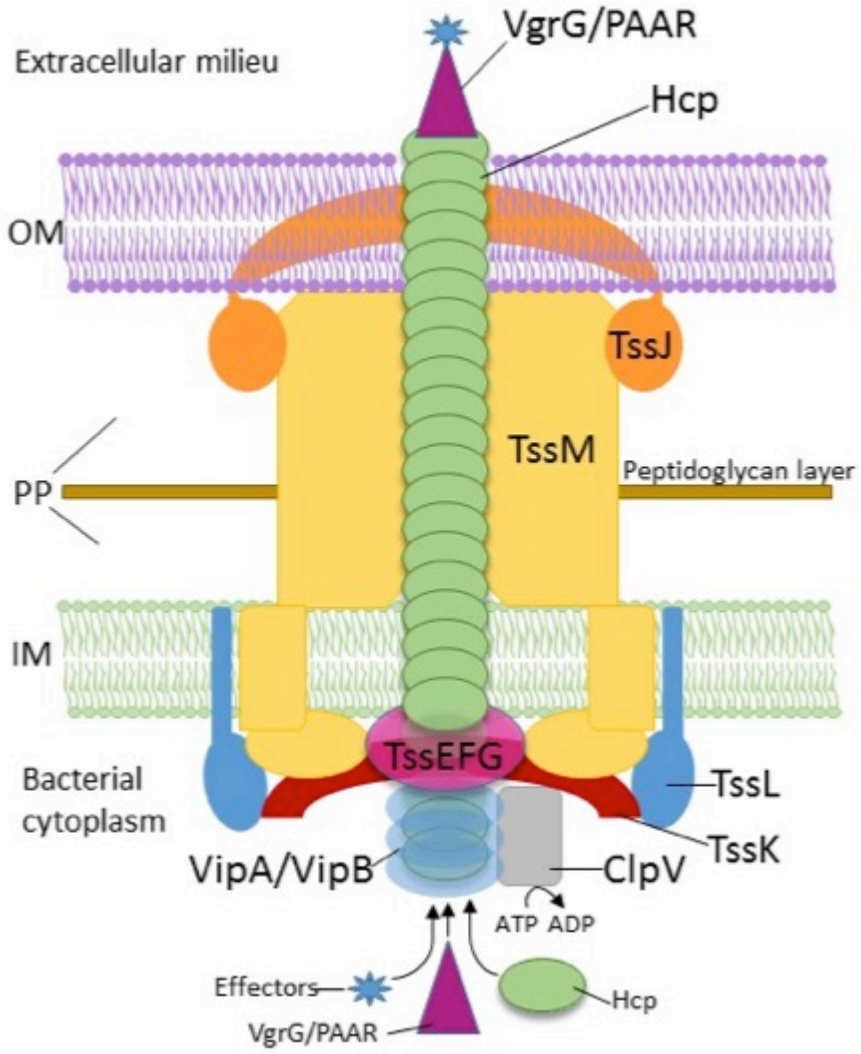

Figure 1.6 Schematic representation of the Type 6 Secretion System (T6SS). The inner membrane (IM), periplasm (PP), outer membrane (OM) and the major components of the T6SS are shown. The components of the base plate complex: TssEFG are located on the cytosolic side of the IM, TssL is anchored in the IM, TssM is bound to the IM and extends to the OM and interacts with TssJ, TssK interacts with membrane bound TssJLM complex, and sheath and tube components. The tube is formed of Hcp polymer, emerging from the base plate spanning the cytoplasm to the extracellular milieu. The sheath is composed of VipA/VipB which polymerises around the growing Hcp tube. Conformation change in sheath components causes contraction of Hcp tube causing the propulsion of the spike complex of VgrG/PAAR located at the tip of the Hcp tube along with the loaded effectors into the target cell in the extracellular milieu. ATPase ClpV remodels the sheath, recycles the tube and drives the translocation of effectors and VgrG/PAAR spike complex through the T6SS machinery.

1.3.3 Type Three Secretion System in Detail

Pathogenic *Yersinia* species cause human diseases ranging from relatively mild intestinal disease for *Yersinia enterocolitca* [80-84] to bubonic plague for *Yersinia pestis* [7,85]. Despite the differences in disease, virulence of the *Yersinia* species is caused by a conserved type three secretion system (T3SS), which is now a well-established model system for this form of protein secretion. Although the T3SS was first discovered in *Yersinia pestis,* it is a conserved virulence factor amongst other human pathogens such as enteropathogenic *Escherichia coli* (EPEC), *Salmonella spp., Pseudomonas aeruginosa, Shigella flexneri,* and *Chlamydia spp.* [81-84,86]. These pathogenic bacteria collectively cause numerous fatalities and significant healthcare costs annually [85,87-90].

T3SS uses a molecular syringe for the delivery of cytotoxic effectors into eukaryotic host cells. These effectors influence and manipulate diverse cellular pathways in the eukaryotic host for the survival and proliferation of the pathogen by either repressing the inflammatory response or altering phagocytosis [83,86,90]. Interfering with the delivery of effectors could have substantial consequences on disease pathology. Since this virulence mechanism is conserved in numerous pathogenic bacteria, it makes an attractive target for novel therapeutics.

In *Yersinia spp.,* the genes of T3SS are located on a 70 kb virulence plasmid, and the expression of genes *in vitro* is dependent on temperature and calcium concentration, a phenomenon called the low calcium response (LCR) [87-92]. T3SS genes are not expressed at ambient temperature. However, upon increasing the temperature of *Yersinia* cultures from 26°C to 37°C in the presence of millimolar concentrations of calcium, conditions representing the mammalian host, T3SS genes are expressed at low levels and the molecular machinery known as the ‘‘injectisome’’ is assembled [90,92-94].

The ‘‘injectisome’’ comprises several components that can be broken down into the various units: (i) the basal body which is composed of the inner membrane ring, the scaffold proteins, the outer membrane ring, the export apparatus, the ATPase complex and the C ring; (ii) the needle which is an extension from the basal body into the

extracellular milieu and (iii) the pore complex also known as the ‘’translocon’’ which is formed in the membrane of the target (Figure 1.7).

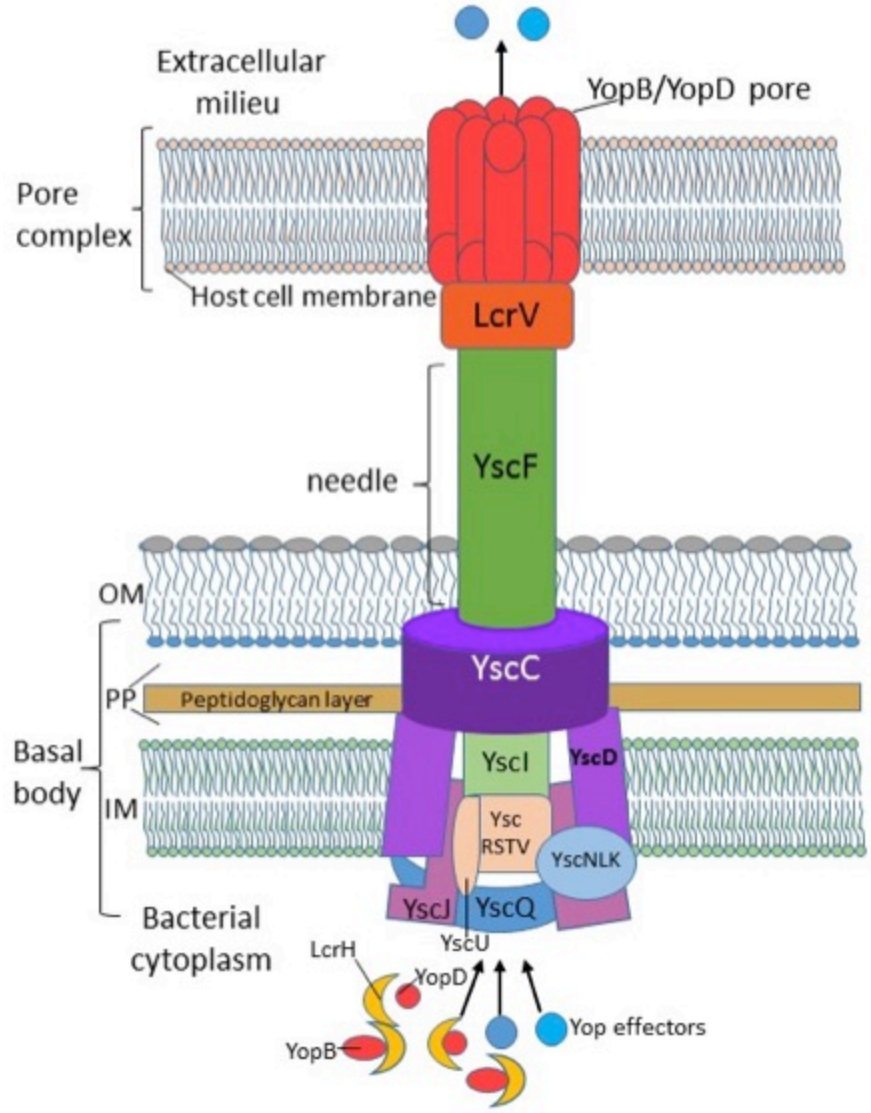

Figure 1.7 Schematic representation of the Type 3 Secretion System (T3SS). The inner membrane (IM), periplasm (PP), outer membrane (OM), the host cell membrane and the major components of the T3SS are shown: basal body, needle and pore complex. The basal body comprises of YscC, YscD, YscJ which form a platform for the assembly of YscQ, YscRSTUV and the complex YscNLK of which YscN is the ATPase powering the secretion of substrates. The needle comprises of YscI which forms a rod through which YscF is secreted and forms the needle. The pore complex is formed by the polymerisation of LcrV at the distal end of YscF forming a pentameric tip and complexes with translocators YopB and YopD which then insert into host cell membrane creating a pore or ‘’translocon’’. The class II chaperone LcrH (shown in yellow) is depicted as binding to YopB and YopD before being channeled across the T3SS assembly. The cargo of YopB/D is then released which gets inserted into the host cell membrane forming a pore.

THE BASAL BODY

Assembly of the T3SS is driven by the formation of the basal body which is initiated by the oligomerisation of YscC on the periplasmic side of the outer membrane and is termed the outer membrane ring (OM) [91,92,95,96] Next, a ring of YscD is assembled in the inner membrane and is thought to connect the inner and outer membrane rings [92-94,97]. YscD then binds to YscJ, which oligomerises to complete the inner membrane (MS) ring [92,93,95,96,98-104]. The assembly of these structures forms a basic channel through the bacterial envelope, which serves as a platform for the assembly of the remaining injectisome components.

On the cytosolic face of the basal body is the C-ring. This is composed of YscQ, which colocalises with YscC in the outer membrane stabilising the whole assembly. Additionally, a complex composed of YscN, YscL and YscK is formed and interacts with the C-ring. YscN is the ATPase that powers the secretion of substrates by the T3SS, YscL is a negative regulator of ATPase activity, while the function of YscK is unknown [97,105].

The next to follow is the assembly of the export apparatus composed of integral membrane proteins YscRSTUV [93,98-104,106-110] within the inner membrane, independently of the scaffold proteins. The pathways for assembly converge at this point with the recruitment of the export apparatus to YscJ in the MS ring of the scaffold [105,111,112]. The formation of the fully functional basal body is achieved with the amalgamation of the scaffold, ATPase complex and export apparatus. The basal body is now capable of exporting secretion substrates.

THE NEEDLE AND THE ''EARLY STAGE''

On completion of the basal body, YscI integrates into the inner membrane and forms the rod that allows substrate transport across the inner membrane. This stage is referred to as the ''early'' stage because only ''early'' substrates are translocated. These include the first proteins to be secreted: YscIFPXO and YopR [106-110,113-116]. The needle protein YscF is secreted through the YscI rod into the periplasmic space

allowing substrate transport across the inner membrane [111,112,117,118]. YscF then undergoes polymerisation to form the needle, which extends ~41 nm from the bacterium *Y. pestis* or ~58 nm from *Y. enterocolitica*. The needle has an outer diameter of ~6-7 nm and an inner diameter of ~2-3 nm [97,113-116].

YscPXO and YopR are not shown in the diagram but have a regulatory role. Indeed, YscP is required to control the needle length while YopR is important in the early stages of needle assembly, though its exact role is not clear [117,118]. Likewise, YscX and YscO are essential for the secretion of early substrates but are not secreted from the bacterium until needle assembly is complete [97,119]. YscY is thought to be the chaperone for YscX secretion [2,106] and YscY has also been shown to bind to SycD/LcrH, which is the chaperone for facilitating secretion of the middle substrates YopB and YopD. The role of the chaperones such as LcrH is covered more extensively below.

THE MIDDLE STAGE AND TRANSLOCON ASSEMBLY

The secretion of translocators LcrV, YopB and D into the extracellular milieu initiates the middle stage. LcrV polymerises at the distal end of YscF forming a pentameric tip on the needle complex [119,120]. YopB and YopD complex with LcrV at the needle tip and are inserted into the host cell membrane creating a pore. This large assembly is termed the pore complex or ''translocon''. This is the key step in the creation of the T3SS as organisms in which the translocon formation is impeded are rendered non-lethal *in vivo* [120,121].

Once the translocon is formed, Yops are delivered through the complex and the late stage, involving the delivery of effector proteins such as YopN and TyeA begins [121,122]. Here, immune supressing proteins and molecules targeting macrophages are released and the process of infection begins [122,123]

Table 1.1 Secretion Systems of Gram-negative bacteria describing their subunit composition, functional characteristics and citations.

Secretion System	Composition of subunits	Functional Characteristics	Citations
T1SS	ATP Binding Cassette (ABC) transporters also known as Inner Membrane Component (IMC) located in the inner membrane. e.g. AcrB in *E. coli*	ABC is an ATPase. It supplies energy for transport of variety of substrates such as ions and macromolecules.	AcrB - [123,124], PDB: 4CDI
	Membrane Fusion Protein (MFP) located in the periplasm. e.g. AcrA in *E. coli*.	MFP interacts with the OMP to complete the channel to the external milieu for export of various compounds.	AcrA - [124,125], PDB: 2F1M
	Outer Membrane Pore forming protein (OMP) is anchored in the outer membrane by a β-barrel structure. e.g. TolC in *E. coli*	OMP forms an exit duct for diverse molecules like protein toxins and antibacterial drugs.	TolC - [125,126], PDB: 2XMN

Secretion System	Composition	Function	Citations
T2SS	Inner Membrane (IM) platform comprising four core proteins: GspC, GspF, GspL and GspM tightly associated with cytoplasmic hexameric ATPase GspE.	GspE is an ATPase, provides energy to drive export of proteins and interacts with IM platform. GspC, F, L and M anchor GspE to the pseudopilus apparatus.	GspE - [126,127], PDB: 4KSR. GspC - [127,128], PDB: 3OSS. GspF - [128-130], PDB: 3C1Q. GspL - [129-131], PDB: 2W7V, 2BH1. GspM - [131,132], PDB: 1UV7.
	Periplasmic pseudopilus, a large multimeric structure composed of the major pseudopilin subunit GspG and minor pseudopilin subunits GspI, GspJ, GspK and GspH.	The base of pseudopilus is in the periplasm and interacts with the plasma membrane. Pilus may grow in order to push secreted molecules through the OM complex or block the OM channel when not required.	GspG - [132,133], PDB: 3G20. GspH - [133,134], PDB: 4DQ9. Gsp I/J/K - [134,135], PDB: 3CI0.
	Outer Membrane (OM) complex consists of a dodecameric secretin GspD and a lipoprotein GspS (pilotin).	GspD forms a large pore in the OM for passage of folded proteins and GspS stabilizes the GspD multimer in the OM.	GspD - [135,136], PDB: 3EZJ. GspS - [136,137], PDB: 3SOL.

Secretion System	Composition	Function	Citations
T3SS	Basal body Scaffold proteins: YscC, YscD, YscJ Export apparatus proteins: YscR, YscS, YscT, YscU, YscV. Cytoplasmic components: YscQ (C-ring) and YscN, YscL, YscK (ATPase complex).	YscC forms a ring in the OM, acting as scaffold. YscD & YscJ form a ring in the IM creating a scaffold. YscRST promote polymerization of YscV. YscU is essential for substrate specificity. YscN is the ATPase for substrate secretion by T3SS. YscN is a negative regulator of ATPase activity.	YscD - [137,138], PDB: 4D9V YscU - [138,139], PD: 2V5G
	The needle YscI, YscF, YscP, YscX, YscO and YopR YscI forms the rod, followed by secretion of YscF which forms the needle	YscI forms the rod to allow substrate passage across the IM. YscF undergoes polymerization to form the needle for translocation of substrates. YscP regulates the length of the needle. YscX and YscO are required for early substrate secretion.	YscF - [139,140], PDB:2P58 YscO - PDB: 4MH6 YopR - [140,141], PDB: 1Z21
	Pore complex LcrV (needle tip complex) YopB/YopD (translocon pore)	LcrV assists YopB/YopD for insertion in the host cell membrane. YopB/YopD create a pore into the host cell membrane and form the translocon for delivery of virulent proteins.	LcrV - [141,142], PDB: 1R6F YopD - [53,142], PDB: 4AM9

Secretion System	Composition	Function	Citations
T4SS	Inner Membrane (IM) complex is composed of three hexameric ATPases (VirD4, VirB4 and VirB11) located at the cytoplasmic side of the IM, together with VirB3, VirB6 and VirB8.	VirD4, VirB4 and VirB11 ATPAses provide energy for substrate transport and T4SS biogenesis. VirB11 assists VirB4 in pilus biogenesis and polymerization. VirB8 helps in the assembly of the pili.	VirB4 - [53,143], PDB: 4AG5. VirB11 - [143,144], PDB: 2GZA. VirB8 - [144,145], PDB: 4AKZ.
	Outer membrane (OM) complex comprises of VirB7, VirB9 and VirB10 with VirB10 extending from the IM to the OM.	VirB7 and VirB9 together from a pore in the OM for substrate translocation. VirB10 forms part of a scaffold around the translocation channel for substrate.	VirB7/VirB9/VirB10 - [145,146], PDB: 3JQO. VirB9/VirB10 - [74,146], PDB: 3ZBJ
	Conjugative pilus is composed of VirB2 and VirB5.	VirB2 and VirB5 form the major and minor subunit of the pilus respectively, connecting the IM to the OM.	

Secretion System	Composition	Function	Citations
T6SS	Baseplate complex comprising TssE (type six subunit E), TssF, TssG, TssJ, TssK, TssL, TssM, TssA and ClpV (ATPase). TssEFG, TssK, TssL, ClpV are located on the cytosolic side of bacterial IM, TssM is bound to the IM and extends onto the OM where it connects to TssJ.	TssM is bound to the IM and extends outwards interacting with TssJ. TssK interacts with membrane bound TssJLM complex, the tube and sheath components. ClpV is an ATPase, provides energy for assembly/disassembly of the sheath and baseplate components.	TssJ/TssM - [74,147], PDB: 3RX9 TssL - [147,148], PDB: 3U66 ClpV - [148,149], PDB: 3ZRJ
	Sheath component: VipA/VipB (TssB/TssC)	Interacts with ClpV in bacterial cytosol, causes contraction of the growing Hcp tube and propels the spike complex loaded with effectors.	VipA/VipB - [79,149], PDB: 3J9G.
	Tube component is haemolysin coregulated protein (Hcp) hexamer (Hcp1), connecting the IM with the OM.	Virulence factor, transporter of effectors and chaperone.	Hcp1 - [79,150], PDB: 4W64.
	Spike complex is made of PAAR-VgrG protein complex and in the OM.	Transportation of effectors into the extracellular milieu, killing of target cell.	PAAR-VgrG - [150,151], PDB: 4JIV

1.3.3.1 The role of Chaperones in the T3SS

For efficient export of both hydrophobic translocators and effector proteins specific chaperones are required. They act as ''bodyguards'' preventing their substrates from generating premature or non-specific interactions with other proteins in the bacterial cytosol prior to export. Moreover, they can maintain their substrates in a partially folded state in order to enable their passage through the narrow channel of the injectisome and may also play a role in secretion process [151-154]. Interestingly, the T3SS chaperones lack the ability to bind and hydrolyse ATP unlike classic chaperones like DnaK or GroEL. T3SS chaperones are divided into three sub-groups based on their binding partners and their modes of interaction: class I chaperones interacting with effector proteins, class II chaperones interacting with the translocators and class III chaperones interacting with T3SS needle components [152-155].

1.3.3.2 Class I Chaperones

Class I chaperones are relatively small (~10-15 kDa), acidic (pI 4-5) and generally display a homodimeric structure with a conserved α-β fold (Figure 1.8). They interact with their cognate effector protein through a chaperone-binding domain (CBD), which is located within the first 100 amino acids of the effector protein. This is downstream from the short amino terminal export signal. They are classified into two categories based on their interaction with their effectors: class IA chaperone bind a single effector, whereas class IB chaperones bind multiple effectors.

Class 1A chaperones: The majority of the structures solved to date fall into class IA. The examples for class IA chaperones are SycE [155,156], SycH [156,157], SycN-YscB (see Figure 1.8a) [157-159], SycT (see Figure 1.8b) [158-160] from *Yersinia spp.* and CesT [160,161] from enteropathogenic *E. coli* (EPEC).

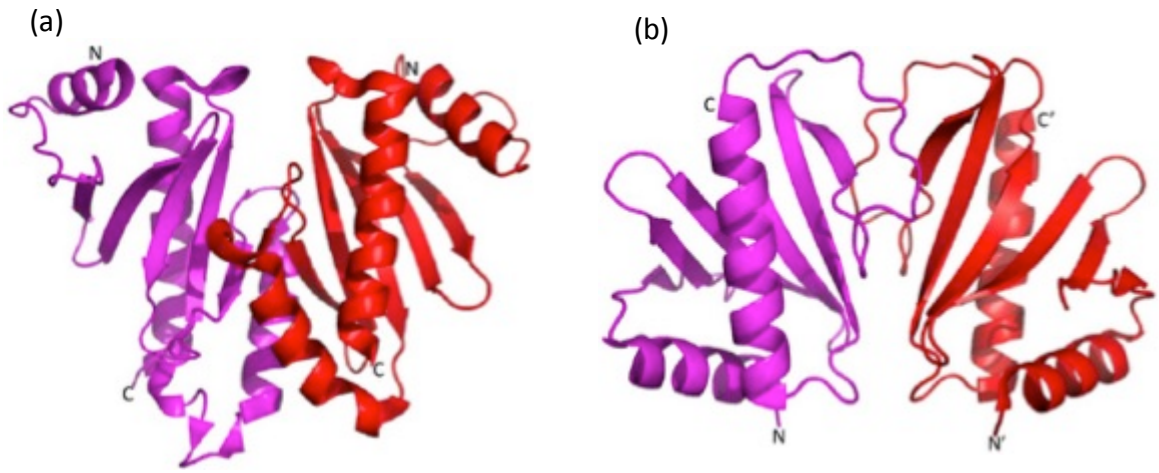

Figure 1.8 Ribbon representation of the crystal structure of class IA chaperones of the T3SS: (a) heterodimer SycN-YscB from *Yersinia pestis* (red/magenta, PDB code 1XKP), (b) homodimer SycT (the monomeric units are coloured magenta and red respectively, PDB code 2BHO). Figure was prepared using PyMOL.

The class I chaperones show low sequence similarity, but possess a conserved 3D structure and a common mode of binding. Each of these dimeric chaperones use a similar fold, where the monomer comprises of three α-helices and a five-stranded antiparallel β sheet arranged in the order of α-β-β-β-α-β-β-α, where the helices are positioned on one face of the β sheet. The central α helix and the loop and β strand, which immediately follows, are responsible for dimerization. This covers a hydrophobic surface area of generally around 2500 $Å^2$ [156,161-163]. The CBD of effector proteins wrap around chaperone homodimers in an extended, horseshoe like conformation with some α-helical secondary structure organisation [156,160,162-164]. The presence of hydrophobic surfaces on the chaperone homodimers are responsible for the binding of the cognate effector protein [156,160,162,164]. A good example of this interaction is SycH and its effector YscM2. Here the stable $YscM2_{(33-50)}$ fragment wraps around the homodimeric SycH in an extended fashion. $YscM2_{(33-50)}$ interacts with SycH via a structured α helix and β strand that dock with the β sheet and helix of the SycH [156,157] (see Figure 1.9).

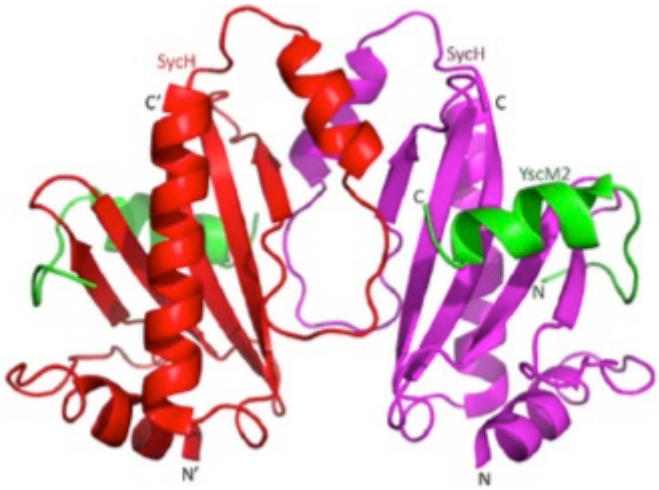

Figure 1.9 Ribbon representation of the crystal structure of *Yersinia pestis* T3SS Class IA chaperone SycH in complex with a stable fragment of its cognate effector protein YscM2$_{(33-50)}$ (PDB code 1TTW). The monomeric units of SycH are shown in red and magenta respectively. The effector YscM2$_{(33-50)}$ fragment is shown in green. Figure was prepared using PyMOL.

Interestingly there are deviations from the homdimeric structure described above. For example, the crystal structure of class IA chaperone SycN-YscB is unique amongst the class I chaperones because it is a heterodimer [157,161] (see Figure 1.11a). Here, although the topology of each monomer is conserved, the heterodimeric nature of the assembly leads to an asymmetry that does not exist in homodimeric class IA chaperones. Even though the α2 helix of YscB lies parallel to the dimer interface, as observed in the homodimers, the corresponding helix in SycN is tilted and induces a shift of β4 and β5 of YscB. This asymmetry in the dimer interface has a direct influence on the specific binding of YscB to its effector, YopN [152,161] (see Figure 1.10). YopN contains an N-terminal secretion signal followed by a chaperone-binding domain (CBD) where its two chaperones, SycN and YscB, bind. The YopN CBD wraps around SycN-YscB chaperone keeping YopN partially unfolded and secretion competent [152,165].

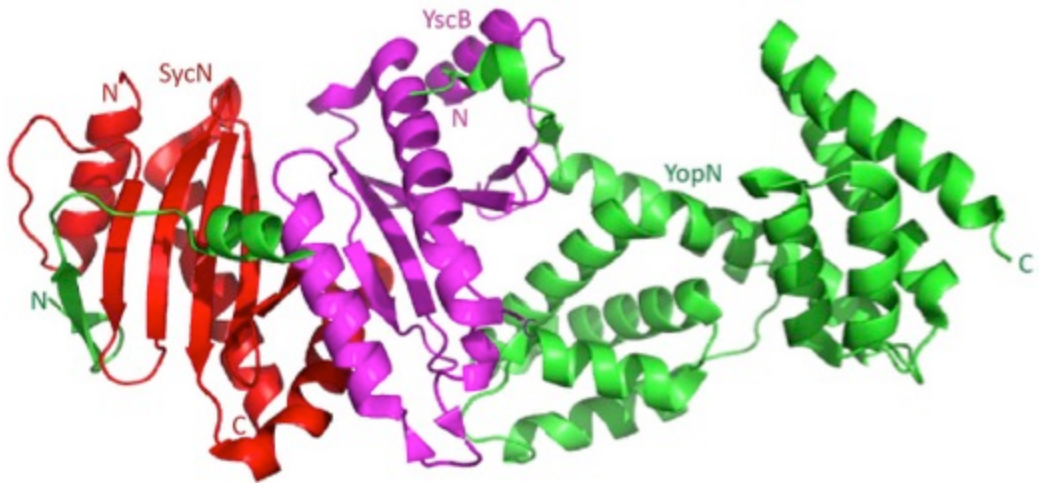

Figure 1.10 Ribbon representation of the crystal structure of *Yersinia pestis* T3SS macromeolecular assembly of effector YopN in complex with its heterodimeric class IA chaperone SycN-YscB (PDB code 1XKP). SycN, YscB and YopN are shown in red, magenta and green respectively. Figure was prepared using PyMOL.

Class 1B Chaperones: As stated previously, class IB chaperones contrast to the Class 1A by binding to multiple diverse effectors. For example, Spa15 from *Shigella flexneri* and InvB from *Salmonella enterica* (see Figure 1.11a and Figure 1.11b, respectively). Interestingly, in spite of possessing the ability to bind to various effectors, the monomers of each chaperone share the same overall fold as the class IA chaperones. However, the main difference lies with the orientation of the dimers. In particular, the α2 helices that form the dimeric interface have a different orientation, leading to a dimer in which the subunits are rotated about 30° with respect to each other. The residues that cause this differing shape and orientation of the α2 helix are conserved among other putative class IB chaperones and thus distinguish class IB from class IA chaperones. The change in dimeric shape also changes the orientation of the hydrophobic pockets that bind the effectors. The effectors still wrap around chaperone homodimers in the extended, horseshoe-like conformation, but the rotation of the assembly causes a longer wrapping linker. Moreover, the residues that form the hydrophobic binding regions are more highly conserved, enabling differing effectors to bind. This suggests that the chaperones of the 1B class are more general chaperones than the more specific class 1A [142,165-169].

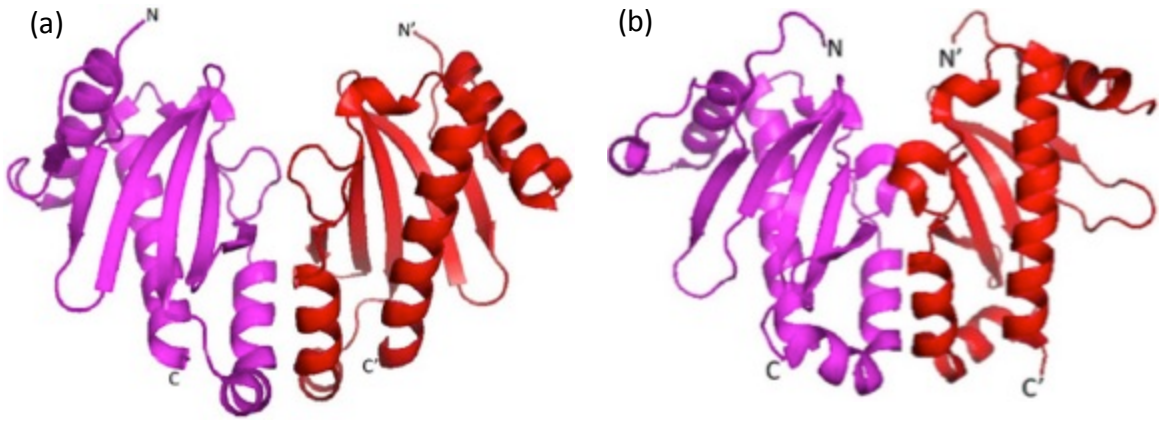

Figure 1.11 Ribbon representation of the crystal structure of class IB chaperones of the T3SS: (a) Spa15 from *Shigella flexneri* (monomers coloured red and magenta respectively, PDB code 1RY9) and (b) InvB from *Salmonella enterica* (monomers shown in red and magenta respectively, PDB code 2FM8). Figure was prepared using PyMOL.

1.3.3.3 Class II & III Chaperones

Both class II & class III chaperones are small, acidic and slightly larger than class I chaperones (~15-20 kDa). Both bind to parts of the secretion apparatus that is formed outside the bacteria. The class II chaperones bind to and stabilise the translocon forming translocator proteins (for example, YopB and YopD in *Yersinia* spp., PopB and PopD in *Pseudomonas aeruginosa* and IpaB and IpaC in *Shigella* spp., respectively). Similarly, the class III T3S chaperones bind to the needle component preventing their premature association or aggregation within the bacterial cytoplasm (for example YscF in *Yersinia* spp. and PscF in *Pseudomonas aeruginosa*). Importantly, the translocon pore and needle complexes can only form if their respective chaperones are present in the bacterial cytosol [142,166-171]. If the chaperones are knocked out, no needle or pore formation occurs, thus rendering the bacteria non-infective.

Interestingly, class II and class III chaperones, although binding to molecules that perform completely different functions, have remarkably similar structures. These are formed from multiple copies of a motif called the tetratricopetide repeat (TPR). TPRs are short 34 amino acid motifs that adopt a αhelix-turn-αhelix conformation and stack onto each other to form elongated structures [170-172]. The X-ray structure of a domain containing three TPRs from protein phosphatase 5 discovered the helix-turn-helix arrangement, with adjacent TPR motifs packing in a parallel fashion, resulting in a

spiral of repeating anti-parallel alpha-helices. The two helices are denoted as A Helix and B Helix (Figure 1.12). The packing angle between the two helices is ~24° within a single TPR and produces a right-handed super helical shape. Two protein surfaces are generated: mainly residues on helices A contribute to the inner concave surface, and the other surface presents residues from both helices A and B. There can be between 3 and 16 direct repeats in a given protein domain [170,172]. Individual TPR motifs are not stable and must be arrayed in tandem to fold correctly. TPR containing proteins are widespread in prokaryotic and eukaryotic organisms and are involved in a variety of biological processes, such as cell cycle regulation, transcriptional control, mitochondrial and peroxisomal protein transport, neurogenesis and protein folding [142,166-170].

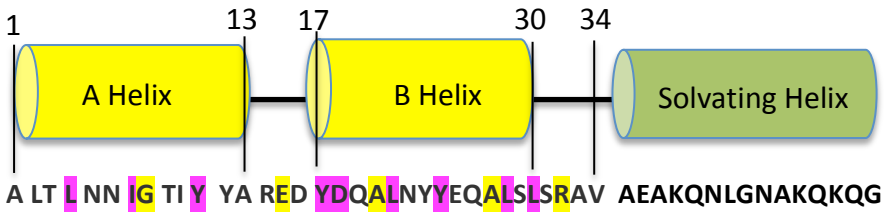

Figure 1.12 Consensus sequence of TPR. The consensus TPR motif (yellow) and solvating helix (green) sequence are displayed with the corresponding sequence underneath, 'n' denotes the number of consensus TPRs. The highly conserved residues are highlighted in yellow (>50% conservation of an identical residue) and pink (50% of similar residue type). The consensus sequence was taken from SMART (a Simple Modular Architecture Research Tool) database with accession no. SM00028.

Excitingly, crystal structures for both Class II and Class III chaperones were recently solved as follows:

1. **Class II Chaperones:** SycD from *Yersinia* enterocolitica, IpgC from *Shigella flexneri* and PcrH from *Pseudomonas aeruginosa* [139,142,166-169,173] (Figure 1.13).

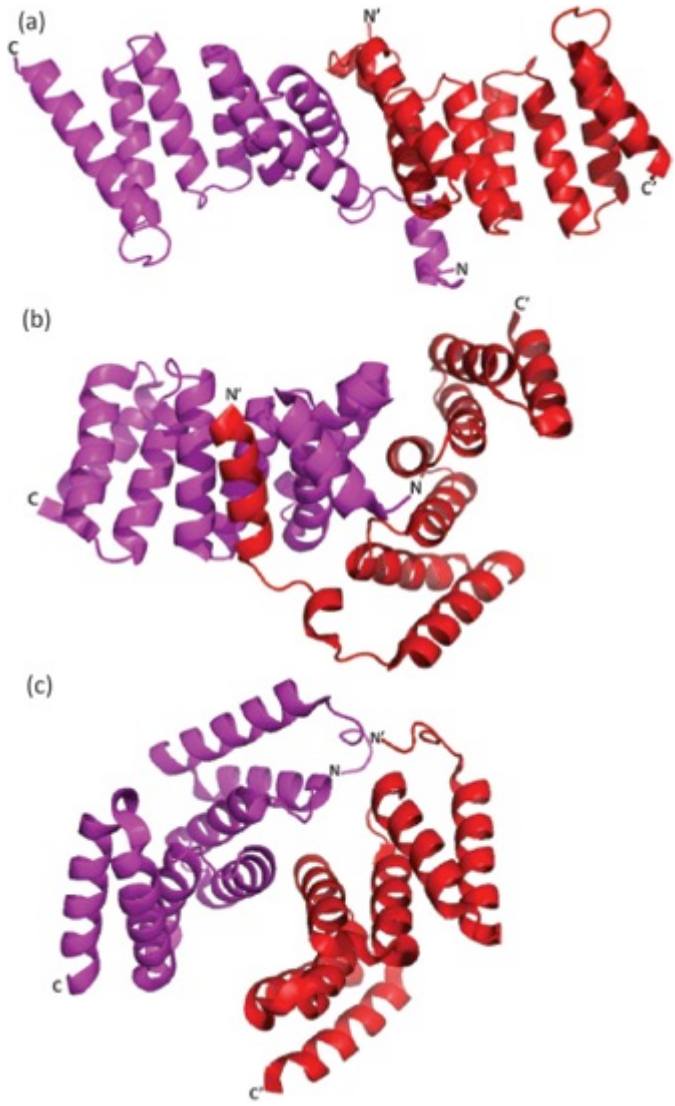

Figure 1.13 Ribbon representation of crystal structures of homodimeric T3SS class II chaperones: (a) $SycD_{(21-163)}$ from *Yersinia enterocolitica* (PDB code 2VGX), (b) IpgC from *Shigella flexneri* (PDB code 3GYZ) and (c) $PcrH_{(21-160)}$ from *Pseudomonas aeruginosa* (PDB code 2XCC). The monomers are shown in red and magenta respectively in each of the above structures. Figure was prepared using PyMOL.

2. **Class III Chaperones:** YscG from *Yersinia* enterocolitica and PscG from *Pseudomonas aeruginosa*[139,167,168,173] (Figure 1.14).

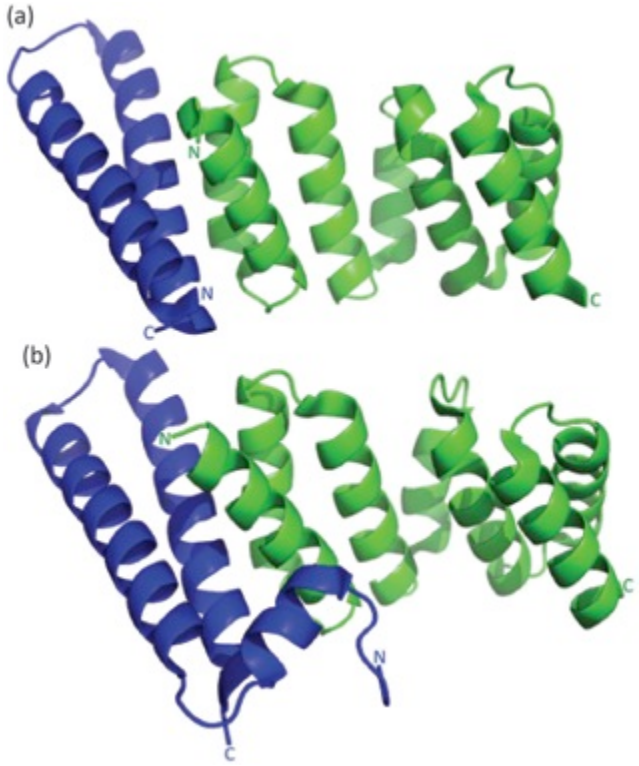

Figure 1.14 Ribbon representation of the crystal structure of T3SS class III chaperones: (a) YscG (coloured green) in complex with YscE (coloured blue) from *Yersinia enterocolitica* (PDB code 2P58) and (b) PscG (coloured green) in complex with PscE (coloured blue) from *Pseudomonas aeruginosa* (PDB code 2UWJ). Figure was prepared using PyMOL.

The structures reveal that each class of chaperone possess a TPR domain of 3.5 TPR motifs. These form a basket-like molecule that has concave and convex sides. In each case their secretion apparatus cargo is bound to the concave face of the molecule. However, the mode of binding within this concave face and oligomeric structure of each chaperone is very different for both classes. Class II chaperones form homodimers that bind to extended peptides of the translocator proteins. Whereas Class III chaperones form heterodimers with a further protein and bind a structured helical segment of their needle cargo. This might be due to the class II chaperones being required to bind two types of cargo protein and the class III chaperones only being required to bind one cargo protein. To dissect the structures in more detail each class is discussed separately in detail below.

1.3.3.4 Structure and biophysical characterisation of Class II Chaperones

Oligomeric Structure: Although class II chaperones are generally homodimers their exact mode of dimerization is somewhat ambiguous. The crystal structures provide a number of possible conformations depending on the protein and construct used (Figure 1.15 and Figure 1.16). For N-terminally shortened SycD (21–163) and IpgC (10–151), further mutational analysis suggested that the head-to-head dimer was the relevant unit (Figure 1.15). In the case of SycD, crystal structures show two possible head-to-head conformations (Figure 1.15a&b). In contrast, the relevant unit of full-length IpgC (1–151) seems to be a back-to-head conformation (Figure 1.15d). N-terminally shortened PcrH (21–160) crystal structures show two dimer structures that might be stable in solution, an asymmetric back-to-back dimer and a symmetric head-to-head dimer (Figure 1.15 (e) & (f)).

To investigate the physiological role of class II chaperone dimerization, *in vivo* experiments were carried out in Yersinia and in Shigella, respectively. Here, the mutated monomeric mutant showed characteristics typical of a null mutant. These consisted of a lack of translocator secretion and an inability to invade mammalian cells [166-168,174]. Yet studies on AcrH and PcrH have shown that translocator binding disrupts their dimeric structures and produces 1:1 chaperone-translocator complexes [166,174-176].

Such structural ambiguity suggests certain flexibility in the topology of the translocator chaperones, which would seem to be of importance to their function. This appears logical given the modular TPR units that form their structure. However, there is little information and no biophysical studies to have specifically investigated whether this is the case. These questions form the basis of this thesis and will be elaborated in Section 1.4 – Thesis Aims.

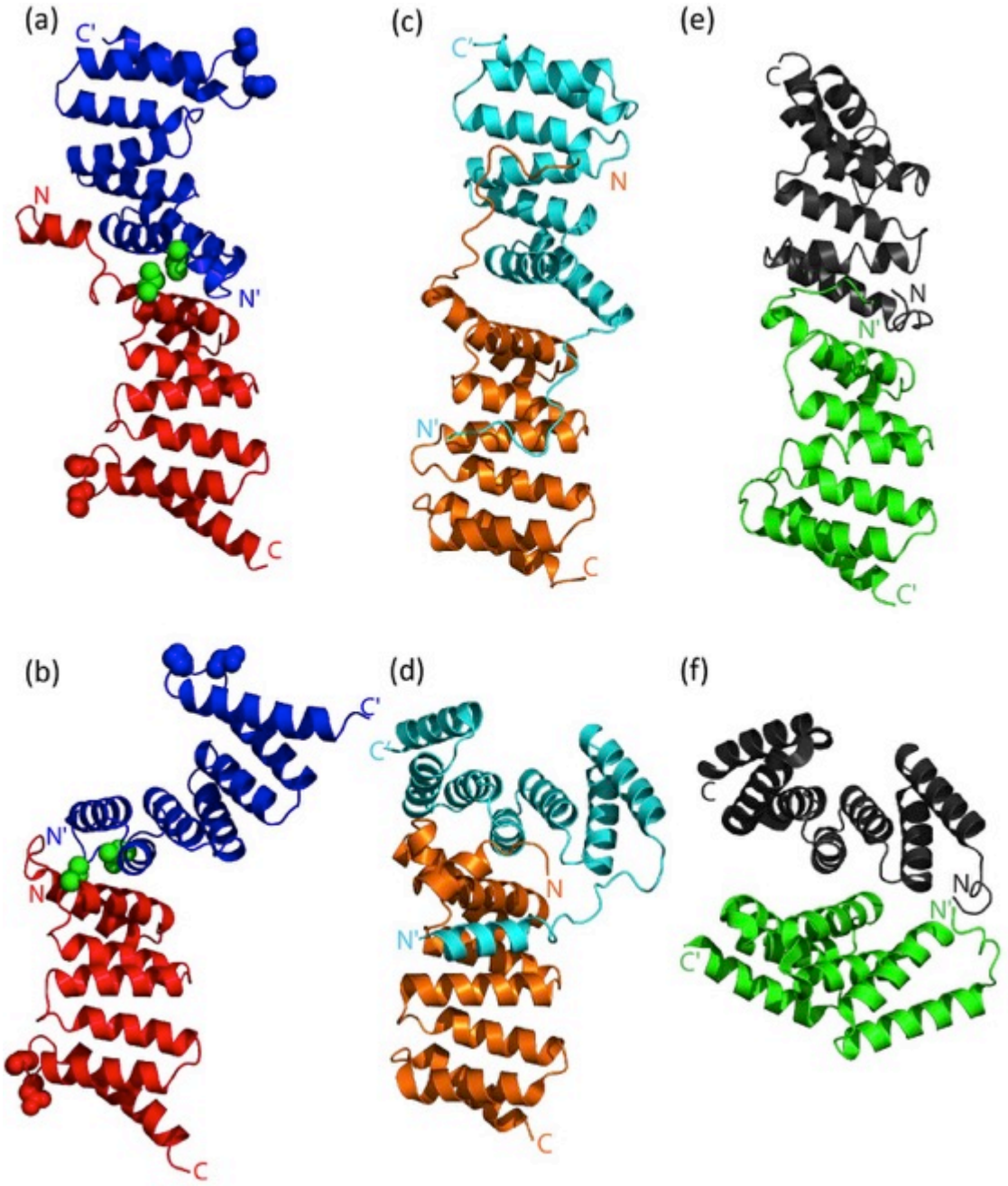

Figure 1.15 Ribbon representation of the crystal structures of class II chaperones: (a) & (b) head-to-head confirmations of dimeric obtained without YopD peptide $SycD_{21-163}$. Chains A and B of $SycD_{21-163}$ are coloured blue and red, respectively. Structures (a) and (b) were produced from 2VGX.pdb and 2VGY.pdb, respectively. Leucine 65 is represented by green spheres and was mutated to glutamic acid to obtain monomeric protein. LcrH differs from SycD in only two positions (N136D and P138T). These amino acids are shown as space fill spheres in each of the monomeric units. (c) & (d) Two differing conformations of dimeric $IpgC_{10-151}$ (c) and dimeric $IpgC1_{-151}$ (d). Chains A and B of IpgC are coloured cyan and orange, respectively. Structures (c) and (d) were produced from 3GZ1.pdb and 3KS2.pdb, respectively. (e) & (f) Two differing conformations of dimeric $PcrH_{21-160}$. Chains A and B of $PcrH_{21-160}$ are coloured dark and green respectively. Structures (e) and (f) were both produced from 2XCC.pdb. Figures (a) to (f) were prepared using PyMOL.

Cargo Binding: Although biochemical studies have implicated more than one interaction between chaperone and translocators, structures of IpgC with IpaB (51–72), PcrH (21–160) with PopD (47–56), and SycD (21-163) with YopD (56– 65) show a common main interaction where an extended peptide from each translocator binds to the same concave face of its cognate TPR domain (1:1 ratio) [142,166,175,176] (Figure 1.16). Thus, the structures suggest that the chaperone can only bind one translocator at any given time.

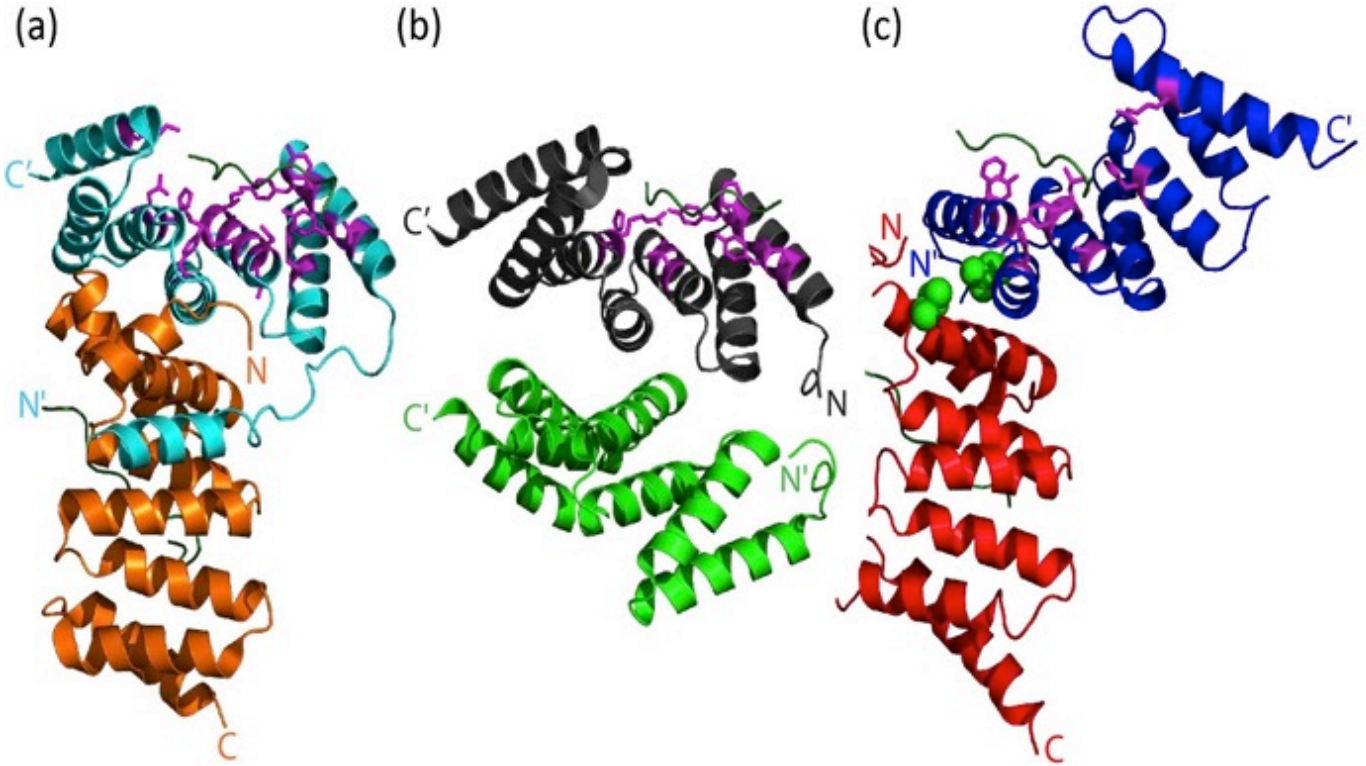

Figure 1.16 Crystal structures of class II chaperones bound to their cognate translocator protein peptides. (a) *Ribbon* representation of the asymmetric dimer $IpgC_{1-151}$ with bound peptides of $IpaB_{51-72}$ (major translocator protein) in back-to-head confirmation (PDB code 3GZ1). Chain A and chain B of $IpgC_{1-151}$ are coloured *cyan* and *orange*, respectively. The bound peptides of IpaB are coloured *dark green*. Residues in chain A of IpgC that interact with IpaB are shown as *sticks* and coloured *purple*. These are located in TPR1-3. (b) *Ribbon* representation of $PcrH_{21-160}$ with the bound peptide of $PopD_{47-56}$ (minor translocator protein) (PDB code 2XCB). Chain A and chain B of PcrH are coloured *dark grey* and *green*, respectively. The bound peptides of PopD are coloured *dark green*. Residues in PcrH that interact with PcrH are shown as *sticks* and coloured *purple*. These are located in TPR1-3. Figures were prepared using PyMOL. (c) *Ribbon* representation of the dimer $SycD_{21-163}$ with bound peptides of $YopD_{56-65}$ (minor translocator protein) in back-to-head confirmation (PDB code 4AM9). Chain A and chain B of $SycD_{21-163}$ are coloured *blue* and *red* respectively. The bound peptides of YopD are colored dark green. Residues in chain A of SycD that interact with YopD are shown as *sticks* and coloured *purple*. These are located in TPR1-3. Leucine 65 is represented by *green spheres* and was mutated to glutamic acid to obtain monomeric protein. SycD differs from LcrH in only two positions (N136D and P138T respectively). Figures were prepared using PyMOL.

A good example to illustrate the chaperone-translocator binding is the crystal structure of SycD in complex with a peptide of the N-terminal region of the minor translocator protein YopD (Figure 1.16 c). The N-terminal YopD hexapeptide ^{58}PELIKP^{63} has three hydrophobic residues (^{58}**P**E**L**IK**P**^{63}) that dock into three specific conserved hydrophobic clefts found along the concave face of the chaperone. The clefts are lined by aromatic and aliphatic residues mainly from the A helices of the first and second TPR motifs [142,167]. The same type of interaction and conserved residues were found in *Shigella* and *Pseudomonas* where the major translocator IpaB (^{58}**P**E**L**KA**P**^{63}) and the minor translocator PopD (^{49}**V**E**L**NA**P**^{54}) bind to IpgC and PcrH, respectively [167]. The binding mode is shown in Figure 1.16 and the sequence conservation of the chaperones is shown in Figure 1.17. Interestingly, Lunelli et al. performed Isothermal Titration Calorimetry (ITC) experiments to obtain a K_d for the interaction of PELKAP peptide with IpgC and various constructs of IpgC in which the peptide-binding site was disrupted. PELKAP bound to IpgC with a K_d of 625 ± 11 µM, whereas the $IpaB_{51-72}$ peptide, used in the co-crystallization bound to IpgC with a K_d of 72 ± 8 µM. The mutated IpgC showed no binding to the peptide, was unable to complement the deletion of *ipgC* in epithelial cell invasion and failed to allow secretion of translocator IpaB. Additionally, they assayed the K_D of peptides encoding the putative chaperone-binding motif of YopB (VQLPAP) and YopD (PELIKP) to SycD. These still showed an interaction, but with a very weak K_d of 455 ± 19 µM and 1,370 ± 38 µM respectively [167,173]. Thus although the peptide binding interfaces shown in the crystal structures are important, the ITC results suggest a further interaction site on the chaperone is probable.

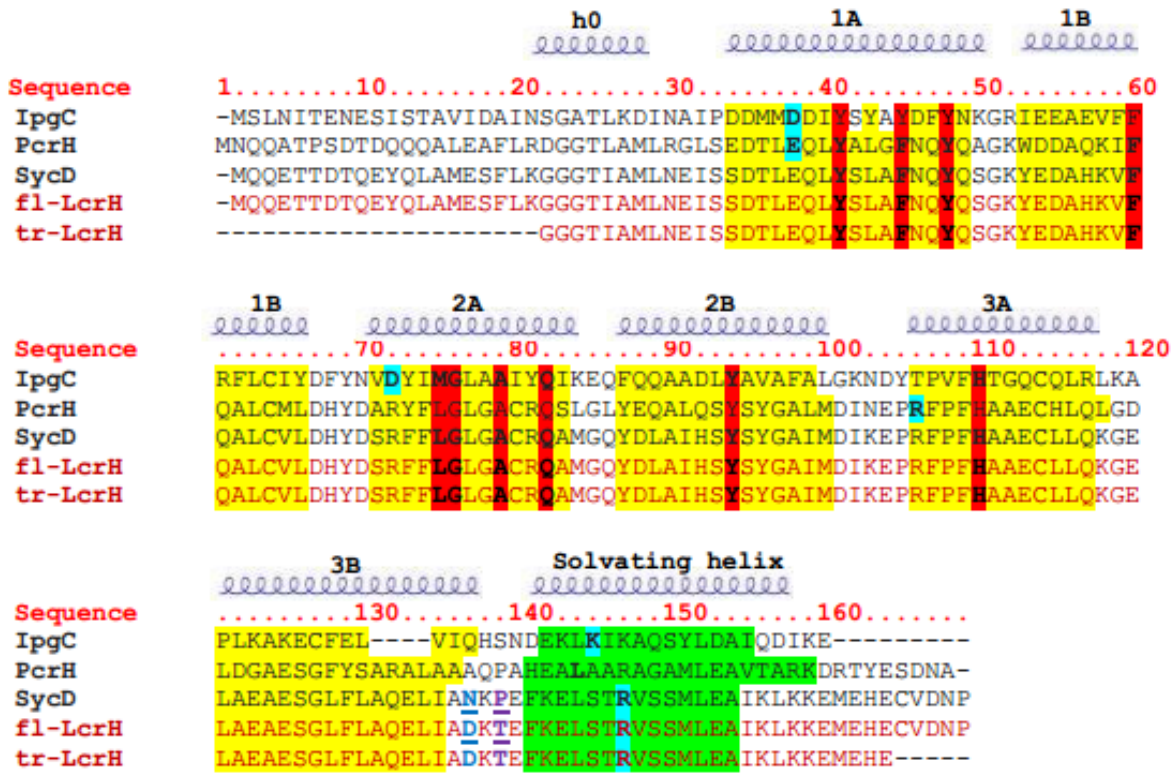

Figure 1.17 Structure based sequence alignment of T3SS Class II chaperones. IpgC from *Shigella flexneri*, PcrH from *Pseudomonas aeruginosa,* SycD from *Yersinia enterocolitica,* fl-LcrH and tr-LcrH from *Yersinia pestis* (residues are shown in red). Residues forming the TPR helices are highlighted in yellow. C-terminal solvating helix forming residues are highlighted in green. Residues involved in hydrophobic and van der Waal's interaction with the class II chaperone's corresponding translocator extended peptides are highlighted in red. Amino acids involved in salt bridge formation by interaction with side chain residues of corresponding translocator peptides are highlighted in light blue. The difference between SycD and LcrH (fl-LcrH and tr-LcrH) is in only two positions: N136D coloured dark blue and P138T coloured purple.

1.3.3.5 Structure and biophysical characterisation of Class III Chaperones

As stated earlier, although the class III chaperones possess a TPR domain like the class II chaperones, they don't form homodimers and don't bind their cargo as an extended peptide. Instead they interact with an additional protein to form a heterodimer and interact with their cargo through a structured α helix-turn-loop arrangement.

Oligomeric State: In both reported structures, the class III TPR chaperone domain binds a small 2 α-helical protein at its N-terminus. In *Pseudomonas* the TPR chaperone PscG binds PscE and in Yersinia the TPR chaperone YscG binds YscE (Figure 1.19). In both structures the interaction between these proteins is very similar, unlike the numerous different homodimers of the Class II chaperones. The two helices of

PscE/YscE interact through hydrophobic interactions with the first two N-terminal TPR containing helices of PscG/YscG. Protein sequence alignment of YscG, PscG and other related proteins showed that these hydrophobic residues are conserved (Figure 1.18). In the case of YscE/G, the total buried surface area of the interaction is 1548 $Å^2$. Moreover, the positioning of PscE/YscE in the complex means that it makes very little direct contact with the chaperones cargo, PscF/YscF (Figure 1.19). The total buried surface area between YscF and YscE in the complex is merely 276 $Å^2$. Thus it would seem that the role of PscE/YscE is most likely to be that of stabilising PscG/YscG in a form that can readily accept its cargo. The fact that YscE null mutant strains of *Yersinia* do not accumulate YscG and that PscE null mutant strains of *Pseudomonas* are non-cytotoxic support this hypothesis [139,173,177].

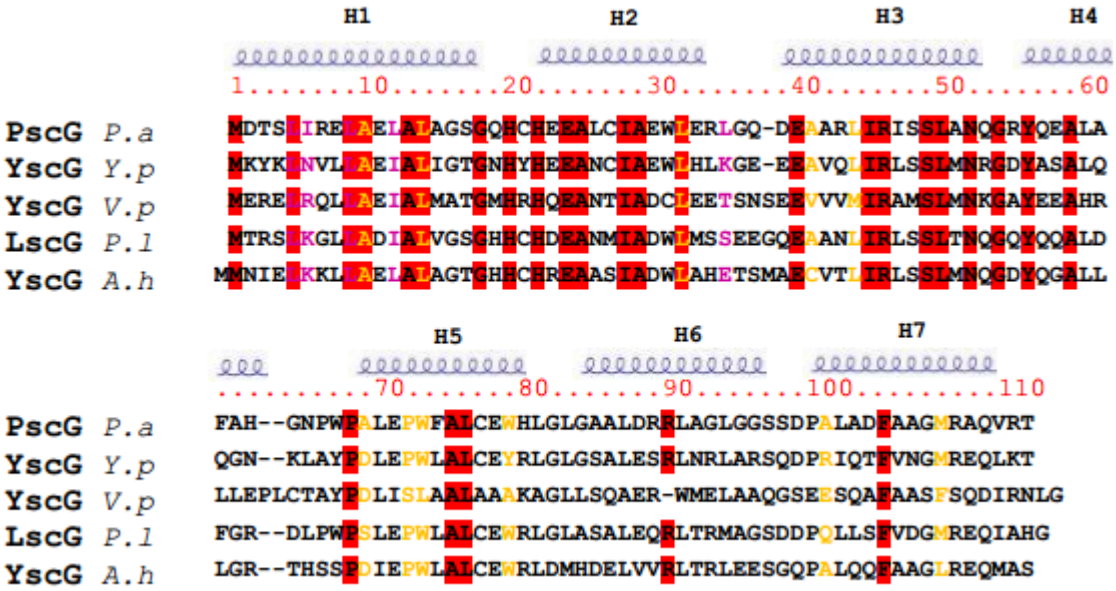

Figure 1.18 Structure based sequence alignment of T3SS class III chaperones sharing homology from diverse pathogens. PscG from *Pseudomonas aeruginosa* (nosocomial infections), YscG from *Yersinia pestis* (bubonic plague), YscG from *Vibrio parahaemolyticus* (gastrointestinal illness), LscG from *Photorhabdus luminescens* (insect pathogen), and YscG from *Aeromonas hydrophila* (respiratory illness in humans, reptiles, and birds). Residues showing 100 % conservation are highlighted in red. PscG homologs share high conservation within residues that interact with PscE (purple) and PscF (orange).

Cargo Binding: The main binding site of the heterodimer is located on the hydrophobic concave groove of the TPR domains of PscG/YscG. PscG/YscG acts as a scaffold to organise the assembly of PscE/YscE and PscF/YscF into the heterotrimeric complex. In both cases, the concave surface of PscG/YscG formed by TPR containing α-helices (H1, H3 and H5) and a C-terminal α-helix (H7), display a highly hydrophobic platform, which grasps the C-terminal helix of PscF/YscF. [139,173,177-180]. In YscEFG complex, the C-terminal residues of $YscF_{50-87}$ adopt a α-helical hairpin conformation within the TPR groove. The total buried surface area between YscF and YscG in the complex is 2724 $Å^2$. Thus, the complex that YscG makes with YscF is far more extensive than those made by the class II chaperones with their cargo. In synergy with the structure of YscEFG, the interaction of PscF mirrors that of YscF, but differs at the N-terminus. Here instead of the hairpin-helix conformation, the PscF shows an extended peptide. One explanation for the difference is the PscF construct used was truncated whereas the YscF was full length. Interestingly, further experimentation concluded that the N-terminal section of YscF (1-49) could not be resolved crystallographically as it was unstructured.

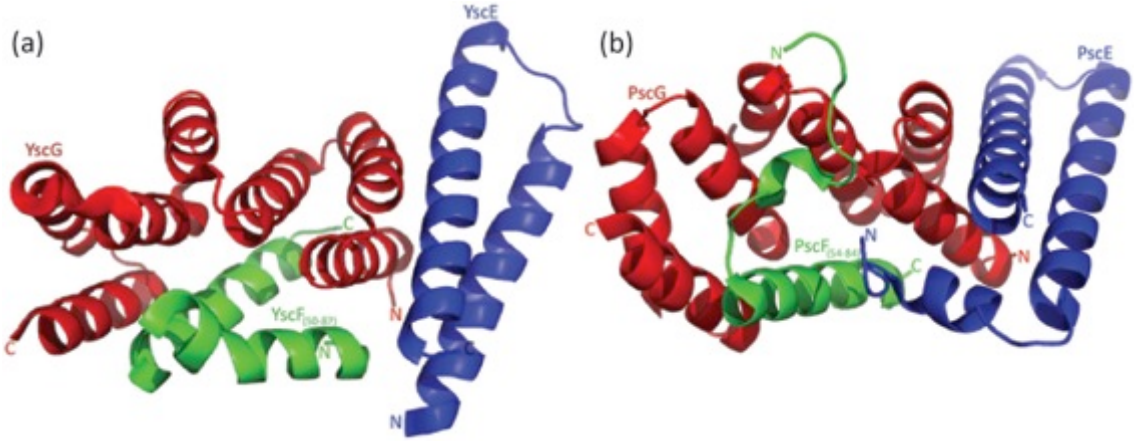

Figure 1.19 Crystal structures of the heterotrimeric complex comprising the class III chaperones: (a) YscEFG complex comprising the heterodimer chaperone of YscE/YscG (coloured blue/red) and needle protein $YscF_{50-87}$ (coloured green). (b) PscEFG complex showing the heterodimer chaperone of PscE/PscG (coloured blue/red) and needle protein $PscF_{54-84}$ (coloured green). Figures were prepared using PyMOL.

1.4 Thesis Aims

Given the crucial role of the class II translocator chaperones, this study aims to investigate their conformational stability and the thermodynamic importance of the homodimeric interface. To accomplish these aims the class II chaperone LcrH from *Yersinia pestis* was chosen as a model system. LcrH is identical to SycD from *Y. enterocolitica*, except for two minor amino acid substitutions, (Figure 1.15 and Figure 1.17).

Initially we will investigate the oligomeric states of different constructs of LcrH and their secondary structure characteristics. These will be achieved by: (i) constructing the LcrH genes - full length LcrH (*fl-LcrH*), truncated LcrH (*tr-LcrH*) and monomeric L65E LcrH (*tr-LcrH L65E*), (ii) carrying out molecular cloning of constructed LcrH genes into suitable expression vectors for protein expression followed by purification strategies and (iii) initial biophysical characterisation of LcrH protein constructs. The oligomeric states of these proteins will be studied by analytical size exclusion chromatography (SEC) and their secondary structure characterised through far-UV circular dichroism (CD).

Furthermore we will examine the monomer-dimer equilibrium and oligomeric state of various LcrH protein constructs which will be undertaken by the use of analytical ultra-centrifugation (AUC), analytical size exclusion chromatography (SEC) and dynamic light scattering (DLS). In addition I intend to explore the thermodynamic stability and flexibility of LcrH proteins through equilibrium chemical denaturations (monitored by far-UV CD and fluorescence spectroscopy).

Chapter 2 Materials and Methods

2.1 Molecular Biology Methods

In this study, three different constructs of LcrH – full length LcrH (fl-LcrH, 168 amino acids), truncated LcrH (tr-LcrH, amino acids 21-163, 143 residues) and mutant L65E LcrH (sequence identical to tr-LcrH, except at amino acid position 65 where leucine was mutated to glutamate) was produced. The techniques used for their gene construction and cloning are described as follows.

2.1.1 *fl-LcrH* gene synthesis

The *fl-LcrH* gene was synthesized using the steps outlined below:

2.1.1.1 Recursive PCR

The full length *LcrH* (*fl-LcrH*) gene was initially synthesized using a recursive PCR method. This required the design of eight coding and non-coding overlapping oligonucleotides that spanned the entire sequence of the *LcrH* gene (Figure 2.1). The overlapping regions in the oligonucleotides were 20 base pairs in length and engineered to give melting temperatures (T_m) in the range 54 – 64 °C. Computer based sequence analysis using ClustalW multiple sequence alignment of the entire gene sequence with the sequence of the overlap regions was performed. The sequence alignment showed them to be unique and unlikely to give non-specific priming. The designed sequences were synthesised by VH Bio Limited, UK and supplied in lyophilised form. They were dissolved in ddH_2O to give a stock concentration of 50 µM.

Figure 2.1: Schematic showing the recursive oligonucleotides required for synthesis of the LcrH gene. The gene is represented as a blue box, the coding oligonucleotides represented as black lines and the non-coding oligonucleotides represented as red lines. Note that each oligonucleotide overlapped with each of its neighbours by 20 bases.

To perform the recursive PCR the overlapping oligonucleotides (0.5 µM final concentration) were added to 10 x reaction buffer (5 µL, Stratagene), dNTPs (0.2 mM of each final concentration), sterile deionised distilled water and *Pfu Turbo* DNA polymerase (1 µL of 2.5 U μL^{-1} –Stratagene) to give a total reaction volume of 50 µL in a sterile PCR tube. The recursive PCR was carried out starting with 95 °C of initial denaturation for 2 minutes, followed by a cycle repeated 25 times: denaturation at 95 °C for 30 seconds, annealing temperature of 52 °C for 30 seconds, elongation at 72 °C for 30 seconds, and finally 10 minutes of extension at 72 °C in a thermal cycler.

2.1.1.1.1 Agarose Gel Electrophoresis

0.75 g of Molecular Biology grade agarose (Fisher, UK) was added to 50 ml of 1 x TBE buffer (Tris-Borate-EDTA buffer - 90 mM Boric acid, 2 mM EDTA, 90 mM Tris-HCl, pH 8.0) in a 100 ml conical flask. The mixture in the conical flask was then heated in the laboratory's microwave oven to prepare a 1.5 % w/v agarose gel. Ethidium bromide was then added to the molten agarose (final concentration 0.5 µg ml^{-1}). The complete mix was added to the gel mould and left to set. DNA samples were prepared by adding 1 µL of 6x gel loading buffer (0.25% Bromophenol Blue, 0.25% Xylene cyanol FF, 15% Ficoll) to 5 µL of DNA preparation. The gel loading buffer contains bromophenol blue dye, which helps increase the DNA sample's density allowing it to fall into the well of the gel and provides a visible marker to monitor the progress of electrophoresis. Once the gel was set, it was submerged in 1 x TBE buffer and loaded with DNA samples and 100 bp DNA ladder (0.5 µg of 100 bp DNA ladder diluted in loading buffer – NEB) for detecting the band of 500 bp *LcrH* gene. The 100 bp DNA ladder contains standard molecular size marker ranging from 100-1,517 bp. Agarose gel electrophoresis was performed in an electrophoresis tank (BIORAD, UK) by applying a current of 35 mA and voltage of 70 volts. DNA is negatively charged at pH 8.0, hence the application of an electric current caused migration of DNA towards the anode. DNA fragments migrate through the matrix of agarose gel at rates that are inversely proportional to the $\log_{10}$ of the molecular weight of DNA.

2.1.1.2 Polymerase Chain Reaction (PCR)

In order to extract a full length *LcrH* gene (*fl-LcrH)* with restriction sites for further cloning, a conventional PCR was performed using the recursive PCR product as template. Oligonucleotides were designed to match the termini of *fl-LcrH* (coding and non-coding

strands) with melting temperatures (T_m) of ≈ 70 °C. The coding oligonucleotide incorporated a *BamH*I and the non-coding oligonucleotide incorporated *Hind*III restriction site at their ends. The reverse oligonucleotide also incorporated a stop codon after the gene sequence, but before the *Hind*III restriction site. The designed sequences were synthesized by Integrated DNA Technologies, Belgium and supplied in lyophilised form. They were dissolved in ddH_20 to give a stock concentration of 50 µM.

To perform the PCR the oligonucleotides (0.5 µM final concentration of each) were added to the recursive PCR product (2 µL), 10 x reaction buffer (5 µL, Stratagene), dNTPs (0.2 mM of each final concentration), sterile deionised distilled water and *Pfu Turbo* DNA polymerase (1 µL of 2.5 U μL^{-1} –Stratagene) to give a total reaction volume of 50 µL in a sterile PCR tube. The PCR was carried out starting with 95 °C of initial denaturation for 2 minutes, followed by a cycle repeated 25 times: denaturation at 95 °C for 30 seconds, annealing temperature of 52 °C for 30 seconds, elongation at 72 °C for 30 seconds, and finally 10 minutes of extension at 72 °C in a thermal cycler. As before, on completion of the PCR, the entire PCR product was run on a 1.5 % agarose gel to confirm the success of the reaction (Section 2.1.1.1.1) showed a clear band of DNA at ~ 500 base pairs. The correct sized DNA was excised from the gel and purified (Section 2.1.3.2).

2.1.2 Insertion of synthesised *LcrH* gene into a cloning vector

The newly synthesized *fl-LcrH* gene was first incorporated into a cloning vector using the following strategy.

2.1.2.1 Cloning of *l-LcrH* gene into TOPO TA cloning vector

2.1.2.1.1 Poly-A tailing with Taq polymerase

1 unit of *Taq* polymerase was added to the PCR reaction from Section 2.1.1.2 and was incubated for 8-10 minutes (no cycle) at 72°C in a thermal cycler. This introduced a poly-A tail ('A' overhangs) of the 3' end of DNA which complements the 'T'-overhangs already present in the pCR®2.1-TOPO® vector (Invitrogen™). This enables the incorporation of the PCR product into the cloning vector for which the map is shown in Figure 2.2.

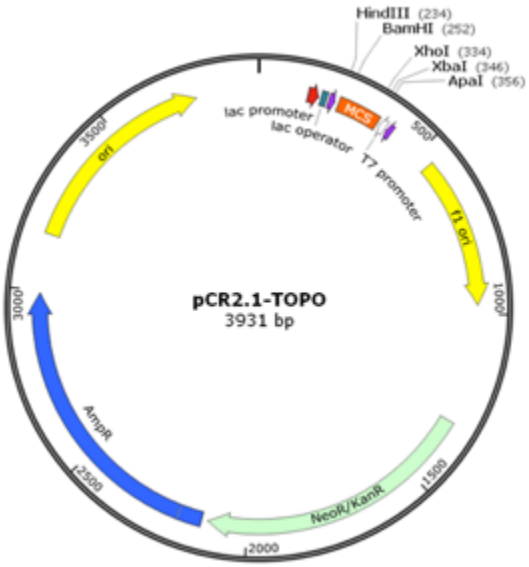

Figure 2.2 pCR2.1-TOPO cloning vector contains a number of features for efficient subcloning. The vector is supplied as a linearized vector containing T overhangs for direct ligation of Taq-amplified PCR products. The T7 promoter and M13 forward and reverse primer sites are present for in vitro RNA transcription and sequencing. EcoR I sites flank the PCR product insertion site for easy excision of inserts. The presence of lac promoter and operator allows for easy blue/white colony screening on X-Gal-IPTG agar plates. Kanamycin and ampicillin resistant sites in the vector allow for the choice of selection in *E. coli*. The vector map was produced using SnapGene Viewer 1.5.3.

2.1.2.1.2 Ligation for TOPO TA cloning

The ligation reaction was performed using 3 µL of the poly-A extended fl-LcrH PCR product, 2 µL of pCR®2.1-TOPO® vector, 1 µL of T4 DNA ligase (NEB, UK), 1 µL of T4 DNA ligase 10 x reaction buffer, 3 µL of sterile deionised distilled water to give total reaction volume of 10 µL. The reaction mixture was incubated at 14 °C for 4 hours.

2.1.2.1.3 Transformation of Ligated *fl-LcrH* in chemically competent cells

The chemically competent cells used for the transformation of the *fl-LcrH* gene cloned in the TOPO TA cloning vector was One Shot® TOP10 *E. coli* cells (Invitrogen™).

One Shot® TOP10 Genotype:

F- *mcrA* Δ(*mrr-hsd*RMS-*mcr*BC) Φ80*lac*ZΔM15 Δ *lac*X74 *rec*A1 *ara*D139 Δ(*araleu*)7697 *gal*U *gal*K *rps*L (StrR) *end*A1 *nup*G

2 µL of the ligation mixture was added to 50 µL of One Shot® TOP10 *E. coli* cells in a sterile microcentrifuge tube and allowed to incubate on ice for 30 minutes. The mixture was

incubated at 42 °C in a water bath for 30 seconds and placed on ice for 2 minutes. 250 µL of LB media was added to the transformed cells and incubated on a shaker (250 RPM) at 37 °C for one hour. After incubation, the cells were centrifuged at 6,000 RPM for 2 minutes; the supernatant was discarded leaving approximately 100 µL of LB media. The cell pellet was resuspended and plated on LB agar plate containing 25 µg/mL of Kanamycin, 20 µg/ml of X-Gal and 0.2 mg/ml of IPTG for blue/white colony screening. The plate was left to incubate at 37 °C overnight and checked the next morning. White colonies represented the *E. coli* cells that contained the *fl-LcrH* gene incorporated into the TOPO TA cloning vector.

2.1.2.1.4 DNA extraction and purification

Representative white colonies were picked using sterile toothpicks, and used to inoculate 5 ml of sterile LB broth containing 50 µg/ml of Kanamycin. This was incubated at 37 °C for 14-16 hours on a shaker (250 RPM). Small-scale isolation of plasmid DNA from these bacterial colonies was then performed (known as minipreparation of plasmid DNA (plasmid miniprep)). This process is based on the alkaline lysis method for extraction of plasmid DNA from a relatively small volume of bacteria and was performed using a QIAprep Spin Miniprep Kit (QIAGEN Ltd.). The plasmid miniprep was carried out using the manufacturer's instructions.

2.1.2.1.5 Estimation of DNA concentration

Plasmid DNA samples obtained from the plasmid miniprep method were diluted using ddH_2O for measurement of DNA concentration. A Shimadzu UV-1601 UV-VIS Scanning spectrophotometer was baselined using ddH_2O as blank sample. 100 µL of the diluted DNA sample was added to a quartz cuvette and a spectrum was measured from 350 to 220 nm. Three differing dilutions for a given DNA sample were prepared and an average of three measured spectra was taken for ensuring accurate DNA concentration measurement. DNA absorbs at 260 nm, hence this wavelength was used to determine the amount of DNA. The following Equation 2.1 was used to measure the concentration of DNA:

Equation 2.1

$$\boldsymbol{DNA\ concentration} = \boldsymbol{A_{260\,nm}} \times \boldsymbol{dilution\ factor} \times \boldsymbol{conversion\ factor}$$

where, A_{260nm} denotes the absorbance at 260 nm; conversion factor is 50 since an absorbance at 260 nm of 1.0 corresponds to 50 ng ml^{-1} of double stranded DNA, the

resultant DNA concentration is measured in ng ml^{-1}. A_{260nm} to A_{280nm} ratio of 1.6 or above indicated pure, contamination free DNA sample.

2.1.2.1.6 Analytical Restriction Digestion with EcoRI

The fl-LcrH gene would be incorporated between *EcoR*I sites in the pCR®2.1-TOPO® vector on successful ligation (the *EcoR*I sites flank the PCR product insertion site in the vector). Hence, the purified plasmid miniprep DNA samples were digested with *EcoR*I restriction enzyme to confirm positive clones. The digestion was carried out using 8 µL of plasmid DNA, 0.5 µL of *EcoR*I restriction enzyme (NEB, UK), 0.5 µL of sterile deionised distilled water, and 1 µL of NEB buffer 2 to give a total reaction volume of 10 µL. The reaction mixture was incubated at 37 °C for 3 hours. The digested bands were visualized on a 1.5 % agarose gel (Section 2.1.1.1.1). Presumptive positive clones were sent for DNA sequencing (Section 2.1.2.1.7) and sequenced using M13 reverse primer.

2.1.2.1.7 DNA sequencing

DNA samples each with a volume of 15 µL of miniprep DNA at a concentration of 100 ng μL^{-1} were prepared in labelled microcentrifuge tube and sent with the correct sequencing primer. DNA sequencing was carried out by Lark Technologies, Essex, UK (now Beckman Coulter Genomics Ltd). The resultant DNA chromatograms were viewed and analyzed using ChromasPro software version 1.34 (Technelysium Pty Ltd.).

2.1.3 Insertion of synthesised *fl-LcrH* gene into an expression vector

Two expression vectors were used for expressing fl-LcrH. These were pProEX-HTb (Invitrogen) and pTrc-GST (designed vector obtained from Prof. A.R. Fersht and based on the pRSETA vector, Life Technologies). These are shown in Figure 2.3. The *fl-LcrH* gene was inserted into these vectors between the restriction sites *BamH*I and *Hind*III.

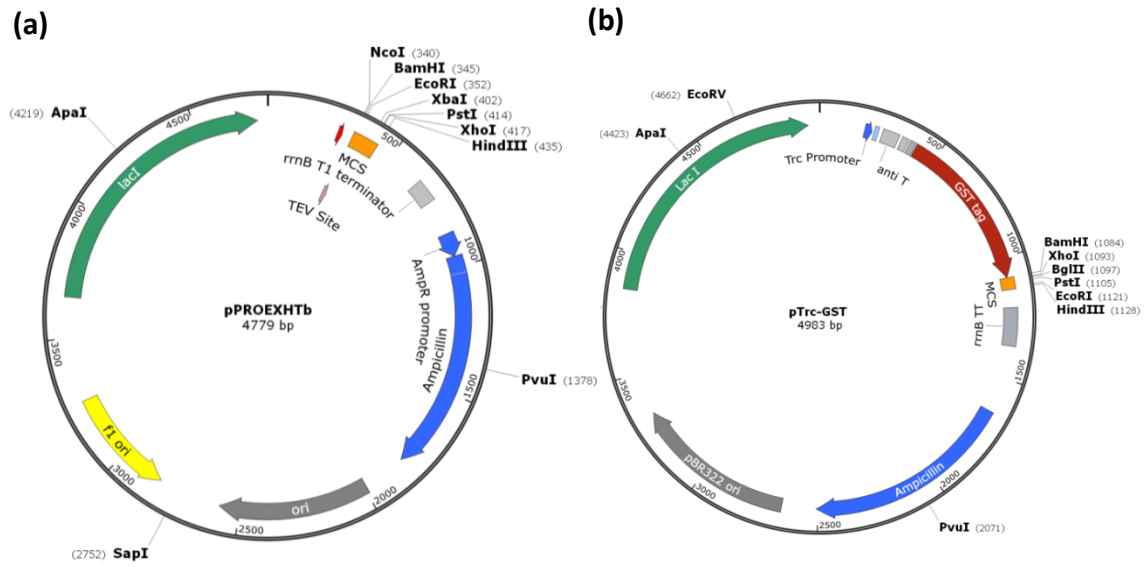

Figure 2.3: pProEX-HTb (a) and pTrc-GST (b) vectors. The vectors contain a number of features including, an ampicillin resistance gene (shown in green colour) that permits the selection of cells carrying the expression vector and multiple cloning site (MCS) shown in orange. The Trc promoter sequence contains part of the tryptophan promoter, part of the lactose promoter and the lactose repressor gene, thus allowing high level of expression when induced with isopropyl β-D-1-thiogalactopyranoside (IPTG). Vector maps were produced using SnapGene viewer version 1.5.2.

2.1.3.1 Restriction digest of *fl-LcrH* gene

Fl-LcrH in the TOPO vector and each expression vector were digested separately using the restriction enzymes *BamH*I and *Hind*III. Due to the star activity of *BamH1* a sequential restriction digestion was carried out. 16 µL of gel purified DNA (PCR product or plasmid vector DNA), 2 µL of NEB buffer 2 (NEB), 1 µL of *Hind*III restriction enzyme (NEB), and incubated for 3 hours at 37 °C. The *Hind*III was then heat deactivation by incubating at 65 °C for 20 minutes and subsequently placed on ice. 0.4 µL of NaCl (5mM stock solution NEB), 0.2 µL of BSA (1 x final concentration from 100 X stock solution, NEB), 1 µL of *BamH*I restriction enzyme (NEB), 0.4 µL of sterile ddH_2O was added to the reaction mixture to give a total volume of 20 µL and incubated for 3 hours at 37 °C. *BamH*I was deactivated by heating the reaction mixture at 65 °C for 20 minutes. The digested DNA samples were visualized on 1.5 % agarose gel (Section 2.1.1.1.1) and DNA bands of correct size were excised and gel purified as below.

2.1.3.2 Purification of DNA from an Agarose Gel

The correct sized DNA band visualized on agarose gel was excised and placed in a PCR tube (the PCR tube was punctured with a hole at the bottom and filled with glass wool), and was placed into a microcentrifuge tube. The lid of the microcentrifuge tube was punctured and the PCR tube containing the excised gel was inserted to fit tightly at the top. This was centrifuged for 10 minutes at 13,000 RPM to separate the DNA from the gel. The gel was held on the glass wool with the DNA in solution collected at the bottom of the microcentrifuge tube. This DNA was then purified from this solution via DNA precipitation using the Pellet Paint Co-Precipitant (Novagen) as per the manufacturer's instructions. The DNA was then re-solubilised in 20 µL of sterile ddH_2O.

2.1.3.3 Ligation

The gel purified digested insert and vector were ligated in a ratio of 3:1 (insert: vector) in terms of volume. The ligation reaction was performed by adding 6 µL of the gel purified insert, 2 µL of the digested vector DNA, 0.5 µL of sterile ddH_2O, 1 µL of T4 DNA ligase 10 x reaction buffer (NEB, UK), 0.5 µL of T4 DNA ligase (NEB, UK) to give a total reaction volume of 10 µL. The reaction mixture was incubated at 4 °C for 14-16 hours. The ligase was deactivated by incubating the reaction mixture at 65 °C for 20 minutes

2.1.3.4 Transformation using Electro-competent cells

The ligation mixture was transformed in electrocompetent XL1-Blue *E. coli* cells (Agilent Technologies). The XL1-Blue strain of *E. coli* allows blue-white colour screening for recombinant plasmids, is an excellent host strain for routine cloning applications using plasmid or lambda vectors and helps in preparation of high quality plasmid DNA.

XL1-Blue Genotype:

recA1 endA1 gyrA96 thi-1 hsdR17 supE44 relA1 lac [F´ *proAB lacI*^{q} *ZΔM15 Tn10* (Tet^r)]

(Genes listed signify mutant alleles. Genes on the F´ episome, however, are wild type unless indicated otherwise).

In order to perform transformation, 1 µL of the ligation mixture was added to 30 µL of XL1-Blue cells (in 10 % glycerol), mixed well and added to 0.2 cm electroporation cuvette (BIORAD). The cuvette was placed into the chamber slide and electroporated using the Bio-Rad Micropulser^{TM}. A pre-programmed electroporation setting called EC2 (voltage of 2.5

kV) was used, as this was the manufacturer's recommended setting. A voltage delivery time of approximately 5 milliseconds after pulsing was an indicator of efficient electroporation. Once pulsed, 1 ml of LB broth was immediately added to the sample and the mixture incubated at 37 °C for 1 hr. The culture produced from the transformation was plated out (≈ 50 µL) onto LB-Agar plates containing ampicillin (100 µg ml^{-1} final concentration) and incubated overnight at 37 °C. Single bacterial colonies were picked the following day, inoculated in 5 ml LB broth containing 100 µg ml^{-1} ampicillin and incubated at 37 °C on a shaker (250 RPM) for 14-16 hours.

2.1.3.5 Confirmation of DNA Clones

To determine whether the ligation had been successful, the isolated DNA was restriction digested (Section 2.1.3.1, except the reaction volume was 10 µL) and run on a 1.5 % agarose gel (Section 2.1.1.1.1). A positive result showed a DNA band that corresponded to the size of the *LcrH* gene (500 bases). The DNA that produced positive restriction digests were then sent for DNA sequencing (Section 2.1.2.1.7).

2.1.4 Synthesis & insertion of truncated *LcrH* (*tr-LcrH*) gene in into pTrc-GST vector

The shortened version, tr-LcrH was synthesized by performing a conventional PCR using *fl-LcrH* in pProEXHTb vector as a template. Oligonucleotides were designed to match the termini of *tr-LcrH* (coding and non-coding strands) with melting temperatures (T_m) of 67–74 °C. The coding oligonucleotide incorporated a *BamH*I and the non-coding oligonucleotide incorporated *Hind*III restriction site at their ends. The reverse oligonucleotide also incorporated a stop codon after the gene sequence, but before the *Hind*III restriction site. The designed sequences were synthesized by Integrated DNA Technologies Inc. and supplied in lyophilised form. They were dissolved in ddH_20 to give a stock concentration of 50 µM. The PCR reaction was performed and success confirmed as described in Section 2.1.1.2.

The correctly sized *tr-LcrH* PCR product was then incorporated into the pTrc-GST vector by a simple restriction digest of vector and gene, followed by DNA extraction, ligation and transformation (Section 2.1.2.1.3). The success was confirmed with analytical restriction digest and DNA sequencing (Section 2.1.3.5).

2.1.5 Synthesis of LE65 mutant of tr-LcrH

In order to create the monomeric L65E LcrH construct, site directed mutagenesis was performed on the pTrc-GST expression vector containing the *tr-LcrH* gene. A point mutation was carried out in the *tr-LcrH* gene, where the 65th amino acid Leucine was mutated to Glutamic acid. Oligonucleotides for the coding and non-coding strand spanning the point mutation site in *tr-LcrH* were synthesized (Integrated DNA Technologies, Inc.) with T_m of 78 °C. Site directed mutagenesis PCR was performed using the QuikChange® Site-Directed Mutagenesis Kit (Stratagene). The formula commonly used for estimating the T_m for the oligonucleotides is shown in Equation 2.2 (QuikChange® Site-Directed Mutagenesis kit instruction manual)

Equation 2.2

$$T_m = 81.5 + 0.41(\%\ GC) - \frac{675}{N} - \%\ mismatch$$

For calculating T_m: N is the primer length in bases, values for % GC and % mismatch are whole numbers.

2.1.5.1 Site Directed Mutagenesis

Site directed mutagenesis was carried out using 1.25 µL each of oligonucleotides for the coding and non-coding strand (125 ng each), 2 µL of template (10 ng of tr-LcrH-pTrc-GST plasmid vector), 5 µL of 10 x reaction buffer (Stratagene), 1 µL of dNTPs (10mM mix), 38.5 µL of ddH_2O and 1 µL of *Pfu* turbo DNA polymerase (2.5 U/µL –Stratagene) to give a total reaction volume of 50 µL in a sterile PCR tube.

The mutagenesis PCR was performed starting with 95 °C of initial denaturation for 30 seconds, followed by a cycle repeated 18 times: denaturation at 95 °C for 30 seconds, annealing temperature of 55 °C for 30 seconds, elongation at 68 °C for 5 minutes 30 seconds (1 minute per kb of plasmid length) and finally 5 minutes of extension at 68 °C in a thermal cycler. 1 µL of *Dpn*I restriction enzyme (10 U/µL) was added to the reaction mixture after the completion of PCR, thoroughly mixed, spun down in a microcentrifuge tube for 1 minute and incubated at 37 °C for 1 hour. This DNA was used to transform XL1-Blue electrocompetent cells (Section 2.1.3.4). Colonies were picked for growing bacterial cultures overnight, followed by isolation and purification of plasmid DNA (Section 2.1.3.2). The

plasmid DNA samples were subjected to analytical restriction digestion with *BamH*I and *Hind*III (Section 2.1.3.1) except that the reaction volume was 10 µL. The restriction digestion was analysed on a 1.5 % agarose gel. DNA samples showing the correct sized bands were selected, sent for DNA sequencing (Section 2.1.2.1.7) and sequencing was carried out using pTrc-His reverse primer.

2.2 Protein Production and Purification

LcrH proteins fl-LcrH, tr-LcrH and monomeric L65E LcrH were produced using the protocol described below.

2.2.1 Protein Production

BL21 C41 (DE3) Electrocompetent strain of *E. coli* cells were transformed (Section 2.1.2.1.3) with expression plasmid vectors pTrc-GST and pProEX-HTb, both carrying the *LcrH* gene respectively. BL21 C41(DE3) cells are *E. coli* strains that are effective in expressing toxic proteins from all classes of organisms, including bacteria, yeast, plant, viruses, and mammals. The C41 strains contain genetic mutations phenotypically selected for conferring tolerance to toxic proteins. The strain C41 (DE3) was derived from BL21 (DE3). This strain has a mutation that reduces the level of T7 RNAP activity, thereby preventing cell death associated with overexpression of many recombinant toxic proteins [178-181].

BL21 C41 (DE3) Genotype: F $^-$ *ompT hsdSB* (r_B^- m_B^-) *gal dcm* (DE3)

Single colonies containing the *LcrH* gene were picked and grown in 10 ml of LB medium containing final concentration of 50 µg/ml ampicillin overnight at 37 °C on a shaker. The 10 ml overnight grown bacterial culture was used to inoculate 1L of 2 x YT + ampicillin in a 2L flask and was grown at 37 °C with constant shaking at 200 RPM until the absorption of the cells at 600 nm (A_{600}) reached 0.6 – 1.0 (≈ 3 – 4 hours). The absorption was monitored using a UV-2401PC UV-Vis recording spectrophotometer. Isopropyl-thio-β-D-galactopyranoside (IPTG) (Melford Laboratories Ltd., UK) was added to a final concentration of 0.1 mM to induce protein expression. The temperature was lowered to 18 °C for improving the stability and solubility of the protein undergoing expression and placed on the shaker overnight (200 RPM). The cells were harvested after 16-18 hours post induction in a

Beckman Avanti J-30I centrifuge and using the JLA 9.1000 rotor for 10 minutes at 4,000 *x g* at 4 °C.

2.2.1.1 Cell Lysis for Protein Extraction

2.2.1.1.1 Cell Lysis by Sonication

The harvested bacterial cell pellet was resuspended in 40 ml of ice-cold 1x PBS containing 10 % glycerol. The cells were lysed by sonication using a Sonics Vibracell Ultrasonic Processor (Sonics & Materials Inc.). The mixture was retained on ice, whilst 6 cycles of 15 seconds on, 45 seconds off, with an output of 30 volts were applied, until the cell mixture became non-viscous and darker in colour. The cell debris was then removed by centrifugation at 33,000 x *g* in Beckman Avanti J-30I centrifuge, in a JA-30.50 rotor for 1 hour at 4 °C.

2.2.1.1.2 Cell Lysis by Homogenisation

The suspension of harvested bacterial cells in ice cold 1X PBS with 10 % glycerol, 5 mM DTT was filtered through a sieve and poured into the inlet of high pressure homogenizer Emulsiflex-C3 (Avestin Inc., Canada). The cell lysis was carried out under pressure of 20,000 lb/in^2 with nitrogen gas according to the manufacturer's instructions. The cells were lysed by two passages through the Emulsiflex-C3 until the lysate became non-viscous and homogenous. The cell lysate was then centrifuged at 33,000 x *g* for 1 hour at 4 °C using Beckman-Coulter JA-30.50 rotor.

2.2.1.2 Purification by Affinity Chromatography

The supernatant protein extracted after cell lysis and subsequent centrifugation was filtered through a 0.2 µm syringe filter (Sartorius Stedim Biotech GmbH, Germany) and subjected to affinity purification. Affinity purification of LcrH proteins was carried out by two methods depending on the expression plasmid used for protein production i.e. pProEX HTb plasmid containing the *fl-LcrH* gene produced a hexahistidine tagged protein whereas pTrc-GST plasmid produced GST tagged proteins:

1) Ni^{2+} affinity chromatography – pProEX HTb plasmid containing the *fl-LcrH* gene produced a hexahistidine-tagged fl-LcrH protein. His-tagged fl-LcrH protein was purified by using Ni^{2+} charged column packed with Iminodiacetic acid agarose resin (Sigma, UK). The resin was

charged with Ni^{2+} by passing 2 column volumes of 100 mM $NiSO_4$ and the unbound $NiSO_4$ was removed with a column volume of 1x PBS.

2) GST-affinity chromatography was used to purify fl-LcrH, tr-LcrH and monomeric L65E LcrH proteins produced from pTrc-GST vector containing the respective genes. GST-tagged proteins were purified by using a column packed with glutathione agarose resin called Super Glu – Glutathione Superflow (Generon, UK).

2.2.1.3 Buffer Solutions

All buffer solutions were made with deionised distilled H_2O (resistance of 18.2 Ω) and vacuum filtered using 0.2 µm membrane filter (Whatman) prior to usage. The names of buffers and their respective compositions are shown in Table 2.1.

Table 2.1: Buffer solutions and their compositions

Name of buffer	Buffer composition
His-tag Wash buffer	1x PBS (137 mM NaCl, 10 mM phosphate, 2.7 mM KCl), pH 7.4
His-tag Elution buffer	50 mM phosphate, 150 mM NaCl, 250 mM Imidazole, pH 7.0
GST Wash buffer	20 mM phosphate, 150 mM NaCl, pH 7.2, 5 mM DTT
GST Elution buffer	20 mM phosphate, 150 mM NaCl, 10 mM reduced glutathione, pH 7.2, 5mM DTT

2.2.1.4 Ni^{2+} Affinity chromatography and cleavage of His-tagged proteins

The filtered supernatant was loaded onto a Ni^{2+} affinity column pre-equilibrated with his-tag wash buffer. After passing the supernatant protein through the Ni^{2+} affinity column (column volume = 10 ml), it was washed with 20 column volumes of his-tag wash buffer. The protein was eluted with his-tag elution buffer. After elution, the column was washed with 2 column volumes of 6 M GdmHCl to unfold any residual protein bound to the column. The column

was then washed with 5 column volumes of ddH_2O, followed by 2 column volumes of 20 % ethanol and stored at 4 °C. The eluted protein was cleaved overnight at 25 °C by addition of TEV protease to remove the fused N-terminal His-tag. The affinity purification and cleavage of LcrH was monitored by visualisation on SDS-PAGE (Section 2.2.2.2).

2.2.1.5 GST Affinity purification and cleavage of GST-tagged proteins

The filtered supernatant was loaded onto the GST affinity column (column volume = 10 ml) and washed with 20 column volumes of GST wash buffer. LcrH – GST fusion protein was cleaved on the resin overnight at 25 °C by addition of thrombin protease (GE Healthcare, UK). The cleaved LcrH was eluted as a flow through in the GST wash buffer. The bound GST-tag was removed from the column by the addition of GST elution buffer. The column was subsequently washed with two column volumes of 6 M GdmHCl to unfold and remove any residual proteins bound to the column. The column was immediately washed with 5 column volumes of ddH_2O, followed by 2 column volumes of 20 % ethanol and stored at 4 °C.

2.2.1.6 Purification using Size Exclusion Chromatography by AKTA FPLC

The final step in the purification used size exclusion chromatography using AKTA FPLC system (GE Healthcare) by loading the cleaved LcrH protein fractions onto a HiLoad™ 16/60 Superdex™ 200 gel filtration column (GE Healthcare, UK) with a bed volume of 120 ml. The column was equilibrated with 180 ml of 50 mM phosphate buffer, 5 mM DTT, pH 7.0. The cleaved LcrH protein fractions were concentrated using Amicon® Ultra Centrifugal Filter units (Millipore) and filtered through 0.2 µm syringe filter (Sartorius Stedim Biotech GmbH, Germany). The protein samples (under 10 ml volume) were loaded onto the gel filtration column with a 50 ml superloop (GE Healthcare). 1 column volume of 50 mM phosphate buffer, 5 mM DTT, pH 7.0 was applied to the column at a flow rate of 1 ml/min. Fractions were collected in 2.5 ml aliquots, in 30 mm tubes.

2.2.2 Protein Purity

Mass spectrometry (Section 2.2.2.1) and SDS-PAGE (Section 2.2.2.2) of the proteins confirmed both the size and checked the purity, respectively. In all cases the purity of LcrH proteins was greater than 95 %. The nucleic acid contamination of the protein was checked by the 280/260 nm ratio. A ratio of 1.6 or above indicated no contamination.

2.2.2.1 Mass Spectrometry

Sample and Matrix preparation

A fresh saturated matrix solution for MALDI-ToF was prepared in a microcentrifuge tube by dissolving Sinapinic acid (Formula weight = 224.21) in 50 % acetonitrile, 0.1 % TFA in ddH_2O. The mixture was vortexed for 1 minute and centrifuged for 20 seconds to remove any undissolved matrix from the solution and the clean top matrix was used. Protein samples of 30 µM concentration were given ZipTip® (Millipore) treatment as per manufacturer's instructions. Sample and matrix solutions were mixed in the ratio of 1: 4 in a microcentrifuge tube. 0.5 µL of the mixture was immediately loaded onto a MALDI plate and allowed to dry at room temperature prior to insertion into the mass spectrometer.

Mass spectra were recorded on a Micromass TofSpec mass spectrometer (Micromass, Manchester, UK), equipped with nitrogen UV laser (337 nm with a 4 nm pulse width).

2.2.2.2 SDS-Polyacrylamide Gel Electrophoresis

All solutions were made as described in the laboratory manual [181,182]. SDS-PAGE was carried out according to standard protocols using the Laemmli system [182,183]. LcrH protein samples were resuspended in SDS loading buffer (50 mM Tris-HCl, pH 6.8, 100 mM DTT, 2% SDS, 0.1% bromophenol blue, 10% glycerol), boiled for 10 minutes and loaded on an 18% SDS-PAGE gel for analysis.

2.2.3 Determination of Protein Concentration

Protein concentration was determined spectrophotometrically, using the UV-2401PC-UV-Vis recording spectrophotometer, according to Equation 2.3.

Equation 2.3

$$C = \left(\frac{A_{280} - A_{320}}{\varepsilon l}\right) x\ dilution\ factor$$

Where C is the protein concentration in M. A_x is the absorbance at x wavelength. ε is the molar extinction coefficient, and l is the cuvette path length in cm.

The molar extinction coefficient at 280 nm wavelength, $\boldsymbol{\varepsilon}_{280\ \mathrm{nm}}$ is calculated by Equation 2.4 [183,184]:

Equation 2.4

$$\boldsymbol{\varepsilon}_{280\,nm} = (\#\ \mathrm{Trp})\ (5500) + (\#\ \mathrm{Tyr})\ (1490) + (\#\ \mathrm{Cys})\ (125)$$

Where '# Trp' refers to the number of tryptophan residues, '# Tyr' refers to the number of tyrosine residues and '# Cys' refers to the number of cysteine residues in the protein. The molar extinction coefficient ($\boldsymbol{\varepsilon}_{280\,nm}$) for the LcrH proteins are as follows; for fl-LcrH, 12,420 M^{-1} cm^{-1}, tr-LcrH and mutant L65E LcrH, 10,805 M^{-1} cm^{-1}.

2.2.4 Storage of Purified Protein

The LcrH proteins were dialysed into 50 mM Tris, pH 8.0, 5 mM DTT overnight at 4 °C. They were then concentrated using centrifugal concentrators (Millipore) to ≈ 100-200 µM and 1 ml aliquots in micro-centrifuge tubes were rapidly frozen using liquid nitrogen. The samples were then stored at -80 °C.

2.3 Biophysical Characterization of LcrH proteins

In all experiments, 50 mM phosphate, pH 7.0, 5 mM DTT buffer was used. The molarity of the stock solutions of urea was determined using a refractometer (model NAR-1T, Atago, Tokyo).

2.3.1 Multimeric state of LcrH proteins using Analytical Size Exclusion Chromatography (SEC)

In order to determine the multimeric state of LcrH proteins, analytical SEC was performed on an AKTA FPLC system (GE Healthcare). This was done by injecting 100 µL of protein at concentrations from 3 µM to 100 µM in 50 mM Phosphate buffer, pH 7.0, 5 mM DTT onto a Superdex™ 75 10/30 column and Superdex™ 200 10/30 column (GE Healthcare). The column was pre-equilibrated with LcrH buffer before injection of protein samples. 1 column volume of 50 mM Phosphate buffer, pH 7.0, 5 mM DTT, was applied at a flow rate of 0.5 ml/min. For the SEC experiments involving urea denatured protein samples, the column

and protein sample was pre-equilibrated for 4 hours and run with the required concentration of urea.

2.3.2 Analytical Ultracentrifugation (AUC)

Two types of sedimentation experiment can be performed using an analytical ultracentrifuge; sedimentation equilibrium and sedimentation velocity. Sedimentation velocity experiments involve spinning molecules at a high speed and looking at the rate at which the molecules move in response to the centrifugal force that is generated. From the rate at which the molecules move, a sedimentation coefficient can be determined (as the centrifugal force is known). Information regarding the shape and sometimes aggregation/oligomerisation state can be determined, although the latter parameter is more easily determined by sedimentation equilibrium experiments. In contrast, sedimentation equilibrium experiments involve spinning molecules at moderate speeds so that centrifugal force causes the protein to sediment gradually, creating a concentration gradient across the cell, whilst diffusive forces act to oppose the sedimentation forces. Eventually these two forces are in equilibrium and so no net movement of the concentration gradient is observed. This gradient can then be measured and from knowing how this concentration gradient is affected by changing rotor speed, molecular masses (and hence oligomerization states) can be determined. Masses can be determined accurately as, at equilibrium, the concentration distribution is only dependent on the mass of the sedimenting species and not on its shape (unlike for sedimentation velocity experiments). If a species is self-associating, dissociation constants can often be obtained if they are in the range measurable by the instrument (usually between 1 μM – 0.5 mM, depending on the absorbance of the molecule in question). All experiments performed on this system are sedimentation equilibrium experiments as this is the method used when an accurate, shape-independent molecular weight is required.

Aimee Boyle from School of Chemistry, University of Bristol performed sedimentation equilibrium experiments on the analytical ultracentrifuge. The experiments were conducted using a Beckman-Optima XL-I analytical centrifuge fitted with an An-60 Ti rotor. Solutions were prepared at 40 μM protein concentration in 50 mM Phosphate buffer, pH 7.0, 5 mM DTT. Data was recorded at 25 °C using speeds in the range 17,000 – 30,000 rpm. Datasets

were initially fitted to a single, ideal species model using the program Ultrascan [184,185] which employed the Equation 2.5.

Equation 2.5

$$C(x) = exp\left\{\frac{[\ln(A)+M\,\omega^2(1-\bar{\nu}*D)\,(x^2-x_r^2)]}{2\,R\,T}\right\} + B$$

Where C(*x*) is the concentration of peptide as a function of radial position (M), A is the measured absorbance of the sample, M is the molar mass of the species (Da), ω is the angular velocity of the rotor (rad s^{-1}), $\bar{\nu}$ is the partial specific volume of the protein in question (ml g^{-1}), D is the solvent density (g ml^{-1}), x^2 is the radial position (cm^2), x_r^2 is the reference radial position (cm^2), R is the gas constant (J mol^{-1} K^{-1}), T is the temperature (K) and B is a baseline offset which compensates for any non-ideality in the data acquisition or the cells.

The partial specific volume of the peptide (0.7341 cm^3 g^{-1}) and the density of the solvent (1.0042 g cm^{-3}) were calculated using Sednterp. A monomer-dimer equilibrium model (Equation 2.6) was used to determine the K_D of the species. A fit was deemed appropriate if the residuals from the fit were randomly scattered and had an absorbance close to zero. Any trends in the residuals indicated a different model was required.

The monomer-dimer equilibrium model was used for determining the dimerization dissociation constant K_D after performing equilibrium sedimentation is shown in Equation 2.6.

Equation 2.6

$$C_T = C_M(R_0)\exp\left[M\varphi(R^2 - R_0^2) + \left(\frac{2}{K_D * M}\right)[C_M(R_0)]^2\exp\left[2M\varphi(r^2 - r_0^2)\right]\right.$$

Where C_T is the total protein concentration, R_0 is the reference radius (cm), R is the radius (cm) and $C_M(R_0)$ is the monomer concentration at R_0, M is the molecular weight of monomer, $\varphi = \frac{\omega^2(1-\bar{\nu}*D)}{2RT}$, ω is the angular velocity of the rotor (rad s^{-1}), $\bar{\nu}$ is the partial specific volume of the protein in question (ml g^{-1}), D is the solvent density (g ml^{-1}), R is the gas constant (J mol^{-1} K^{-1}) and T is the absolute temperature (K).

The protein concentration (C_T) *versus* radius (r) plots were analysed to determine K_D of the species according to the above theoretical Equation 2.6 for monomer-dimer equilibrium. Least squares curve fitting was performed using the Ultrascan software. Errors were obtained by Monto Carlo analysis and given with 5 % confidence limit.

2.3.3 Dynamic Light Scattering (DLS)

Dynamic light scattering (DLS), also known as quasi-elastic light scattering (QELS) and photon correlation spectroscopy (PCS), is a non-invasive, well-established technique in the field of protein crystallography. DLS is used to measure hydrodynamic sizes, polydispersities and aggregation effects of protein samples in solution [185,186]. Apart from proteins, its applications include emulsions, micelles, polymers, nanoparticles or colloids. It measures the size and size distribution of molecules in the submicron region, and with the latest technology lower than 1nm. In DLS, a laser beam illuminates the sample and the Brownian motion of particles or molecules in suspension scatters the laser light at different intensities. Analysis of these intensity fluctuations yield the velocity of the Brownian motion and hence the particle size using the Stokes-Einstein relationship [186,187] (Equation 2.7).

Equation 2.7

$$R_h = \frac{k_B T}{6\pi\eta D}$$

Where, R_h is the hydrodynamic radius, k_B is Boltzmann constant, T is temperature, η is the solvent viscosity and D is the translational diffusion coefficient (obtained through the velocity of Brownian motion by DLS).

DLS measurements were carried out using Zetasizer Nano S instrument (Malvern Instruments Ltd). Protein samples were prepared at concentrations of 50 µM in 50 mM phosphate buffer, pH 7.0, 5 mM DTT. For experiments involving urea denatured protein samples, the protein sample was pre-equilibrated for 4 hours and run with the required concentration of urea. All samples were spun at 10,000 rpm for 10 minutes before taking measurements. The results were analyzed by Zetasizer software version 6.12 (Malvern Instruments Ltd).

2.4 Secondary and Tertiary Structure Characterization

2.4.1 Circular Dichroism (CD) Spectroscopy

Circular Dichroism (CD) Spectroscopy is a spectroscopic technique where the CD of molecules is measured over a range of wavelengths. CD is the difference in the absorption of left and right handed circularly polarised light in chiral (structurally asymmetrical) molecules and occurs when a molecule contains one or more chiral chromophores (light-absorbing groups). Depending on the CD instrument, the data are recorded as either as the difference in absorbance of right- and left-handed circularly polarised light, $\Delta A(\lambda) = A_L(\lambda) - A_R(\lambda)$, or as ellipticity, θ_{obs} in degrees or millidegrees. Data in both formats can be converted to molar values, that is, to the differential molar circular dichroic extinction coefficient, $\Delta\varepsilon = \varepsilon_L - \varepsilon_R$ and to the molar ellipticity, $[\theta]$. $\Delta\varepsilon$ and $[\theta]$ are related by Equation 2.8.

Equation 2.8 $$[\boldsymbol{\theta}] = \mathbf{3300} \quad \boldsymbol{\Delta\varepsilon}$$

It should be noted that the concentration standards are different for $[\theta]$ and $\Delta\varepsilon$. $\Delta\varepsilon$ is the differential absorbance of a 1 mol/l solution in a 1 cm cell , whereas $[\theta]$ is the rotation in degrees of a 1 dmol/cm^3 solution and a path length of 1 cm.

The principle of CD involves a monochromatic beam of light passing through a Photo Elastic Modulator (PEM) that converts the linear polarised light into alternating left and right handed polarised light. The two polarisations are differently absorbed by the chiral sample, and the detector called Photo Multiplier Tube (PMT) [187-189], detects this difference in absorption and conveys the CD signal. Along with the CD signal, the CD spectropolarimeter also records the High Tension (HT) voltage of the detector. This HT voltage is a measure of the amount of voltage the detector is using and is dependent on the amount of light striking the detector (more light – lower HT voltage). Furthermore, HT voltage is roughly proportional to the absorbance of the sample. If the HT voltage goes above ~800 Volts the noise will become disproportionate to the sample signal and the output will be completely unreliable (Jasco J-715 Spectropolarimeter Operating Manual).

CD spectroscopy is widely used to study a range of chiral molecules, but its most important application is in the study of large biological molecules. Largely, it is used for analysis of the

secondary structure or conformation of proteins, as secondary structure is sensitive to environment, temperature or pH. CD can be used to monitor secondary structural changes with environmental conditions or interaction with other molecules. Structural, kinetic and thermodynamic information about proteins can be derived from CD spectroscopy [188-190].

Far-UV (spectral region 190-250 nm) CD was used to probe the secondary structure of the LcrH protein at different protein concentrations and denaturant concentrations. Spectra were acquired on either a Jasco J-715 CD Spectropolarimeter (JASCO, UK) or a Chirascan™ CD Spectrometer (Applied Photophysics Ltd, UK). All far-UV CD spectra were acquired in LcrH buffer, at 25 °C. The following pathlengths were used: 10 or 5 mm pathlengths for protein concentrations at 3 µM; 1, 2 or 5 mm path lengths for proteins concentrations at 6, 12 and 25 µM and 1 mm path length for protein concentrations at 50 µM and 80 µM. Spectra were recorded from 200 to 300 nm. To compare data, and thus correct for pathlength and concentration, all ellipticities were converted to molar ellipticity (degrees cm^2 $dmol^{-1}$), shown in Equation 2.9.

Equation 2.9

$$[\theta]_{molar} = \left(\frac{100 \times \theta_{obs}}{d \times m}\right)$$

Where, $[\theta]_{molar}$ is molar ellipticty in deg cm^2 $dmol^{-1}$, θ_{obs} is the observed CD signal in millideg, d is the cuvette path length in cm and m is molar concentration of protein.

2.4.2 Fluorescence Spectroscopy

Fluorescence is a phenomenon where a molecular system absorbs, then emits light. During absorption, high energy (short wavelength) light excites the system, promoting electron within the molecule to move from the ground state, to the excited state [190,191]. Emission is observed when the excited electron returns from the excited state back to the ground state. As some energy is always lost by non-radiative processes, such as vibrational transitions, the energy of the emitted light is always lower than that of the absorbed light [191,192]. The energies and relative intensities of the fluorescence signals give an indication about the structure and environment of the fluorophores (substances that exhibit fluorescence).

Fluorescence spectrophotometer also called Spectrofluorimeter or Fluorimeter is a device for measurement of fluorescence of proteins that contain intrinsic fluorophores (naturally occurring fluorophores) such as tryptophan, tyrosine and phenylalanines. A typical fluorescence spectrophotometer contains a sample holder, incident photon source (a xenon lamp), monochromators for selecting particular incident wavelengths, focussing optics, photon-collecting detector and a control software unit. The detector is usually set at 90° to the light source. A fluorescence emission spectrum is recorded when the excitation wavelength is held constant and the emission beam is scanned as a function of wavelength. A fluorescence spectrophotometer detects the changes in fluorescence intensity, which enables the study of the tertiary structural changes of proteins or binding of two molecules. For example, the wavelength of tryptophan fluorescence can be used to determine whether a tryptophan is in an aqueous environment (longer wavelength) or buried deep within the protein (shorter wavelength) [192,193].

All measurements were performed in a thermostatted cuvetter holder at 25 °C using a Varian Cary Eclipse Fluorescence Spectrophotometer (Agilent Technologies). Tyrosine fluorescence was employed due the lack of Tryptophan residues in LcrH. The excitation wavelength was 274 nm and band passes for excitation and emission was 5 nm. The fluorescent emission of the LcrH protein was measured from 294 to 400 nm. The λ_{max} of 303 nm (emission wavelength for tyrosine) was used in analysis unless otherwise stated.

2.5 Equilibrium Studies for measuring Thermodynamic Stability

2.5.1 General Background

The thermodynamic stability of proteins can be investigated by performing unfolding studies under equilibrium conditions. These experiments involve unfolding the protein by varying one parameter (concentration of chemical denaturant, temperature, pH and pressure) and utilising a probe (fluorescence and circular dichroism) to measure the equilibrium produced. In this study, chemical denaturations were performed using urea and circular dichroism (Section 2.4.1) was used to monitor the changes in secondary structure. Fluorescence spectroscopy (Section 2.4.2) was used to measure the changes in tertiary structure. The far UV spectra from 200 to 300 nm monitored the secondary structure of the

protein. LcrH proteins are alpha helical containing three TPRs in each monomer, thus depicted in a negative peak at 222 nm.

2.5.2 Equipment and General Procedures

All experiments, unless otherwise stated, were carried out at 25 °C in 50 mM Phosphate buffer, pH 7.0, 5 mM DTT. All stock solutions of urea were made using volumetric flasks, and the urea solutions were flash frozen and stored at -20 °C to prevent degradation. All protein solutions were filtered 0.2µm syringe filter prior to addition to denaturant solutions. GdmHCl and urea solutions were checked by a refractometer (model NAR-1T, Atago, Tokyo), using Equation 2.10 and Equation 2.11 respectively [168,193].

Equation 2.10

$$Molarity = 57.1\ (\Delta N) + 38.7\ (\Delta N)^2 - 91.6\ (\Delta N)^3$$

Equation 2.11

$$Molarity = 117.7\ (\Delta N) + 29.7\ (\Delta N)^2 + 185.5\ (\Delta N)^3$$

Where, $\Delta \boldsymbol{N}$ is the difference in refractive index between the denaturant solution and 50 mM Phosphate buffer, pH 7.0, 5 mM DTT.

2.5.3 Preparation of Samples for Equilibrium Chemical Denaturation

A stock solution of GdmHCl (≈ 8 M) or urea (≈ 10 M) was diluted with ddH_2O (resistance of 18.2 Ω) to obtain a large range of denaturant concentrations using a Hamilton Microlab dispenser (Hamilton Company). The protein and denaturant stock solutions were filtered through 0.2 µm syringe filter. Cuvettes of differing path lengths were used depending on the protein concentration for the denaturation experiment. Smaller path length cuvette was used to scan higher protein concentration samples to prevent saturation of the detector. The preparation of samples for different protein concentrations and the use of cuvettes of suitable path lengths have been described as follows.

2.5.3.1 Sample preparation for LcrH protein concentrations 1 to 12 µM

Experiments involving denaturation of protein samples from 1 to 12 µM, a 9 x stock solution of protein (9 to 108 µM) and buffer (450 mM Phosphate buffer, pH 7.0, 45 mM DTT) was prepared. 100 µL of this 9 x stock solution was added to 800 µL of denaturant sample resulting in a 1 x concentration of proteins ranging from 1 to 12 µM. Cuvettes of path lengths 10 mm (for 1 µM LcrH), 5 mm (for 3 µM and 6 µM LcrH) and 2 mm (for 12 µM) were used for performing far-UV CD scans.

2.5.3.2 Sample preparation for LcrH protein concentrations 25 to 80 µM

A 6x stock solution of protein (150 to 480 µM) and buffer (300 mM Phosphate buffer, pH 7.0, 30 mM DTT) was prepared for conducting experiments involving protein samples from 25 to 80 µM. 50 µL of this 6 x stock solution was added to 250 µL of denaturant sample resulting in a 1x concentration of proteins ranging from 25 to 80 µM. The final conditions were 50 mM Phosphate buffer pH 7.0, 5 mM DTT. 1 mm path length cuvette was used to perform far-UV CD scans for LcrH protein with concentrations 25 to 80 µM.

The protein/denaturant solutions were pre-equilibrated at 25 °C for a minimum of 4 hours prior to performing experiments on the CD. Scans were taken in a thermostatted cuvette holder at 25 °C $\pm$ 0.2 °C and between 210 nm and 250 nm at a scan rate of 1 nm s^{-1}. The largest difference in signal between native and denatured LcrH was observed at 222 nm, and this wavelength was used to monitor unfolding. For easy comparison of differing data sets, the CD signal at 222 nm (λ_{obs}) was converted to relative spectroscopic signal (λ_{rel}) using Equation 2.12.

Equation 2.12

$$\lambda_{rel} = \frac{(\lambda_{obs} - \lambda_N)}{(\lambda_D - \lambda_N)}$$

Where λ_{obs} is the observed CD signal, λ_N is the signal of the native state and λ_D is the signal of the denatured state.

Chapter 3 Gene Construction, Purification Strategy and Initial Biophysical Characterisation of LcrH proteins

3.1 Introduction

This chapter describes the following: (i) gene construction of full length LcrH (fl-LcrH), truncated LcrH (tr-LcrH) and monomeric L65E LcrH, (ii) purification strategies of these three constructs and (iii) initial biophysical characterisation - oligomeric state, conditions under which these oligomeric states were maintained (i.e. abrogation of any aggregation) and secondary structure characterisation.

3.2 Experimental approaches

Genes were constructed using PCR and site directed mutagenesis. Protein purification was carried out using affinity and size exclusion chromatography. SDS-PAGE gels and Mass Spectrometry followed protein purification. Once purified, analytical size exclusion chromatography was used to determine oligomeric state and conditions under which these oligomeric states were maintained. Finally, protein secondary structure was analysed using far-UV circular dichroism (CD).

3.3 Results

3.3.1 Full length LcrH (fl-LcrH) gene construction

The fl-LcrH gene sequence was obtained from NCBI Reference Sequence: NC_009595.1 showing 507 bp region from 55032 to 55538. The translated protein sequence of full length LcrH, comprising of 168 amino acids, is shown in Figure 3.1.

(a)

```
  1 ATG CAA CAA GAG ACG ACA GAC ACT CAA GAA TAC CAG CTG GCA ATG
 46 GAA TCC TTC CTA AAA GGA GGG GGA ACT ATC GCC ATG CTC AAC GAA
 91 ATT TCA AGT GAC ACT TTA GAG CAA CTC TAC TCT CTT GCA TTT AAC
136 CAA TAC CAG TCA GGA AAA TAC GAG GAT GCT CAC AAG GTC TTT CAA
181 GCT CTC TGT GTG CTA GAC CAC TAT GAT TCA CGT TTC TTT TTA GGG
226 CTA GGC GCT TGT CGT CAA GCC ATG GGG CAA TAC GAC TTA GCG ATT
271 CAT AGC TAC AGC TAT GGC GCC ATA ATG GAT ATA AAA GAA CCT CGT
316 TTT CCG TTT CAT GCG GCC GAA TGT TTA CTG CAA AAG GGA GAG CTT
361 GCT GAA GCA GAA AGT GGC TTG TTC TTG GCT CAA GAG CTT ATC GCA
406 GAC AAA ACT GAG TTT AAG GAG CTT TCC ACC CGA GTT AGC TCA ATG
451 TTA GAA GCA ATT AAA TTG AAA AAG GAG ATG GAA CAT GAG TGC GTT
496 GAT AAC CCA TGA
```

(b)

```
1.......10 ........20 ........30 ........40 ........50 ........60
MQQETTDTQE YQLAMESFLK GGGTIAMLNE ISSDTLEQLY SLAFNQYQSG KYEDAHKVFQ

........70 ........80 ........90 .......100 .......110 .......120
ALCVLDHYDS RFFLGLGACR QAMGQYDLAI HSYSYGAIMD IKEPRFPFHA AECLLQKGEL

.......130 .......140 .......150 .......160 .....168
AEAESGLFLA QELIADKTEF KELSTRVSSM LEAIKLKKEM EHECVDNP
```

Figure 3.1: Full length LcrH (fl-LcrH) (a) gene NCBI Reference Sequence: NC_009595.1 showing 507 bp region from a *Yersinia pestis* CA88-4125 plasmid pCD1 and (b) fl-LcrH protein sequence with accession no. AAA27642 in FASTA format. Sequences are numbered in red and amino acids are shown in black.

The fl-LcrH gene was constructed using recursive PCR (2.1.1.1) where eight coding and non-coding oligonucleotides spanning the entire length of the gene were used. Each oligonucleotide overlapped with its neighbour by 20 bases (Figure 2.1). The resultant recursive PCR product was run on 1% agarose gel (2.1.1.1.1) and showed a range of DNA sizes from ~100 – 500 bp (Figure 3.2a). This is expected and is caused by recombination and extension of oligonucleotides by different amounts. In order to obtain a full length LcrH

gene from the recursive PCR mixture, a conventional PCR was performed using the recursive PCR product as the template and PCR primers encoding the 5' and 3' of the gene with additional restriction sites (BamHI and HindIII at the 5' and 3' end, respectively) (Figure 3.3). Figure 3.2b showed that the PCR yielded DNA bands of ~500 bp which corresponds to the correct size of *fl-LcrH* gene (504 bp). The PCR product was then gel purified (section 2.1.3.2) and inserted into pProEX HTb (section 2.1.3) and pTrc-GST (section 2.1.4) vector for protein expression. DNA sequencing of the genes within the pProEX HTb and pTrc-GST vectors confirmed correct gene sequence had been synthesised.

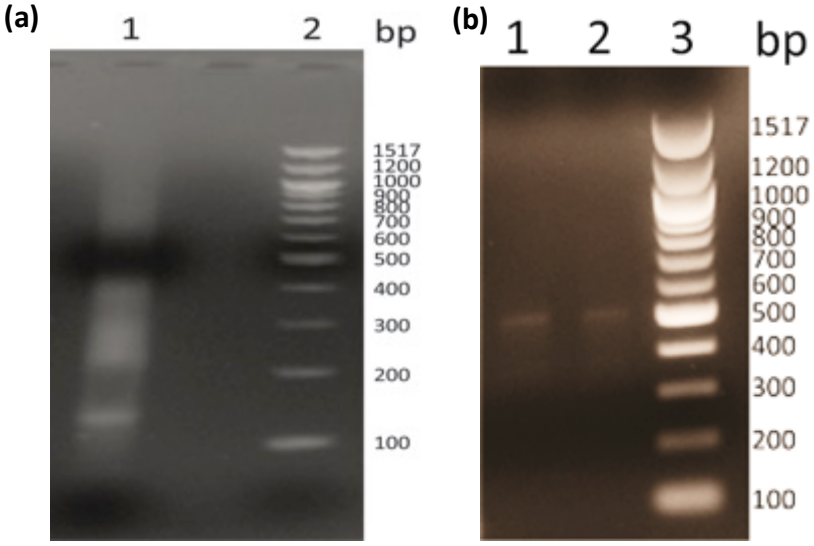

Figure 3.2 (a) 1% agarose gel of recursive PCR of fl-LcrH gene. Lane 1 - recursive PCR product of *fl-LcrH* gene showing a range of DNA sizes ranging from ~100 to 500 bp, lane 2 - 1 Kb DNA ladder. (b) 1.5% agarose gel showing PCR product of *fl-LcrH* gene. Lanes 1&2 contain the PCR product of *fl-LcrH* gene showing DNA bands of ~500 bp. Lane 3: 100 bp DNA ladder.

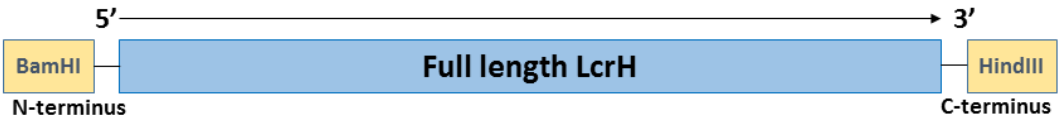

Figure 3.3 Schematic showing the incorporated restriction sites of BamHI and HindIII at the 5' and 3' termini respectively of the full length LcrH gene using conventional PCR.

3.3.2 Production and purification of full length LcrH (fl-LcrH)

The pProEX HTb vector (section 2.1.3) expressed the fl-LcrH as a fusion protein with an N-terminal hexahistidine tagged protein. Protein expression was carried out in the *E. coli*

expression strain BL21 C41 (DE3). The conditions that gave the greatest soluble protein were found to be growth at 37 °C until an OD_{600nm} of 0.6 was reached and then induction with 0.1 mM IPTG at 27 °C for 14-16 hours. The fl-LcrH protein expression at different time points is shown in Figure 3.4.

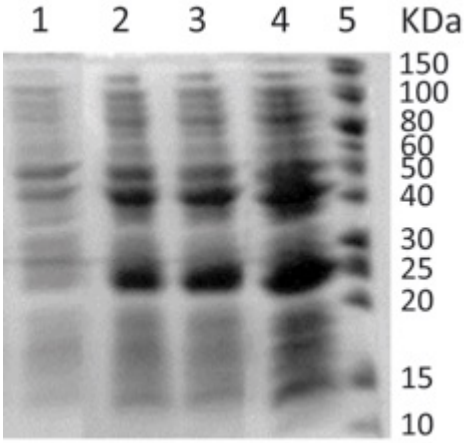

Figure 3.4: 15 % SDS-PAGE gel showing the production of his-tagged fl-LcrH protein at different time points. Lanes 1, 2, 3 and 4 are lysed bacterial cell pellets after induction with 1mM IPTG at time t = 0 hrs, t = 2 hrs, t = 4 hrs and t = 16 hrs respectively. Lane 5 – protein ladder. The protein production was induced with IPTG at 16 °C and bacterial cells were grown overnight before harvesting for proteins.

Native Purification: Fl-LcrH was extracted from the bacterial cells (Section 2.2.1.1) and subjected to affinity chromatography using Ni^{2+} column (Section 2.2.1.4). The his-tagged fl-LcrH protein was eluted (Figure 3.5a) and the his-tag cleaved using TEV protease (Figure 3.5b). Fl-LcrH has a molecular weight of 19 KDa and on the SDS-PAGE gel in Figure 3.5b, the cleaved fl-LcrH is observed as band of ≈ 20 KDa. However, there was a significant proportion of fl-LcrH found to be present in the insoluble pellet after sonication (inclusion bodies).

Denatured Purification: The insoluble pellet (I) was re-suspended in a denaturing lysis buffer (1x PBS, pH 7.0, 6 M GdmHCl, 10 % glycerol, 5 mM DTT), sonicated on ice, centrifuged and the resultant supernatant was subjected to affinity chromatography using a Ni^{2+} column pre-equilibrated with 5 column volumes of lysis buffer. The Ni^{2+} column was then washed with reducing concentrations of GdmHCl to gradually fold the bound proteins on the column before finally washing with 1 x PBS, pH 7.0, 10 % glycerol to completely remove the any trace of GdmHCl. The his-tagged fl-LcrH was then eluted using the his-tag elution buffer (section 2.2.1.2) and the his-tag from the protein was cleaved by TEV protease (Figure 3.5b).

Purification of fl-LcrH: Both natively purified and denatured purified cleaved fl-LcrH was then subjected to size exclusion chromatography to remove residual TEV protease and other protein impurities (section 2.2.1.6). Figure 3.5(c) shows the size exclusion chromatography (SEC) profile of fl-LcrH purification. The inset in Figure 3.5(c) shows the SDS-PAGE gel of the protein fractions eluted from the SEC of fl-LcrH. In the SDS-PAGE gel, lane 2 contains the protein fraction loaded onto the SEC, lanes 3-5 show higher molecular weight impurities and lane 6 onwards fl-LcrH band ~19 kDa can be observed. Lanes 6 & 7 showed considerable amount of higher molecular weight proteins co-eluting with fl-LcrH. The SDS-PAGE gel lanes 8-11 contained relatively higher purity of fl-LcrH protein. Thus, it became clear that the purified fl-LcrH samples obtained after the final SEC contained higher molecular weight impurities. Therefore, to increase purity to 95 % an additional wash step was introduced in the nickel column step. Here, the columns were washed with 1x PBS containing low concentration of imidazole (5 mM) before elution with his-tag elution buffer. However, the co-elution of higher molecular weight impurities could not be completely avoided. Both purification strategies are summarised in Figure 3.5 and achieved more than 90 % purity. Protein fractions corresponding to the lanes 8-11 in the inset Figure 3.5 (c) were pooled and concentrated as more than 90 % purity was achieved.

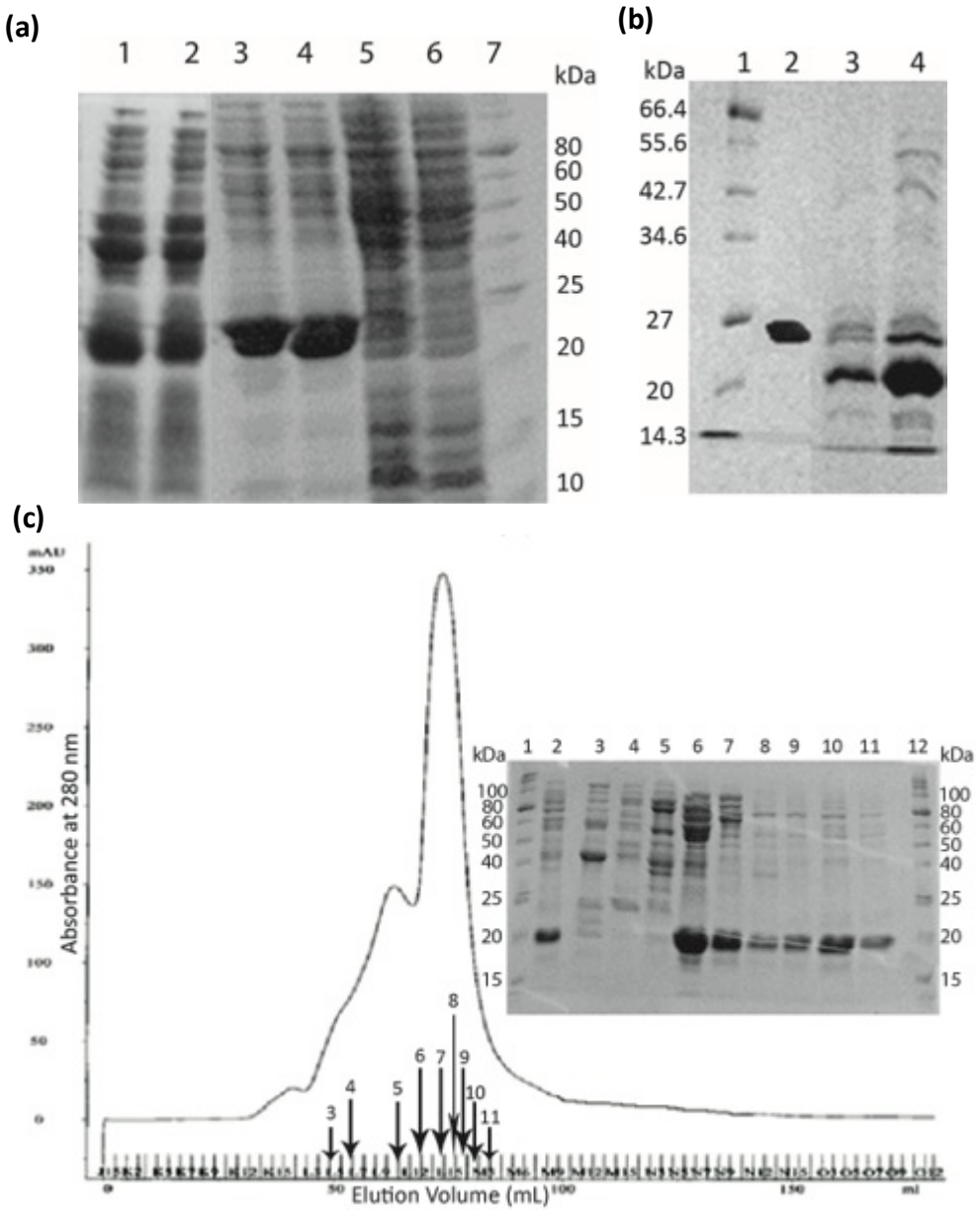

Figure 3.5 15% SDS PAGE gel showing (a) elution profile of his-tagged fl-LcrH. Lanes from left left to right, Lane 1 – supernatant containing soluble protein (s), lane 2 – supernatant from re-solubilized inclusion bodies (I), lane 3 – eluted fl-LcrH from soluble supernatant (s), lane 4 – eluted fl-LcrH from re-solubilized inclusion bodies (I), lane 5 – flow through (f/t) from (s), lane 6 – flow through (f/t) from (I), lane 7 – protein ladder. (b) Cleavage of his-tag from fl-LcrH (combined elutions from soluble supernatant and re-solubilised inclusion bodies) using TEV protease, lane 1- protein ladder, lane 2 – uncleaved his-tagged fl-LcrH, lanes 3 and 4 – cleaved fl-LcrH. (c) Size exclusion chromatography profile of cleaved fl-LcrH, the chromatogram showing the elution of fl-LcrH and the 15 % SDS-PAGE gel (inset) showing the eluted protein fractions. Lanes from left to right, lane 1 & 12– protein ladder, lane 2 – cleaved fl-LcrH sample loaded on the FPLC, lane 3-11: eluted protein fraction from SEC. The protein fractions loaded onto the SDS-PAGE gel are shown as the corresponding lane numbers on the SEC chromatogram.

In order to attain higher levels of protein purity, the *fl-LcrH* gene was inserted in pTrc-GST expression vector (section 2.1.3). The pTrc-GST vector produces the fl-LcrH as an N-terminally GST tagged fusion protein (section 2.2.1.5). As before the vector was transformed in BL21 C41(DE3) expression strain of *E. coli* and grown in an identical manner to that used for producing his-tagged fl-LcrH mentioned i.e. bacterial growth at 37 °C until reaching an $O.D_{600\ nm}$ of 0.6. However, expression was induced with 0.1 mM IPTG at 16 °C for 14-16 hours. The fl-LcrH protein was then extracted from bacterial cells (section 2.2.1.1) and subjected to affinity purification by passing it through a column containing glutathione agarose resin pre-equilibrated with GST wash buffer (section 2.2.1.3). Thrombin protease was added to the resin bound with the GST-fl-LcrH fusion protein for cleavage on column in order to separate the GST tag from fl-LcrH protein. The fl-LcrH eluted from the column as a flow through while the GST tag remained bound to the glutathione agarose resin. The protein production and purification of GST-tagged fl-LcrH followed by thrombin cleavage is shown in Figure 3.6.

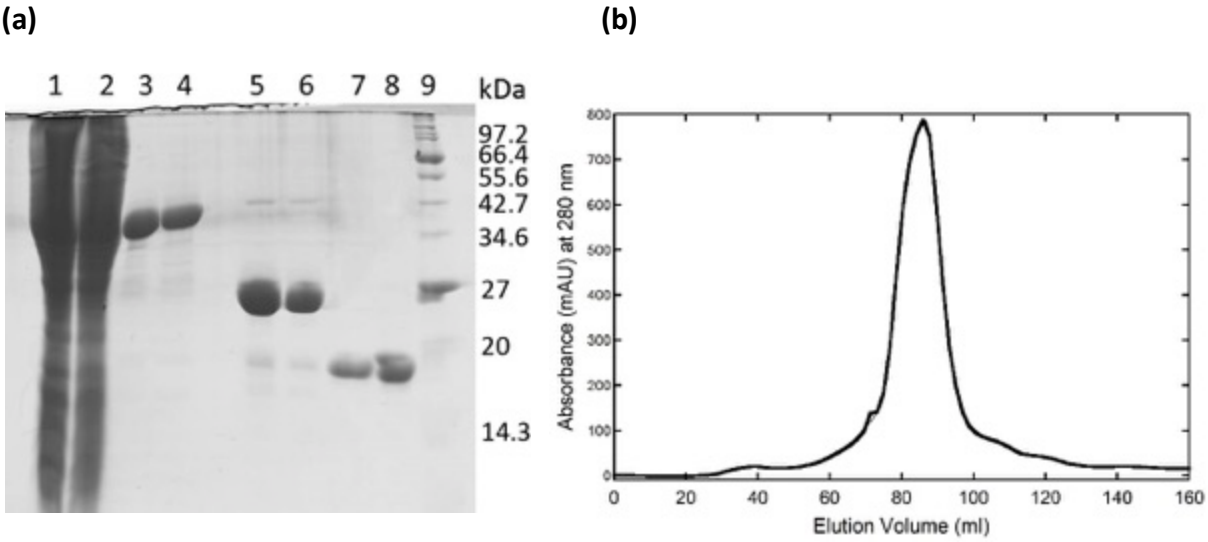

Figure 3.6 (a) 18 % SDS-PAGE showing the protein production and elution profile of GST-tagged fl-LcrH protein. Lanes from left to right: lane 1 - lysed cells, lane 2 – supernatant protein, lanes 3 & 4 – GST-fusion fl-LcrH protein bound to the glutathione agarose resin, lanes 5 & 6 – cleaved GST tag bound to the glutathione agarose resin, lanes 7 & 8 – fl-LcrH protein, lane 9 – protein marker. The GST tag was cleaved using thrombin protease to achieve fl-LcrH protein of ≈ 19 kDa. (b) Chromatogram showing size exclusion profile of fl-LcrH using S200 16/60 column. The fl-LcrH protein fractions from 60 – 110 ml were pooled and concentrated further.

The fl-LcrH protein bands of ≈ 19 kDa can be clearly observed in the 18 % SDS-PAGE gel (Figure 3.6a) after cleavage with thrombin protease. The affinity purified fl-LcrH protein was further concentrated and subjected to size exclusion chromatography for removal of thrombin (Figure 3.6b). The fl-LcrH protein obtained using the GST-tagged fl-LcrH fusion method was easier to purify, provided a greater yield and was of higher purity in comparison to his-tagged fl-LcrH (> 95 % vs. < 90 %, respectively).

3.3.3 Truncated LcrH (tr-LcrH)

After the successful expression and purification of fl-LcrH, it proved to be relatively unstable and prone to aggregation on concentrating (discussed more fully later in this chapter). Moreover, soon after we had purified fl-LcrH the crystal structure of SycD was published. This is the same protein as LcrH but found in *Yersina enterocolitica.* The sequence identity of both proteins is extremely high with only two variant amino acid positions (position 136 and 138 – Figure 3.7 a). Importantly, the paper showed that the construct used to obtain crystals was a shortened version of SycD (tr-SycD) that was more stable and less prone to aggregation. This shortened construct spanned from position 21 to 163. The N-terminal deletion removed a mostly unstructured region, whereas the C-terminal deletion removed a solvent exposed cysteine. It was therefore decided that we should also obtain a truncated LcrH (tr-LcrH).

(a)

```
Sequence      1........10........20........30........40........50........60
  SycD        MQQETTDTQEYQLAMESFLKGGGTIAMLNEISSDTLEQLYSLAFNQYQSGKYEDAHKVFQ
  tr-SycD     --------------------GGGTIAMLNEISSDTLEQLYSLAFNQYQSGKYEDAHKVFQ
  fl-LcrH     MQQETTDTQEYQLAMESFLKGGGTIAMLNEISSDTLEQLYSLAFNQYQSGKYEDAHKVFQ
  tr-LcrH     --------------------GGGTIAMLNEISSDTLEQLYSLAFNQYQSGKYEDAHKVFQ

  Sequence    .........70........80........90........100.......110.......120
  SycD        ALCVLDHYDSRFFLGLGACRQAMGQYDLAIHSYSYGAIMDIKEPRFPFHAAECLLQKGEL
  tr-SycD     ALCVLDHYDSRFFLGLGACRQAMGQYDLAIHSYSYGAIMDIKEPRFPFHAAECLLQKGEL
  fl-LcrH     ALCVLDHYDSRFFLGLGACRQAMGQYDLAIHSYSYGAIMDIKEPRFPFHAAECLLQKGEL
  tr-LcrH     ALCVLDHYDSRFFLGLGACRQAMGQYDLAIHSYSYGAIMDIKEPRFPFHAAECLLQKGEL

  Sequence    .........130.......140.......150.......160.......
  SycD        AEAESGLFLAQELIANKPEFKELSTRVSSMLEAIKLKKEMEHECVDNP
  tr-SycD     AEAESGLFLAQELIANKPEFKELSTRVSSMLEAIKLKKEMEHE-----
  fl-LcrH     AEAESGLFLAQELIADKTEFKELSTRVSSMLEAIKLKKEMEHECVDNP
  tr-LcrH     AEAESGLFLAQELIADKTEFKELSTRVSSMLEAIKLKKEMEHE-----
```

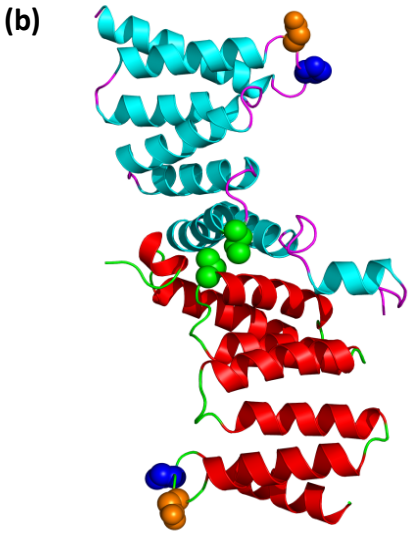

Figure 3.7: (a) Multiple sequence alignment of protein sequences of SycD and tr-SycD from *Yersinia enterocolitica* (both shown in black) with fl-LcrH and tr-LcrH (both shown in dark red) from *Yersinia pestis*. Asparagine 'N' in SycD and tr-SycD is aspartic acid 'D' both in fl-LcrH and tr-LcrH and is highlighted in yellow. Proline 'P' in SycD and tr-SycD is Threonine 'T' both in fl-LcrH and tr-LcrH and is highlighted in turquoise. The 65th Leucine residue is highlighted in green and was changed to Glutamic acid to obtain monomeric tr-SycD and L65E tr-LcrH. Amino acid sequence numbers are shown in red. This figure was generated by ClustalW multiple alignment software. (b) Ribbon representation of head-to-head conformation of dimeric SycD$_{21\text{-}163}$ (tr-SycD) from *Yersinia enterocolitica* which is 99 % identical to tr-LcrH from *Yersinia pestis*. tr-LcrH differs from SycD in only two positions (N136D and P138T). Asparagine and Proline at amino acid positions 136 and 138 are shown in yellow and blue spheres respectively. The 65th leucine residue is shown in green spheres and was mutated to glutamic acid to obtain the monomeric L65E LcrH. Chains A and B of SycD$_{21\text{-}163}$ are coloured cyan and red respectively. Figure was prepared using PyMOL.

The *tr-LcrH* gene was constructed by PCR with the fl-LcrH gene as template and a forward primer starting at the DNA codons of the 21st amino acid and a reverse primer starting from DNA codons of the 163rd amino acid (Figure 3.8). Both primers possessed a BamHI and HindIII restriction sites, respectively for insertion into the pTrc-GST expression vector (Section 2.1.4).

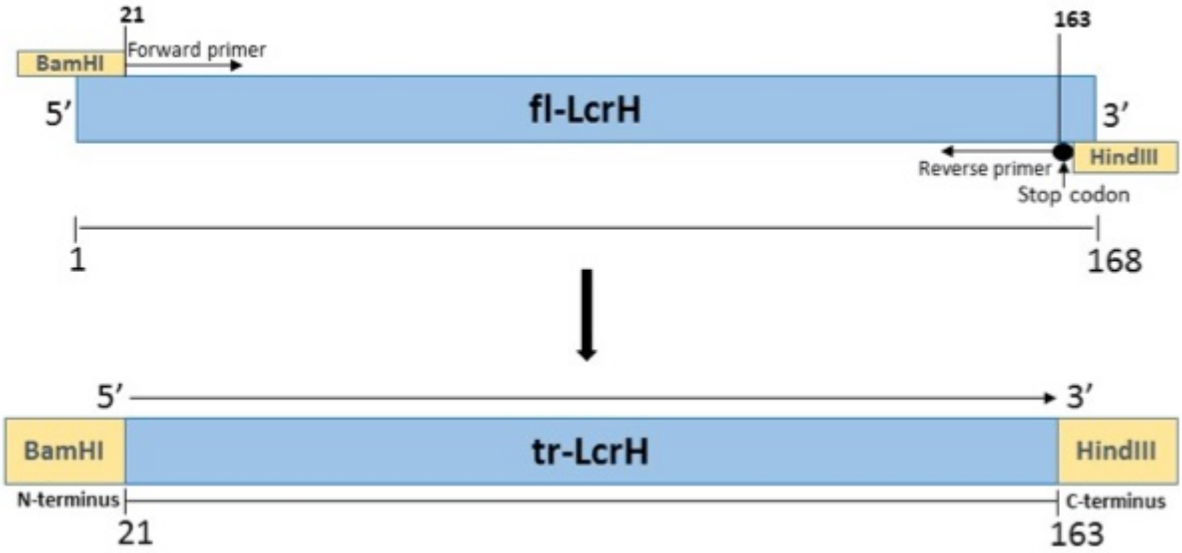

Figure 3.8 Schematic representing the construction of tr-LcrH through PCR using fl-LcrH as template, forward primer spanning the DNA encoding 21st amino acid with BamHI restriction site, reverse primer spanning the DNA encoding the 163rd amino acid which also included a stop codon and HindIII restriction site. The resultant PCR product obtained is shown as the shortened tr-LcrH spanning amino acids from position 21-163.

The pTrc-GST vector inserted with *tr-LcrH* gene was transformed into XL-1 Blue strain of *E. coli* (section 2.1.3.4) followed by isolation of DNA from individual colonies. This was followed by restriction digestion of the isolated DNA using BamHI and HindIII (section 2.1.4) in order to screen the colonies that yielded DNA containing correctly sized insert. Those with a DNA size of ~430 base pairs (Figure 3.9) were sent for DNA sequencing. DNA sequencing confirmed that tr-LcrH gene was successfully cloned in pTrc-GST vector (section 2.1.2.1.7).

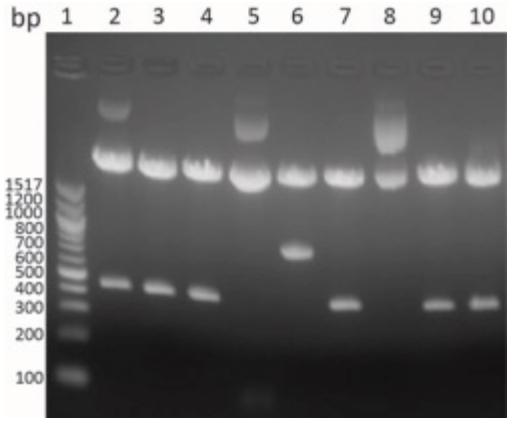

Figure 3.9 1.5 % agarose gel showing restriction digestion of *tr-LcrH* gene from pTrc-GST vector. Lane 1 shows 100 bp DNA ladder. Lanes 2, 3, 4, 7, 9 and 10 show DNA band of ~430 bp corresponding to correct size of *tr-LcrH* gene.

3.3.4 Expression & Purification of Truncated LcrH (tr-LcrH)

As before the pTrc-GST vector containing the *tr-LcrH* gene was transformed into BL21 C41 (DE3) expression strain of *E. coli* to produce GST-tagged tr-LcrH protein. The protocol for GST-tagged tr-LcrH protein production was identical to that used for the production of GST-tagged fl-LcrH production (Section 2.1.4). The protein production and elution profile of GST-tagged tr-LcrH is shown in Figure 3.10(a). The GST-tag was cleaved off the tr-LcrH protein by using thrombin protease giving a band of ≈ 16 kDa shown in Figure 3.10b.

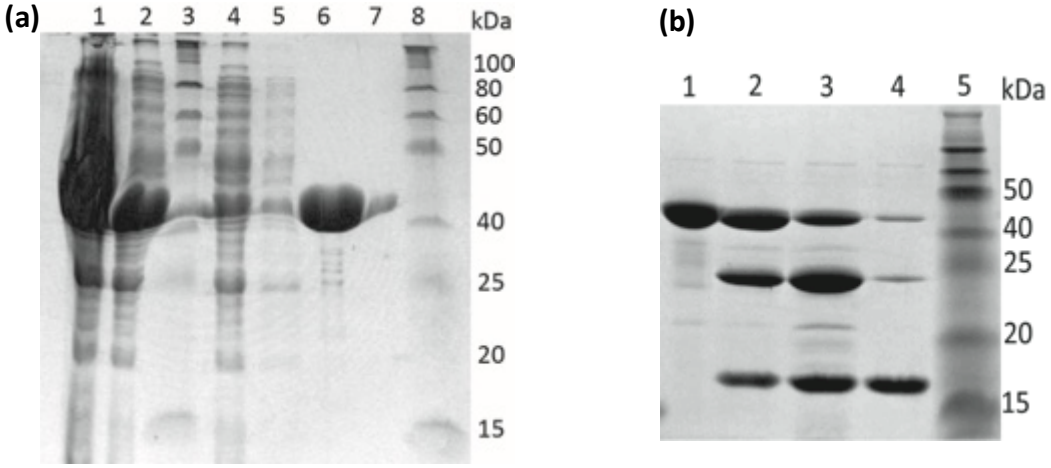

Figure 3.10 18 % SDS-PAGE gel showing (a) protein production of GST-tagged tr-LcrH: Lane 1 – lysed cells, lane 2 – supernatant protein, lane 3 – protein marker, lane 4 – flow through, lane 5 – wash, lanes 6 & 7 – GST-tagged tr-LcrH bound to glutathione agarose resin, lane 8 – protein marker. (b) Cleavage of GST tag from tr-LcrH using thrombin protease. Lane 1 – GST-tagged tr-LcrH bound to the glutathione agarose resin, lanes 2-4 – thrombin protease induced cleavage for separation of GST tag from tr-LcrH on the glutathione agarose resin, lane 5 – protein marker.

The tr-LcrH protein was concentrated and further subjected to purification by size exclusion chromatography (Section 2.2.1.6), which ensured the removal of thrombin protease and enabled to achieve more than 95 % purity. The protein samples eluted from the size exclusion chromatography we loaded on an 18 % SDS-PAGE gel (Section 2.2.2.2) to check for the level of purity, shown in Figure 3.11. The tr-LcrH protein samples eluted from the size exclusion chromatography column showed bands of ≈ 16 kDa more than 95 % purity. Thus, tr-LcrH was successfully produced and purified.

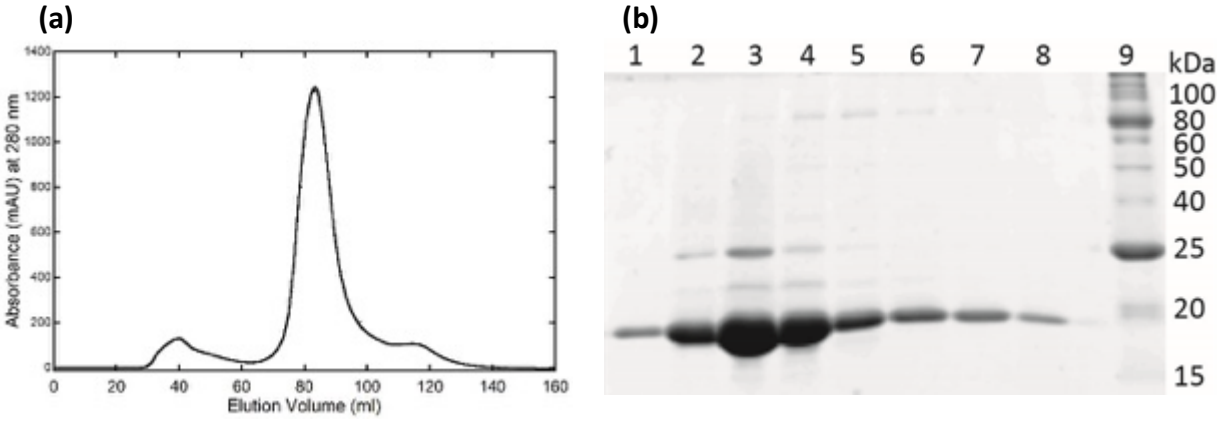

Figure 3.11: (a) Size exclusion chromatography profile of tr-LcrH using S200 16/60 column. (b) 18 % SDS-PAGE gel showing tr-LcrH protein samples purified by size exclusion chromatography. Lanes 1 to 8 are tr-LcrH SEC fractions from 70 ml until 110 ml with each fraction of 5 ml volume.

3.3.5 Construction of L65E tr-LcrH

The study that described the crystal structure of SycD (and thus obviously LcrH) also showed that a single amino acid mutation could render the SycD dimer monomeric [168,194]. This mutation was L65E (Figure 3.7). It was, therefore, important that we also obtained this monomeric version of LcrH. To obtain LE65 tr-LcrH site directed mutagenesis was performed on the pTrc-GST expression plasmid containing the *tr-LcrH* gene (Section 2.1.5). Confirmation of the mutation was obtained through DNA sequencing by Beckman Coulter Genomics Ltd. (Section 2.1.2.1.7).

3.3.6 Expression and Purification of L65E tr-LcrH

The protein was produced using the protocol identical to that used for the production of GST-tagged fl-LcrH (Section 3.3.2) and GST-tagged tr-LcrH (Section 3.3.3) proteins. The protein samples were loaded onto an 18 % SDS-PAGE for analysis and Figure 3.12 shows the protein production, affinity purification and cleavage of the GST tag using thrombin protease.

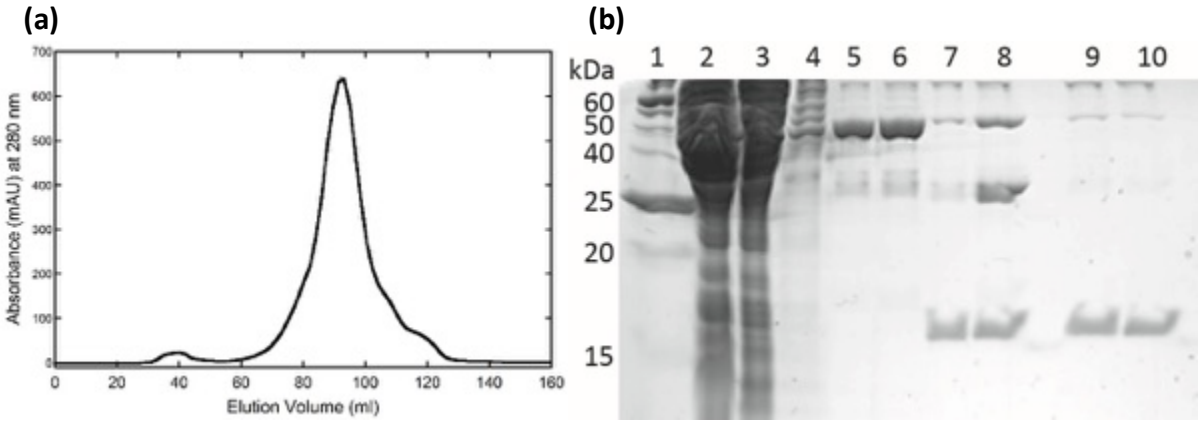

Figure 3.12: (a) Size exclusion chromatography elution profile of L65E tr-LcrH using Superdex 200 16/60 column. Eluted protein fractions from 70-115 ml were pooled and concentrated further. (b) 18 % SDS-PAGE gel showing the GST-tagged L65E tr-LcrH production, its affinity purification profile and cleavage of GST tag using thrombin protease. Lane 1 – protein ladder, lane 2 – lysed cells, lane 3 – supernatant protein, lane 4 – flow through, lanes 5 & 6 – resin sample showing the bound GST-tagged L65E tr-LcrH, lanes 7 & 8 – resin sample showing the thrombin cleavage of GST-tagged L65E tr-LcrH, lanes 9 &10 – eluted L65E tr-LcrH showing a band ≈ 16 KDa, identical to tr-LcrH protein.

The eluted L65E tr-LcrH after cleavage of GST-tag showed a pure L65E tr-LcrH band of ≈ 16 kDa, identical to tr-LcrH (Figure 3.11 (b)). L65E tr-LcrH was then subjected to size exclusion chromatography for the removal of thrombin protease and achieve more than 95 % purity. Importantly, the size exclusion chromatography showed that the LE65 mutant eluted at a larger volume than tr-LcrH (~95 ml vs ~80 ml). This is consistent with LE65 tr-LcrH being monomeric and tr-LcrH being dimeric.

3.3.7 Initial characterization of LcrH constructs

3.3.7.1 Defining buffer & protein concentrations to maintain "native" oligomeric states of LcrH constructs

During the purification of all LcrH constructs it was obvious that they were prone to aggregation. This manifested itself mainly during concentration steps where: (i) protein concentration was lost and (ii) UV-Vis absorbance showed high signal at 320 nm. Therefore it was important to define suitable buffer and protein concentrations conditions were they would remain in "native" oligomeric states.

Buffer conditions were chosen by: (i) calculating the isoelectric point (pI) of the proteins using the ExPASy – ProtParam tool [166-168,194] and (ii) choosing a pH that was 2 pH units away from the pI. The theoretical pI of the proteins is as follows: 4.70 for fl-LcrH, 4.95 for tr-LcrH and 4.87 for L65E tr-LcrH. Thus, 50 mM phosphate buffer at pH 7.0 was chosen (this, fortuitously, also emulated physiological conditions). Phosphate buffer was also chosen as it can specifically stabilise certain proteins. In addition 5 mM DTT was added to prevent disulphide bond formation.

To determine what protein concentrations these buffer conditions enabled (i.e. no aggregation was observed) the proteins were firstly concentrated until protein loss was observed through gain of UV absorbance at 320 nm and loss at 280 nm. The highest non-aggregating concentrations for fl-LcrH, tr-LcrH and LE65 tr-LcrH were 300 µM, 500 µM and 150 µM, respectively. To confirm whether these conditions were stable over 1 week, each protein was concentrated to the aforementioned value and subjected to analytical SEC (Section 2.3.1). They were then stored at 4 °C for one week and then analytical SEC was repeated. Figure 3.13 shows the analytical SEC traces for each LcrH protein before and after 1 week at 4°C.

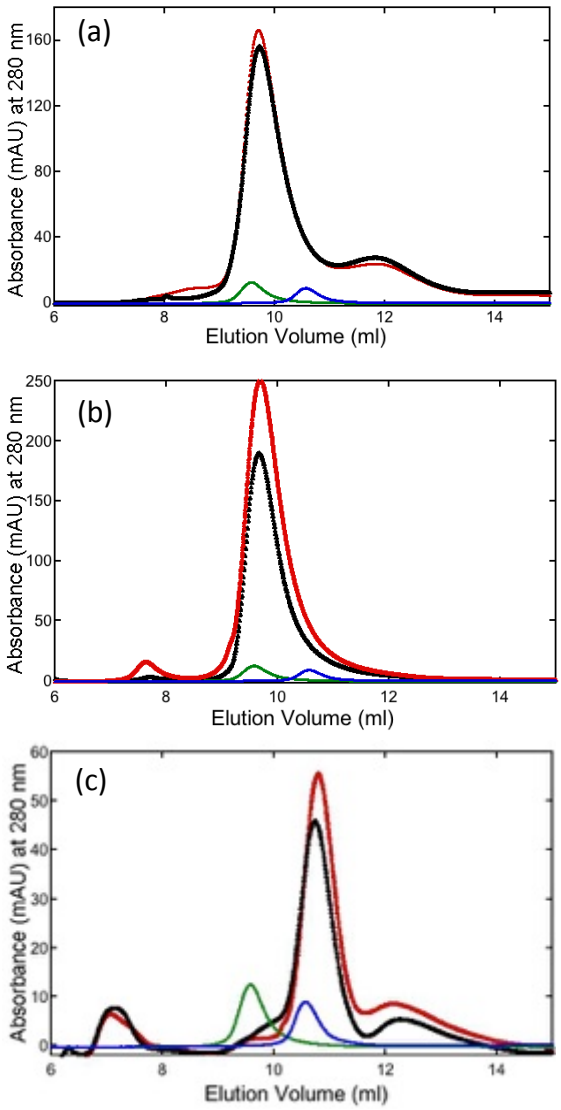

Figure 3.13 Analytical size exclusion chromatography profile of LcrH proteins using Superdex^{TM} 75 10/30 column before and after 1 week: (a) fl-LcrH at 300 µM, (b) tr-LcrH at 500 µM and (c) L65E tr-LcrH at 150 µM. The elution profile in black denotes the first analytical SEC run for the respective LcrH protein samples at the aforementioned protein concentrations. The elution profile in red denotes the analytical SEC of the same protein samples stored for 1 week at 4 °C. TPR standards: CTPR3 (blue) and CTPRa6 (green). Each protein sample at the respective concentrations was loaded using 100 µl sample loop in 50 mM Phosphate, pH 7.0, 5 mM DTT at 25 °C. Figure was prepared using KALEIDAGRAPH 4.0.

Figure 3.13(a) did not show any evidence of aggregation in the protein samples. The elution peak for both samples i.e. before and after storage at 4 °C was ≈ 9.8 ml. However, a tailing peak at ≈ 11-13 ml was observed in both sample runs, which can be attributed to protein degradation. Figure 3.13 (b) shows the analytical SEC profile for tr-LcrH at 500 µM before and after storage at 4 °C. The elution profile for both sample runs was identical. The

difference in the absorbance peaks between the two samples could be attributed to the variability in sample runs. The analytical SEC profile for L65E tr-LcrH at 150 µM was indistinguishable for both sample runs. The elution volume for both sample runs was ≈ 10.8 ml. Additionally, the elution volumes of both tr-LcrH and fl-LcrH are close to that of the dimeric TPR standard CTPRa6 (10.55 ml). Thus, confirming the dimeric oligomeric state of tr-LcrH and fl-LcrH. Figure 3.13 (c) represents the analytical SEC profile of monomeric mutant L65E tr-LcrH. Both elution profiles for L65E tr-LcrH are nearly identical. The elution profiles gives an indication of aggregation (small elution peaks before the void volume (V_o) = 8.5 ml) and some degradation products (tailing peaks) in both sample runs.

On comparing the analytical SEC profile of LcrH proteins at their respective protein concentrations it was observed that over the course of one week the proteins did not undergo significant changes. This confirmed that the highest non-aggregating protein concentrations determined for each of LcrH protein constructs and the buffer conditions used were stable over time. As can be seen all proteins were stable over this time course at their respective concentrations with little loss of protein. This was confirmed by obtaining the concentration of each protein by UV-Vis absorbance at 280 nm before and after one week at 4 °C.

The elution profiles of the protein samples before and after one week storage at 4 °C were identical. For fl-LcrH, tr-LcrH and L65E tr-LcrH this equated to peak elution volumes of ~9.6 ml, ~9.8 ml and ~10.8 ml respectively. The tailing peak in the fl-LcrH elution profile is consistent with slight degradation (similar in both runs). The slight difference in the size of the elution peaks is simply due to the variability of the UV-Vis detector of the AKTA FPLC. The protein concentration was confirmed by obtaining UV-Vis absorbance at 280 nm of each protein before and after one week prior to each analytical SEC run. Interestingly, a difference in size of the elution peaks of LcrH proteins was observed. The peak sizes for LcrH proteins were in the following order: fl-LcrH>tr-LcrH>L65E tr-LcrH. This is suggestive of fl-LcrH and tr-LcrH being dimeric and L65E tr-LcrH monomeric (discussed in Chapter 4).

3.3.7.2 Far-UV circular dichroism of native LcrH constructs

To confirm that the conditions used above produced correctly folded LcrH constructs far-UV CD spectra were obtained (section 2.4.1). Figure 3.14 shows the native and urea denatured far-UV CD spectra of fl-LcrH, tr-LcrH and L65E tr-LcrH at 3 µM (spectra measured in 5 mm path length cuvette) and 50 µM (spectra measured in 1 mm path length cuvette) respectively. The native spectra clearly show correctly alpha-helically folded protein, as they possess minima at 222 nm and 208 nm. Interestingly the fl-LcrH has approximately 10 % greater signal at 222 nm than both tr-LcrH and its LE65 mutant (which are identical). When 8 M urea is added to LcrH proteins there is a complete loss of secondary structure as shown by the disappearance of the minima at 208 & 222 nm.

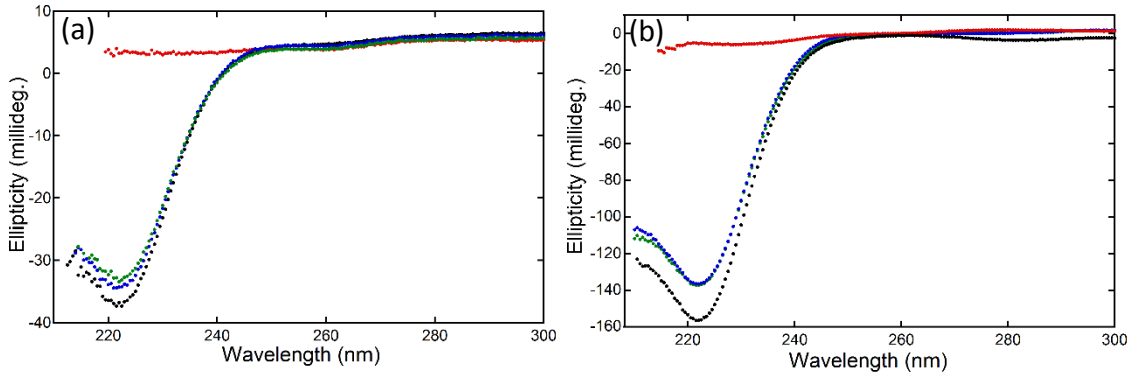

Figure 3.14 Far-UV CD spectra comparing native fl-LcrH (black), tr-LcrH (blue). L65E tr-LcrH (green) and denatured L65E tr-LcrH in 8 M urea (red) for concentrations: (a) 3µM (spectra measured using 5 mm path length cuvette) and (b) 50µM (spectra measured using 1 mm path length cuvette) The detector on the CD spectrophotometer became saturated with HT voltage exceeding 850 volts after 212 nm for samples in 5 mm cuvette and after 208 nm for samples in 1 mm path length cuvette. Figure was prepared using KALEIDAGRAPH 4.0.

In the above Figure 3.14, far-UV CD spectra for LcrH protein samples at 3 µM and 50 µM, were masked beyond wavelengths at 212 nm and 208 nm respectively because the HT voltage of the detector of the CD spectropolarimeter increased to above 800 volts. This is because if the HT voltage goes above ~800 volts the noise becomes disproportionate to the sample signal and the output is completely unreliable (Section 2.4.1 and Jasco J-715 Spectropolarimeter Operating Manual).

3.3.8 Conclusion

The three protein constructs of LcrH – fl-LcrH, tr-LcrH and L65E tr-LcrH were successfully produced and purified. We were able to define suitable buffer and protein concentration conditions for maintenance of native oligomeric states of the respective proteins through analytical size exclusion chromatography. Far-UV CD spectroscopy enabled to confirm that the conditions used produced correctly folded proteins. In the following chapter we explore the oligomeric states and thermodynamic stability of LcrH protein constructs.

Chapter 4 Oligomeric State, Flexibility and Thermodynamic Stability of LcrH protein constructs

4.1 Introduction

In this chapter we explore the oligomeric state, flexibility and thermodynamic stability of each of our constructs of LcrH. These investigations enable the dissection of the role of oligomeric state and stability on LcrH's biological function.

4.2 Experimental Approaches

The monomer-dimer equilibrium and the oligomeric state of the different constructs of LcrH was determined by analytical size exclusion chromatography, dynamic light scattering and analytical ultracentrifugation We then examine the thermodynamic stability and flexibility of our different LcrH constructs by performing equilibrium unfolding through chemical denaturation. The unfolding was monitored by far-UV circular dichroism and fluorescence spectroscopy as probes for secondary and tertiary structures respectively.

4.3 Results

4.3.1 Oligomeric States of LcrH using Analytical Size Exclusion Chromatography (SEC)

Class II chaperones of the type three secretion system (TTSS) in gram negative bacteria *Yersinia, Shigella* and *Pseudomonas* species have been shown to be homodimeric in solution [166-168,195]. In Chapter 3 we obtained conditions where fl-LcrH, tr-LcrH and L65E tr-LcrH were ''stable'' (*i.e.* maintained a ''native'' oligomeric state). These experiments were carried out at high concentrations and gave elution profiles in analytical SEC of dimeric size for fl-LcrH and tr-LcrH but monomeric for L65E tr-LcrH. To qualitatively probe the monomer-dimer equilibrium of fl-LcrH and tr-LcrH, analytical

SEC was performed over a range of protein concentrations. LcrH is a non-globular protein with each monomeric unit comprising of 3.5 modular tetratricopeptide repeats (TPRs). Thus, two non-globular protein standards – CTPR3 (3.5 continuously arrayed TPR motifs) and CTPRa6 (6.5 continuously arrayed TPR motifs) were chosen as protein standards for comparing the molecular sizes. The crystal structure of SycD (99% identical to LcrH) shows that the dimeric form of the protein produces a ''head-to-head'' dimer. Thus, dimeric LcrH should have a similar size to that of CTPRa6. Whereas the monomeric LcrH (L65E tr-LcrH) should elute with size similar to that of CTPR3 (Figure 4.1).

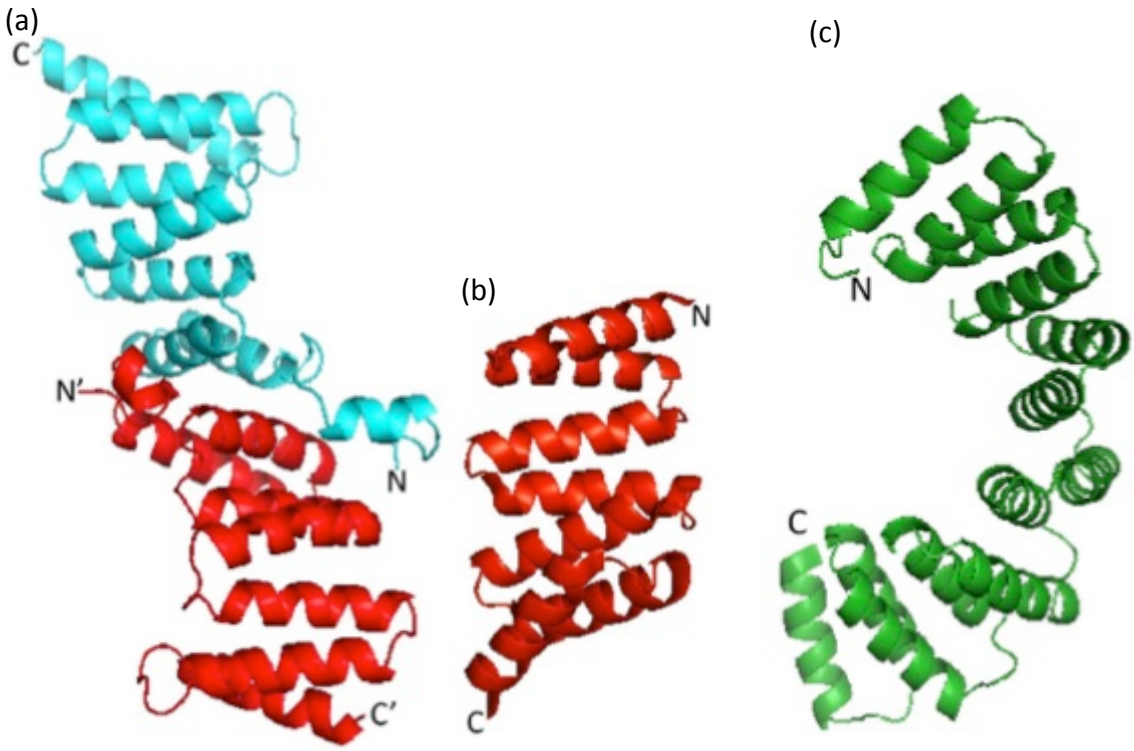

Figure 4.1 Ribbon representation of the crystal structures of (a) head-to-head confirmation of dimeric $SycD_{21-163}$ [Protein Data Bank (PDB) entry: 2VGX], chains A and B are shown in cyan and red respectively, (b) CTPR3 (PDB entry: 1NA0), (c) CTPRa6. The figure was prepared using PYMOL.

Figure 4.2 (a) and Figure 4.2 (b) show the analytical SEC profile for fl-LcrH and tr-LcrH from 3 – 100 µM respectively. These show that at higher concentrations (100 µM), fl-LcrH and tr-LcrH eluted with volumes of 9.7 ml and 9.6 ml respectively, and were consistent with a homodimeric structure (in close agreement with an elution peak of 9.6 ml for the designed TPR protein CTPRa6 containing 6.5 stacked repeats).

Interestingly, when the protein concentrations were lowered to more physiological concentrations i.e. from 100 µM to 3 µM, the elution volumes for fl-LcrH and tr-LcrH were observed to shift to that of a monomeric sized protein. The lowest concentration of 3 µM for tr-LcrH eluted at 10.7 ml, which was identical to the elution volume of 10.7

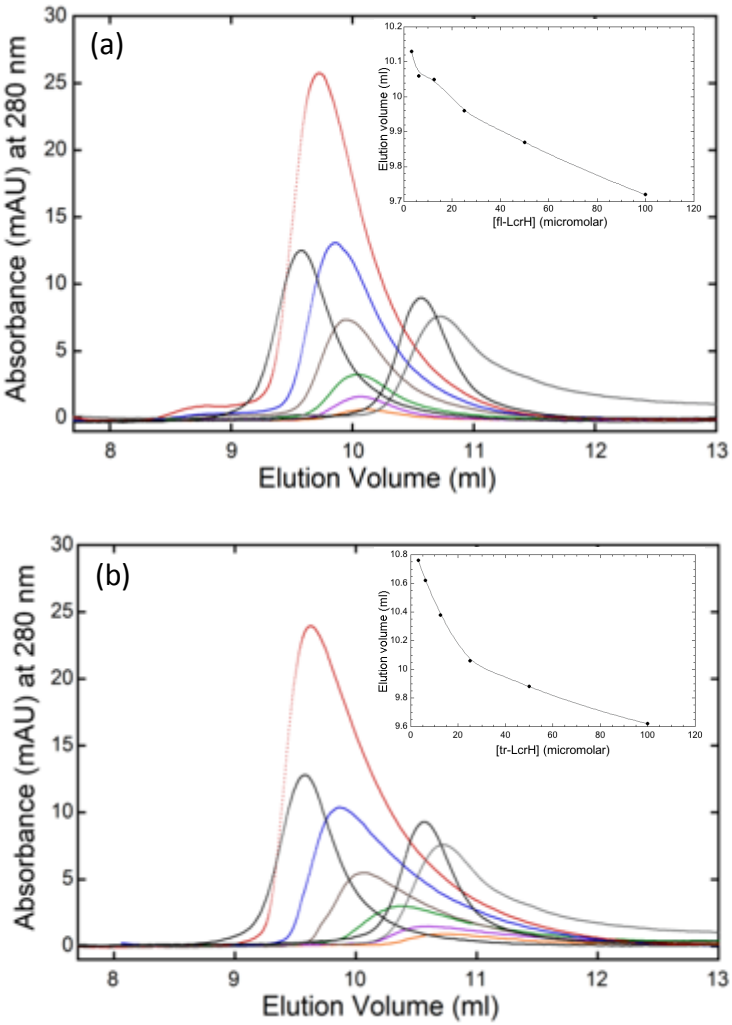

ml for monomeric L65E tr-LcrH and similar to elution volume of 10.55 ml for CTPR3 protein (containing 3.5 stacked repeats).

Figure 4.2 Analytical size exclusion chromatography profile of fl-LcrH (a) and tr-LcrH (b) using Superdex 75 HR 10/30 column at protein concentrations of 100 µM (red), 50 µM (blue), 25 µM (brown), 12 µM (green), 6 µM (purple) and 3 µM (orange). For calibration, two protein standards – CTPRa6 and CTPR3 were also run. CTPRa6 is a designed TPR protein that contains 6.5 continuously arrayed TPR motifs. CTPR3 is also a designed TPR protein that contains 3.5 continuously arrayed TPR motifs. Both the protein standards are coloured black; with cTPRa6 having elution volume of 9.6 ml and cTPR3 shows an elution volume of 10.55 ml. Monomeric L65E tr-LcrH is shown in grey and has an elution volume of 10.7 ml. In the respective inset figures, the elution volumes of LcrH proteins are plotted against their respective protein concentrations. Figure was prepared using KALEIDAGRAPH 4.0.

The change in elution profile shows that LcrH is present in monomer-dimer equilibrium at physiological protein concentrations and therefore has a relatively weak dimerisation interaction. It also suggests that its K_D value should be in the low micromolar range.

4.3.2 Determination of Dimerization Dissociation Constant (K_D) using Analytical Ultracentrifugation (AUC)

The previous section suggested that the dimerization dissociation constant (K_D) should be in the low micromolar (μM) concentration range for tr-LcrH and fl-LcrH. In order to

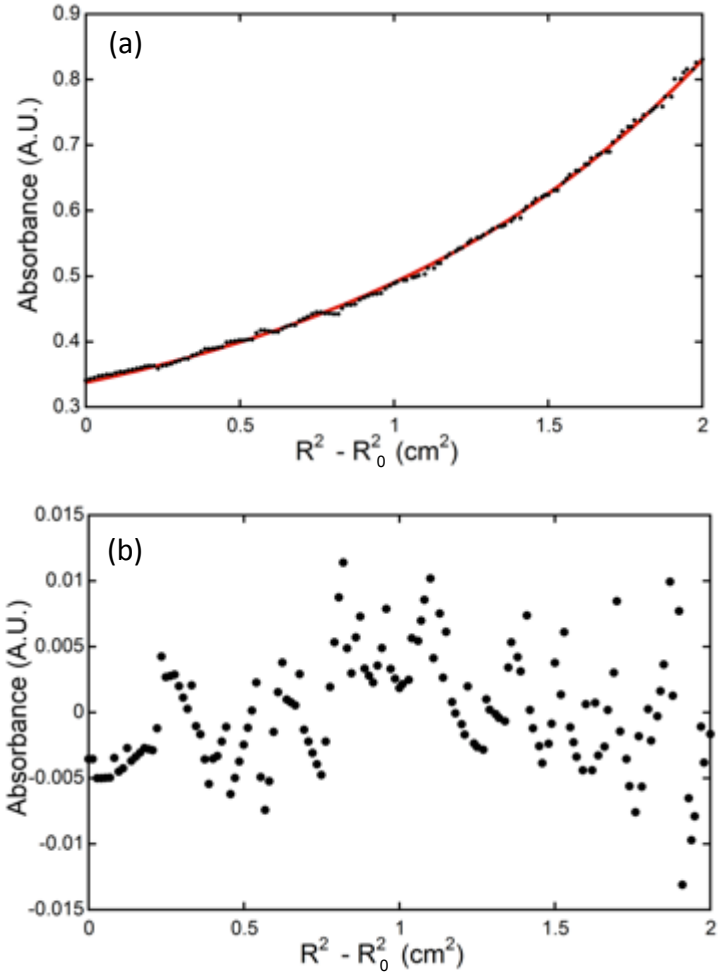

accurately determine the K_D value, equilibrium sedimentation by analytical ultracentrifugation for tr-LcrH was performed (section 2.3.2, Figure 4.3).

Figure 4.3 Equilibrium Analytical Ultracentrifugation (AUC) for tr-LcrH, the figure shows (a) the representative curve obtained from equilibrium sedimentation using analytical ultracentrifugation denoted by black dots and the line of best fit (red) to a monomer-dimer equilibrium model using the program Ultrascan, (b) fitted residuals shown by black filled circles.

From Figure 4.3 (b), it can be observed that the residuals from the fit appear to be scattered randomly and have an absorbance close to zero. This deemed the fit appropriate. No other trends can be observed in the residuals so does not need to be fitted to another model except the monomer-dimer equilibrium model (Equation 2.6). Multiple curves from the equilibrium sedimentation experiment were fitted and calculations were carried out using the Equation 2.6. This gave a dimerization dissociation constant K_D of 15 ± 5 μM. The errors and confidence limits were calculated as mentioned in section 2.3.2.

4.3.2.1 Calculating percentage of dimer at a given protein concentration

After determining the dimerization dissociation constant K_D for tr-LcrH, the percentage of the protein population that is dimeric can be calculated as follows:

The monomer-dimer chemical equilibrium at a given protein concentration can be illustrated by the Equation 4.1 below.

Equation 4.1

$$M + M \rightleftharpoons D$$

Where D is the dimer and M is the monomer. Thus, the dimerization dissociation constant K_D of this equilibrium is:

Equation 4.2

$$K_D = \frac{[M][M]}{[D]} = \frac{[M]^2}{[D]}$$

The total protein concentration (C_T) for the dimeric system can be written as:

Equation 4.3

$$[C_T] = [\mathrm{M}] + 2[\mathrm{D}]$$

Rearranging Equation 4.3 and solving for M gives

Equation 4.4

$$[M] = [C_T\,] - 2[D]$$

Substituting Equation 4.4 into the K_D expression (Equation 4.2) gives

Equation 4.5

$$K_D = \frac{(C_T - 2D)(C_T - 2D)}{D}$$

Solving the above Equation 4.5 into quadratic form gives:

Equation 4.6

$$[D] = \frac{4C_T + K_D \pm \sqrt{(8C_T * K_D + {K_D}^2)}}{8}$$

Fraction of dimeric species (F_D) at any given protein concentration can be defined by:

Equation 4.7

$$F_D = \frac{2[D]}{[C_T]}$$

'F_D' is the fraction of total 'D' (dimer), which can vary from 0 to 1 and 'C_T' is the total protein concentration.

Thus, by substituting Equation 4.6 in Equation 4.7 we obtain:

Equation 4.8

$$F_D = \frac{4C_T + K_D \pm \sqrt{(8C_T * K_D + {K_D}^2)}}{4[C_T]}$$

A saturation-binding curve of F_D (fraction of total dimer) vs C_T (total protein concentration) using Equation 4.8 with the dimerization dissociation constant K_D value of 15 µM was plotted (Figure 4.4).

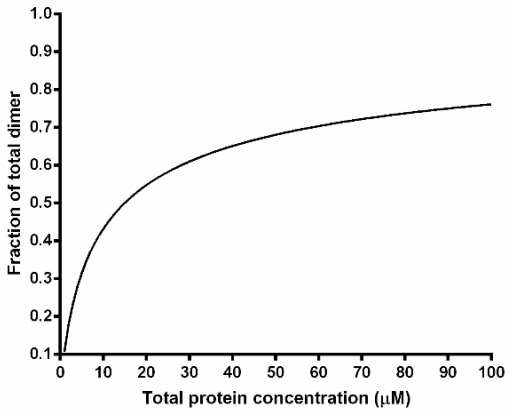

Figure 4.4 Saturation binding curve for dimerization of tr-LcrH showing a graph of *Y* vs C_T, where *Y* is the fraction of total possible dimer which varies between 0 to 1, C_T is the total protein concentration (μM) and the dimerization dissociation constant K_D = 15 ± 5 μM.

The curve in Figure 4.4 is hyperbolic with half-maximal dimer formation occurring at a total protein concentration of C_T = K_D. It can also be noted that even at a total protein concentration of 600 μM, which is 40-fold greater than K_D, only 90 % of the total possible dimer (D) is formed (F_D= 0.90). When C_T = 90 μM, 75 % of the protein is dimeric (Y = 0.75). The percentages of dimer at protein concentrations we will use later are shown in Table 4.1. The table shows that even at lower concentrations of tr-LcrH there is some dimer present.

Table 4.1: Dimer percentages at resepective protein concentrations of tr-LcrH

Total Protein Concentration (μM)	Percentage of Dimer (%)
1	11
3	23
6	34
12	46
25	58
50	68
80	74
100	76

The table shows percentages of dimer population of tr-LcrH at the given total protein concentrations (μM). The dimer percentages have been rounded up to the next highest number.

4.3.3 Loss of LcrH's α-Helical Structure on N-terminal Deletion and Concentration Reduction

As LcrH is a completely α-helical protein, far-UV CD provides an excellent probe for monitoring its secondary structure in solution. In the previous chapter we observed that under our conditions all LcrH constructs exhibit strong α-helical signals with indicative minima at 208 and 222 nm. Thus, to probe whether any structure is lost between fl-LcrH and tr-LcrH or transition from dimer to monomer, far-UV CD spectra were recorded for protein concentrations of 3 – 100 µM. The CD ellipticity at each concentration was converted to molar ellipticity (Equation 2.9) for ease of data comparison and to correct for path length and protein concentration (Figure 4.5).

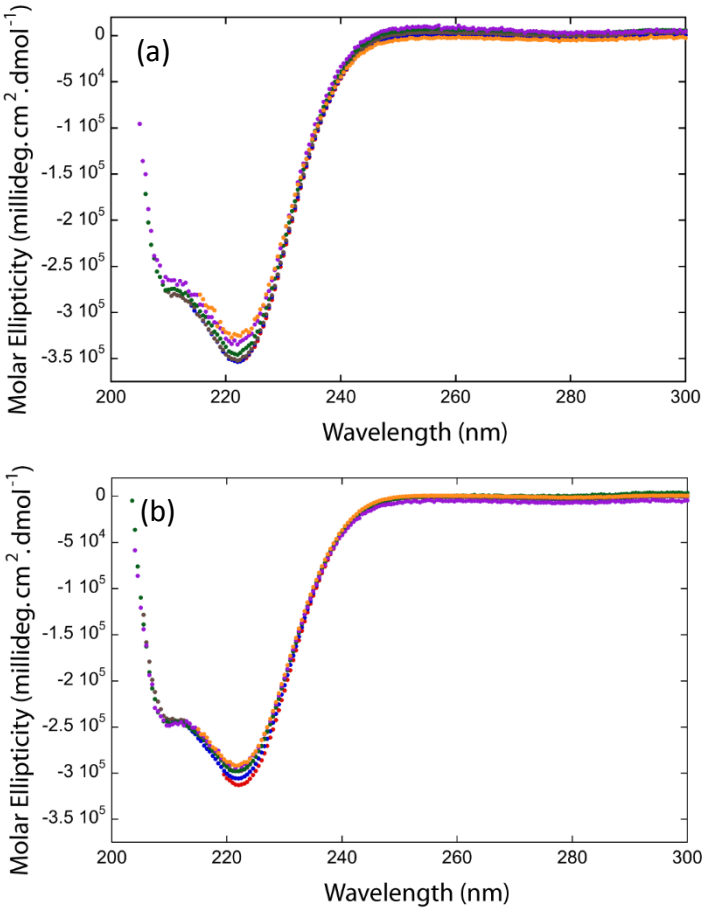

Figure 4.5 far-UV CD spectra showing molar ellipticity from 200 to 300 nm for native fl-LcrH (a) and tr-LcrH (b) at concentrations of 100 µM (red), 50 µM (blue), 25 µM (brown), 12 µM (green), 6µM (purple), and 3 µM (orange). Figure was prepared using KALEIDAGRAPH 4.0.

Interestingly, we observed a reduction in the signal (molar ellipticity at 222 nm) when tr-LcrH was compared with fl-LcrH and when the concentration of each protein was decreased. In each case the change was small as follows: at 50 µM, fl-LcrH and tr-LcrH

have molar ellipticities at 222 nm of -3.1 × 10^6 and -2.7 × 10^6 degrees cm^2 $dmol^{-1}$, respectively, and at 3.1 μM, fl-LcrH and tr-LcrH have molar ellipticities of -2.8 × 10^6 and -2.5 × 10^6 degrees cm^2 $dmol^{-1}$, respectively. In both comparisons this equates to a maximal change of ≈ 10 %. The reduction of α-helical signal from fl-LcrH to tr-LcrH suggested that the N-terminal 20 amino acid deletion of LcrH removes some α-helical structure. The loss of α-helical signal with a decrease in protein concentration is consistent with the weak monomer/dimer equilibrium i.e. the reduction in concentration of LcrH results in a monomeric state, which is less α-helically structured than the dimer.

4.3.4 Equilibrium Unfolding and Thermodynamic Stability of LcrH

To determine the flexibility and thermodynamic stability of fl-LcrH, tr-LcrH and L65E tr-LcrH equilibrium chemical denaturation experiments were performed (section 2.5.3). However, to achieve analysable denaturation experiments that were reproducible, we first needed to determine the following:

i. The best structural probe to monitor the chemical denaturation
ii. The most suitable chemical denaturant
iii. The minimum equilibration time that produced a proper equilibrium at every denaturant concentration
iv. The reversibility of equilibrium unfolding

4.3.4.1 The Best Structural Probe to Monitor Chemical Denaturation

In general, two highly used biophysical probes for protein structural change are far-UV circular dichroism (far-UV CD) and fluorescence. This is because both these techniques require small concentrations of protein sample, low sample volumes and exhibit high sensitivity. Far UV CD is an absorbance-based technique that monitors the secondary structure of a protein while fluorescence monitors the tertiary structural changes. LcrH should be amenable to both techniques, as firstly it has a high alpha-helical native structure thereby making it easy to gain information about the secondary structure and folded state of proteins using far UV CD. Secondly, fl-LcrH and tr-LcrH contain 8 and 7 tyrosine residues respectively. Hence, tyrosine fluorescence can be used as a

tertiary structure probe to monitor changes in LcrH's protein structure when subjected to unfolding.

To observe the change in signal of both these probes on LcrH's unfolding, each protein construct was incubated with 8 M urea. Figure 4.6 (a-c) shows the far-UV CD spectra of native and denatured LcrH proteins (fl-LcrH, tr-LcrH and L65E tr-LcrH) at 3 µM in 50 mM Phosphate, pH 7.0, 5 mM DTT. The native and 8 M urea denatured LcrH protein samples were incubated at 25 °C for 6 hours prior to recording far-UV CD spectra. The native protein samples showed strong α-helical signal with minima at 222 nm and 208 nm (minima at 208 nm not shown in figure). This is consistent with their high alpha helical native secondary structure. When a high molarity of chemical denaturant (8 M urea) was introduced these indicative minima disappeared, displaying that all native structure was unfolded. Importantly, the change in signal between folded and unfolded protein samples was suitably large.

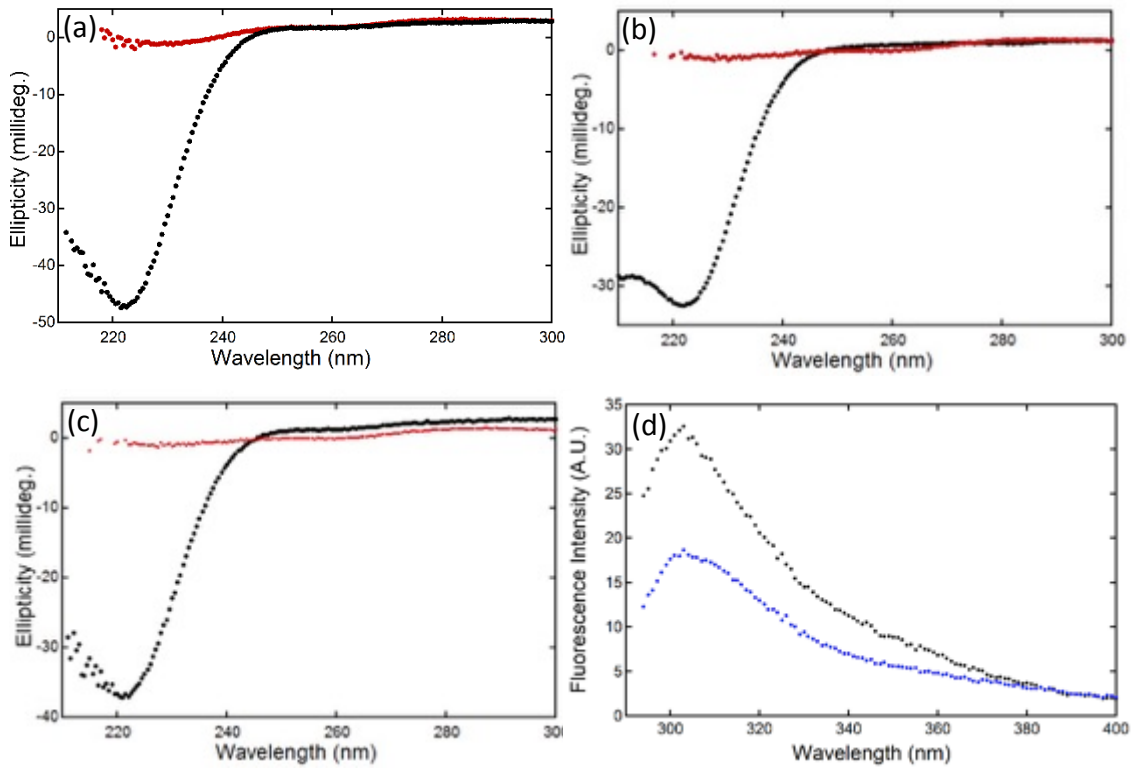

Figure 4.6 Far-UV CD spectra at 3 µM protein concentration of (a) fl-LcrH, (b) tr-LcrH, (c) L65E tr-LcrH showing native (black filled circles) and 8 M urea denatured (red filled circles). The CD spectra of the samples was taken using 5 mm path length quartz cuvette at 25 ± 0.2 °C. The data was masked for wavelengths below 212 nm as the CD detector became saturated with voltage exceeding 850 HT volts. (d) Tyrosine fluorescence of 3 µM tr-LcrH showing native (black) and 8 M urea denatured (blue). The excitation wavelength was 274 nm, the fluorescence spectra was measured from 294 nm to 400 nm in 1 cm pathlength quartz cuvette at 25 ± 5 °C. Figure was prepared using KALEIDAGRAPH 4.0.

After monitoring the secondary structure of LcrH proteins using far-UV CD, it was then decided to use fluorescence spectroscopy to compare the native and denatured tertiary structure of LcrH. Figure 4.6 (d) shows the comparison between the fluorescence intensities of native and 8 M urea denatured 3 µM tr-LcrH protein samples. Here, the sample was excited at 274 nm and emission spectrum from 294 nm to 400 nm was recorded. A peak due to tyrosine emission can be seen at 303 nm, which decreases on addition of urea. However, it is also obvious that the change in signal in fluorescence on unfolding was not as great a change as that observed for the far-UV CD. Figure 4.6 showed that the largest difference in the far-UV CD signal between the native and denatured LcrH samples was observed at 222 nm, which was then used to monitor equilibrium unfolding.

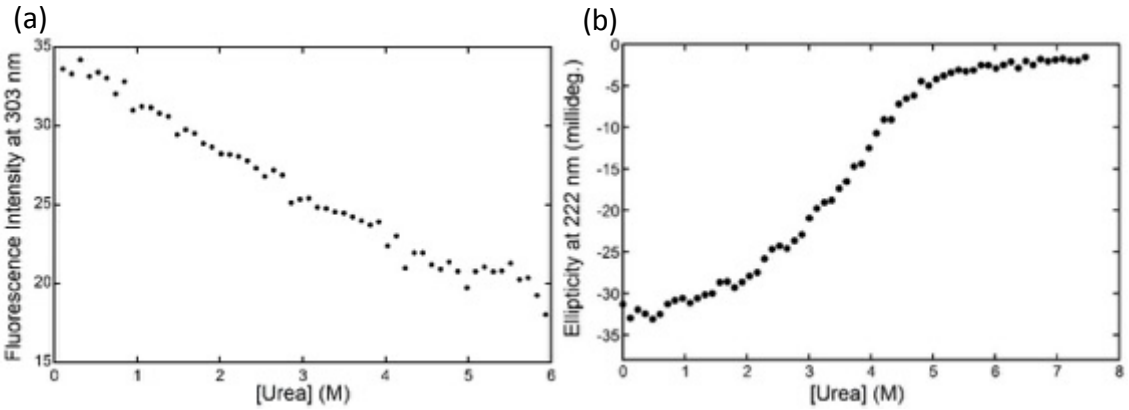

Figure 4.7: (a) Tyrosine fluorescence monitored at 303 nm (*black filled circles*) for urea induced equilibrium unfolding of 3 µM tr-LcrH. The excitation wavelength was 274 nm and slit width for excitation and emission was 5 nm. Fluorescence emission was recorded using 1 cm path length quartz cuvette at 25 ± 5 °C. (b) Equilibrium unfolding profile of 3 µM tr-LcrH monitored by far-UV CD at 222 nm wavelength. Measurements were taken using 0.5 cm path length quartz cuvette at 25 ± 5 °C in 50 mM Phosphate, pH 7.0 and 5 mM DTT. The samples were incubated at 25 °C for 6 hours prior to far-UV CD and fluorescence measurements. Figure was prepared using KALEIDAGRAPH 4.0.

Given that both probes showed a clear difference between native and denatured protein, it was decided to obtain a full equilibrium chemical denaturation. Here samples containing 3 µM tr-LcrH were prepared with a series of urea concentrations from 0 to 8 M urea (section 2.5.3.1). The samples were incubated for 6 hours at 25 °C

before taking far-UV CD and fluorescence measurements. The equilibrium unfolding profile of 3 µM tr-LcrH for each probe is shown in Figure 4.7. When the two profiles are compared, a number of striking differences become obvious. The tyrosine fluorescence monitored equilibrium unfolding showed that tr-LcrH possesses no sigmoidal co-operative transition. In contrast, although far-UV CD monitored equilibrium unfolding (Figure 4.6 (b)) also showed an initial gradual unfolding profile, there is a distinct sigmoidal transition between the initial (folded) and final (unfolded) states. The fluorescence monitored unfolding data did not bear any resemblance to the sigmoidal unfolding pattern observed in far-UV CD monitored unfolding data. One explanation of the differing curves can be suggested by the positioning of the tyrosine residues in tr-LcrH (Figure 4.8). The surface analysis of the tr-LcrH protein structure showed that 50 % of the tyrosine residues, which are located in the N-terminus of the protein were found to be solvent exposed in the native state of the protein. Consequently, as the protein undergoes unfolding, the remaining 50 % of tyrosine residues too become solvent exposed. However, resultant change in the fluorescence intensity between native and unfolded LcrH protein in comparison to the secondary structural change observed from far-UV CD data (Figure 4.6) was much lower. This is because fluorescence is based on the environment of fluorophores i.e. tryptophans and tyrosines that are solvent exposed fluoresce at a different wavelength compared to those in a non-solvent exposed environment (the hydrophobic core of the protein). In order to observe a difference in fluorescence between a native and unfolded protein, there must be an overall change in the interaction of the solvent exposed tyrosines and tryptophans with the solution. Tryptophan has stronger fluorescence and higher quantum yield in comparison to tyrosine. But, LcrH does not contain any tryptophan residues. Although, tyrosine is a weaker emitter than tryptophan, it may still contribute significantly to protein fluorescence if present in great numbers. tr-LcrH and fl-LcrH contain only 7 and 8 tyrosine residues respectively, which is not a large number. Furthermore, tyrosine is frequently quenched due to loss of proton on the aromatic hydroxyl group by undergoing ionization in the excited state or due to its interaction with the peptide chain.

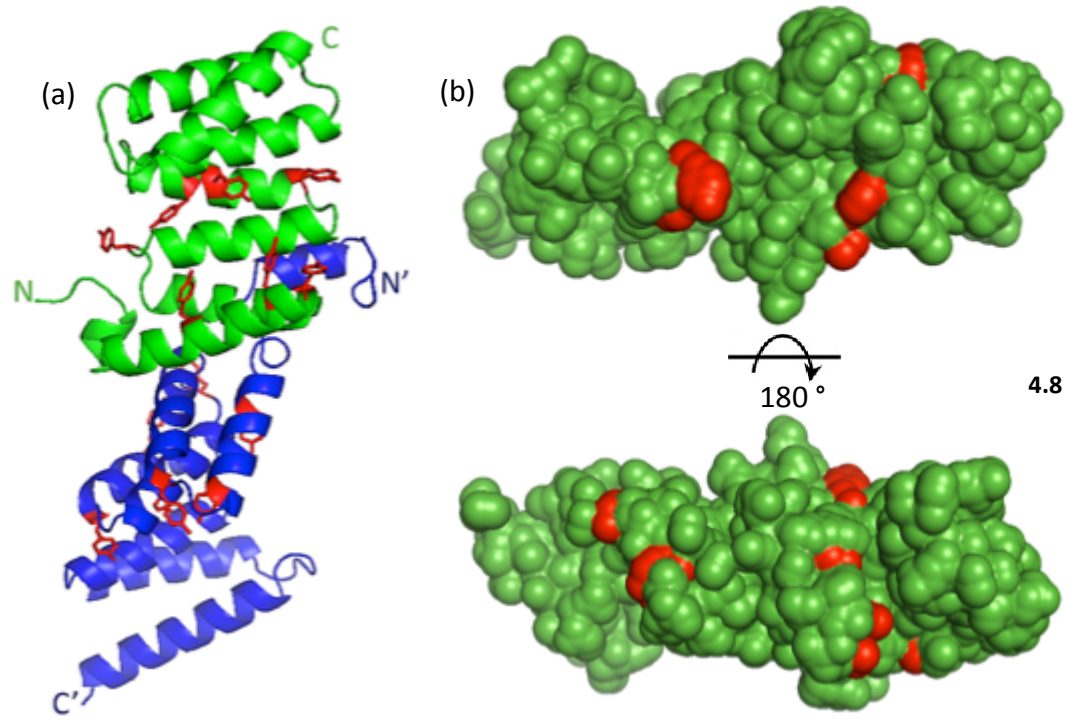

Figure 4.8 (a) Ribbon representation of dimeric tr-LcrH ($LcrH_{21-163}$) (PDB entry: 2VGX). Chains A and B are coloured green and blue respectively. There are 7 tyrosine residues in each chain, which are coloured in red and shown as sticks. (b) Solvent accessible surface representation of dimeric tr-LcrH (green) with tyrosine residues coloured red. The figures were prepared using PyMOL.

Thus, the equilibrium unfolding monitored by tyrosine fluorescence was not found to be suitable. Far-UV CD proved to be the best structural probe for monitoring the equilibrium unfolding of LcrH's protein constructs.

4.3.4.2 Determining the most suitable chemical denaturant

It was previously shown that LcrH underwent complete loss of secondary structure on denaturation with high molar concentration (8 M) of the chemical denaturant urea (Figure 4.6). When 6 M Guanidine hydrochloride (GdmHCl) was used to unfold 3- µM tr-LcrH, same result was achieved (Figure 4.9).

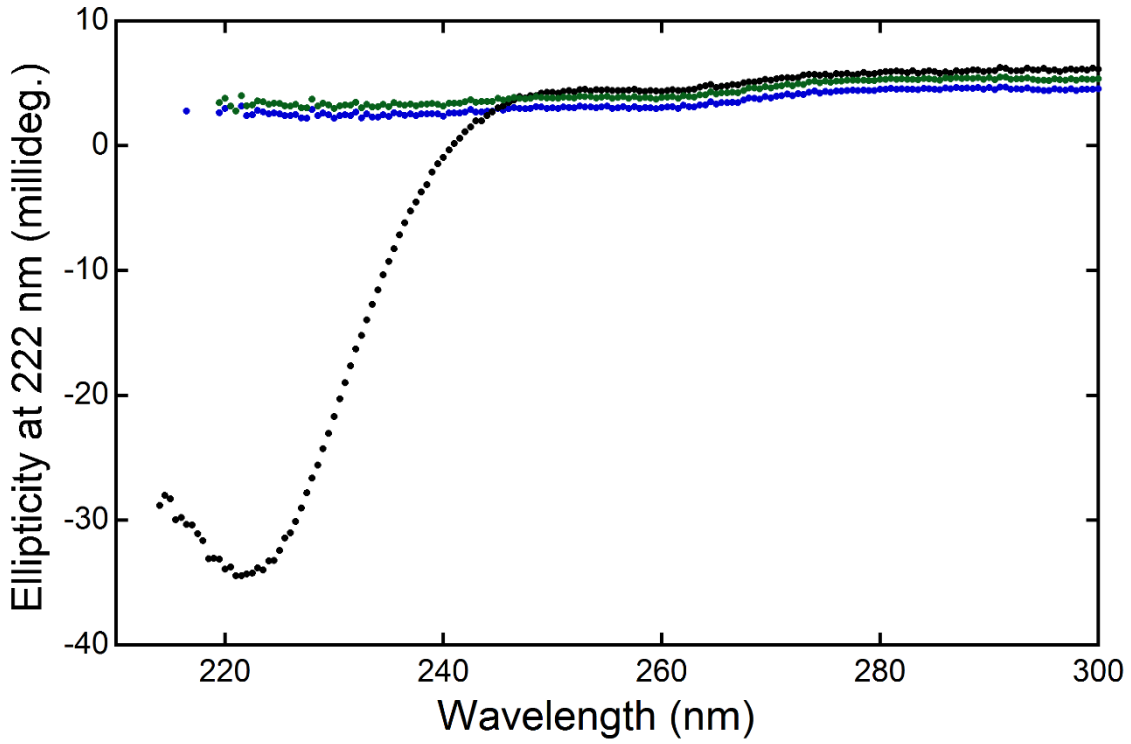

Figure 4.9 Far-UV CD spectra of 3 µM tr-LcrH showing native (black filled circles), 8 M urea denatured (blue) and 6 M GdmHCl denatured (green). The CD measurements were taken using 5 mm pathlength quartz cuvette at 25 ± 0.2 °C in 50 mM Phosphate, pH 7.0, 5mM DTT. Figure was prepared using KALEIDAGRAPH 4.0.

After observing the effect of GdmHCl, it was decided to perform an equilibrium chemical denaturation experiment using GdmHCl as a chemical denaturant and 3 µM tr-LcrH protein as the protein sample (Section 2.5.3). The samples were incubated at 25 ± 0.2°C for 6 hours followed by far-UV CD measurements. The GdmHCl induced equilibrium unfolding of tr-LcrH was compared to the urea induced equilibrium unfolding (Figure 4.10). GdmHCl is a stronger chemical denaturant than urea. Figure 4.10 shows that tr-LcrH undergoes unfolding at lower concentration of GdmHCl compared to that of urea. Importantly, the data comparison showed that there is a lack of folded (native) baseline for GdmHCl induced unfolding compared to that of urea. This lack of native baseline caused difficulties in fitting equilibrium unfolding curves to 2-state or multi-state denaturation models.

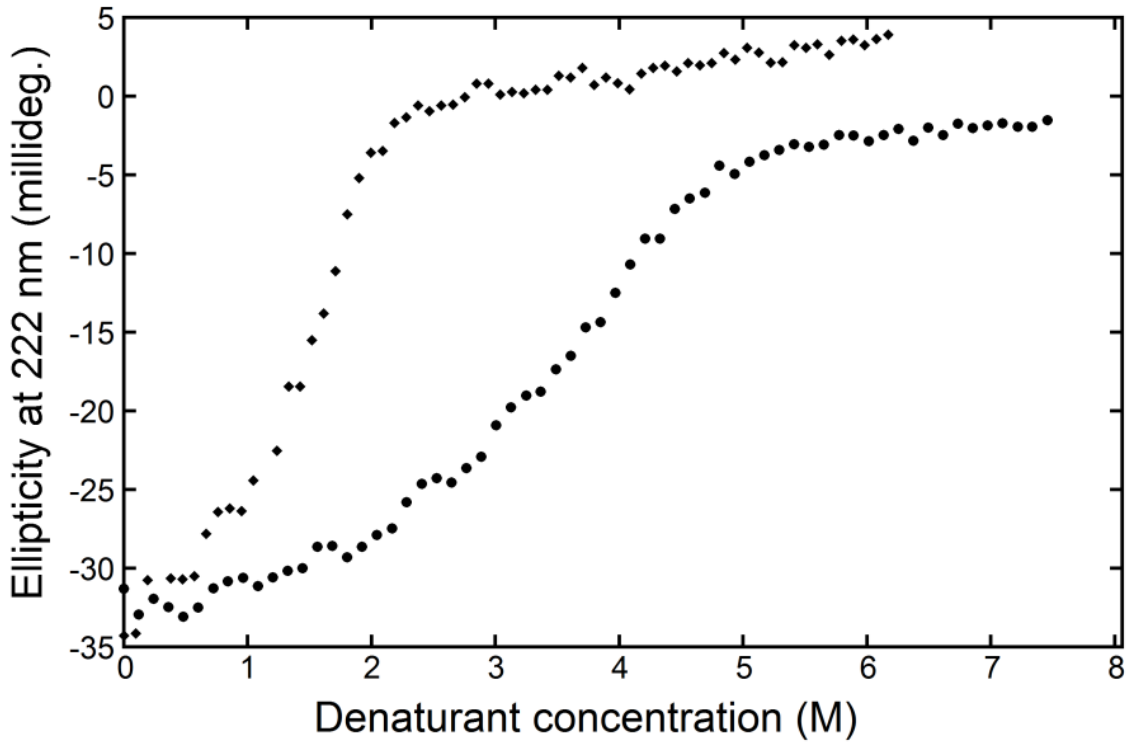

Figure 4.10 Equilibrium denaturation of 3 µM tr-LcrH using urea (black filled circles) and GdmHCl (black filled diamonds) monitored by changes in far-UV CD at 222 nm plotted against the denaturant concentrations (M) of urea and GdmHCl respectively. The samples were equilibrated for 6 hours prior to taking far-UV CD scans, in 5 mm path length quartz cuvette at 25 °C ± 0.2 °C, in 50 mM Phosphate pH 7.0, 5 mM DTT. Figure was prepared using KALEIDAGRAPH 4.0.

Therefore, it was decided that urea was the most suitable chemical denaturant. Henceforth, all the equilibrium-unfolding experiments of LcrH protein constructs were carried out using urea.

4.3.4.3 Minimum Equilibration Time for Equilibrium Chemical Denaturation

It is important to confirm that all protein samples at each denaturant concentration reach equilibrium. If insufficient time is allowed for equilibration, an incorrect stability and/or non-reproducible experiments may occur [195-197]. In order to determine the minimum equilibration time for LcrH, 3 µM tr-LcrH was chosen as a test case. A mixture of protein and urea in buffer were prepared (Section 2.5.3) and the samples were incubated for differing lengths of time (4, 12 and 24 hours). This was followed by taking far-UV CD measurements at 222 nm in a thermostatted cuvette holder at 25 ± 0.2 °C in a 5 mm path length quartz cuvette. Figure 4.11 shows the overlaid results.

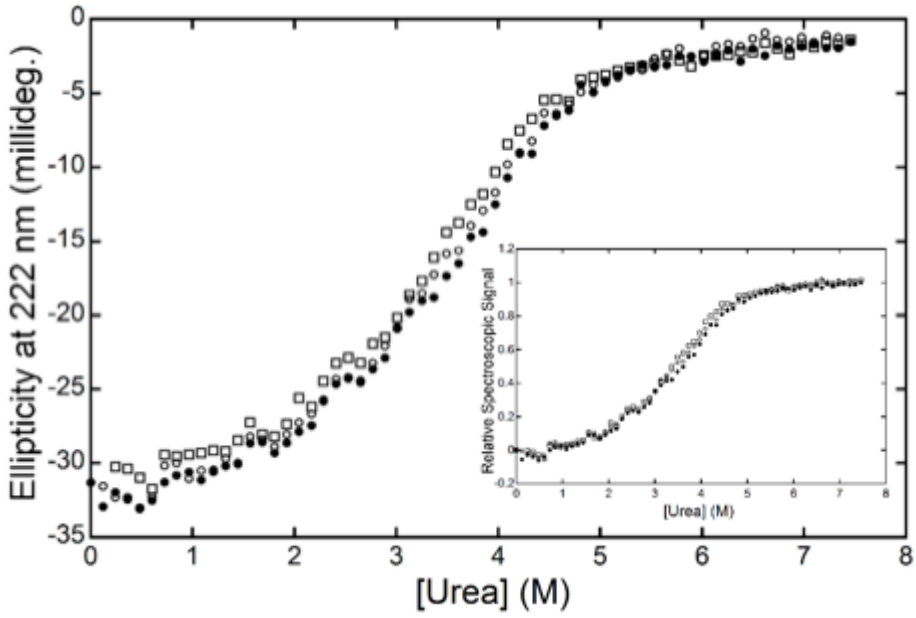

Figure 4.11 Urea induced equilibrium denaturation of tr-LcrH monitored by changes in far-UV CD signal (ellipticity in millidegrees) at 222 nm plotted against the concentration of urea (M). The superimposed equilibrium unfolding profiles of 3 µM tr-LcrH corresponds to differing equilibration times: 4 hours (filled circles), 12 hours (open circles) and 24 hours (closed squares) respectively. The inset figure shows the same unfolding profiles converted to relative spectroscopic signal (fraction unfolded) for easy comparison of different data sets. Figure was prepared using KALEIDAGRAPH 4.0.

Importantly, all three differing equilibration times were observed to be superimposable. It could thus be inferred that 4 hours was the minimum time required for achieving chemical equilibrium. Therefore, all equilibrium-unfolding experiments

were left for a minimum equilibration time of 4 hours prior to taking measurements on the CD spectrophotometer.

4.3.4.4 The Reversibility of Equilibrium Unfolding

The final control required was to confirm that the chemical denaturations were reversible. This is requirement, as otherwise thermodynamic parameters observed from fitting the curves will not report on the unfolding process, but instead on aggregation. For this experiment, tr-LcrH and fl-LcrH protein samples at 27 µM were unfolded with 8 M urea, equilibrated for 4 hours at 25 ± 0.2 °C respectively. The unfolded protein samples of both protein constructs were then refolded by aliquoting into buffer with differing concentrations of urea. This gave a final protein concentration of 3 µM in each differing urea concentration. The diluted/refolded samples were re-equilibrated for 4 hours followed by far-UV CD measurement at 222 nm. Figure 4.12 shows the far-UV CD monitored refolded equilibrium titrations superimposed onto the unfolded equilibrium titrations at 3 µM concentration of tr-LcrH and fl-LcrH respectively.

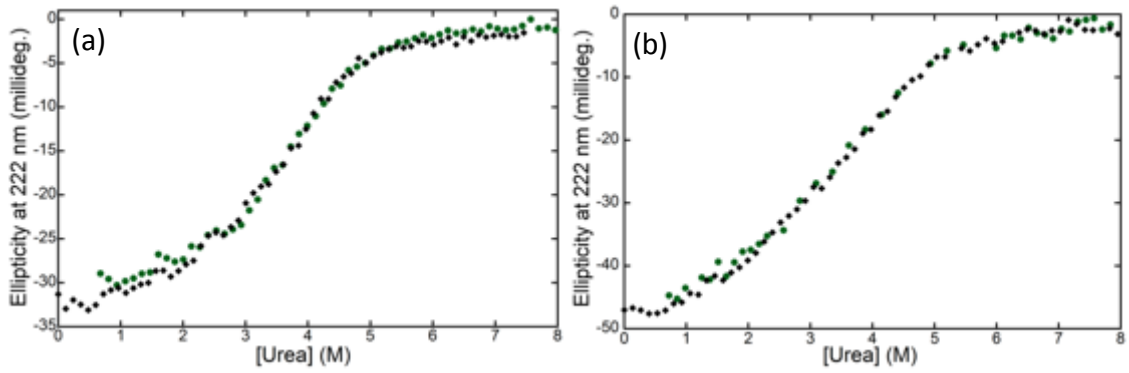

Figure 4.12 Reversibility of urea induced equilibrium unfolding of (a) tr-LcrH and (b) fl-LcrH at 3 µM protein concentration showing the unfolded titrations (black closed diamonds) and refolded titrations (green closed circles) respectively. The unfolding and refolding equilibrium titrations were monitored by changes in far-UV CD at 222 nm, in 5 mm path length quartz cuvette at 25 °C ± 0.2 °C, in 50 mM Phosphate, pH 7.0, 5 mM DTT. Figure was prepared using KALEIDAGRAPH 4.0.

The unfolded and subsequently refolded sampled retained nearly 100 % of their native far-UV CD signal. This confirmed that urea induced equilibrium unfolding of both tr-LcrH and fl-LcrH is completely reversible under the buffer conditions used.

4.3.5 Equilibrium Chemical Denaturation of LcrH's Protein Constructs

Having determined conditions where reversible, aggregation-free chemical denaturations of LcrH can be performed and monitored, we conducted such denturations at a number of different protein concentrations. For fl-LcrH, these were 3 and 50 µM (Figure 4.13), for tr-LcrH these ranged from 1 to 80 µM (Figure 4.14) and for monomeric L65E tr-LcrH these were 1.5 and 3 µM (Figure 4.15). Reproducibility of each denaturation was confirmed by repeating each experiment at least once (shown in the aforementioned figures). For both fl-LcrH and tr-LcrH the 50 and 80 µM chemical denaturations were the highest protein concentration that could be prepared. This was due to the methodology that chemical denaturations require, i.e. the protein stock solution is diluted to the same amount into a series of increasing urea concentrations.

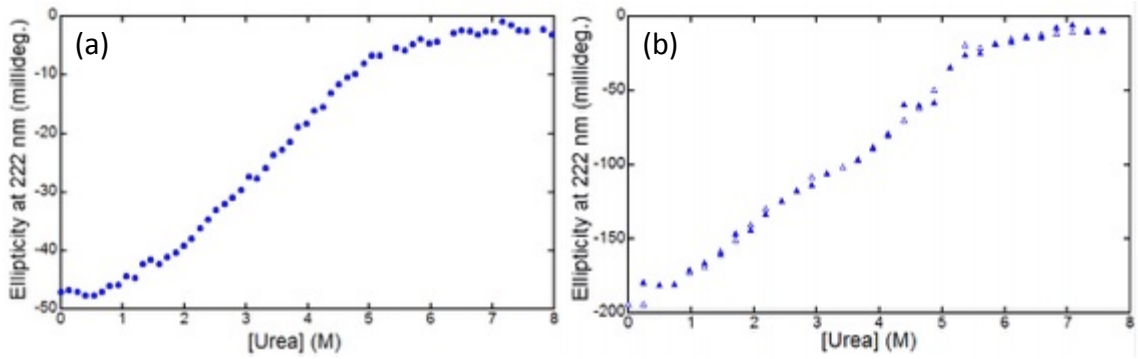

Figure 4.13 Urea induced equilibrium chemical denaturation of fl-LcrH at protein concentrations of (a) 3 µM shown by blue filled circles, far-UV CD measurements were taken using a 5 mm path length cuvette and (b) 50 µM shown by open and filled blue triangles for reproducibility, far-UV CD measurements were taken using a 1 mm path length cuvette. Figure was prepared using KALEIDAGRAPH 4.0.

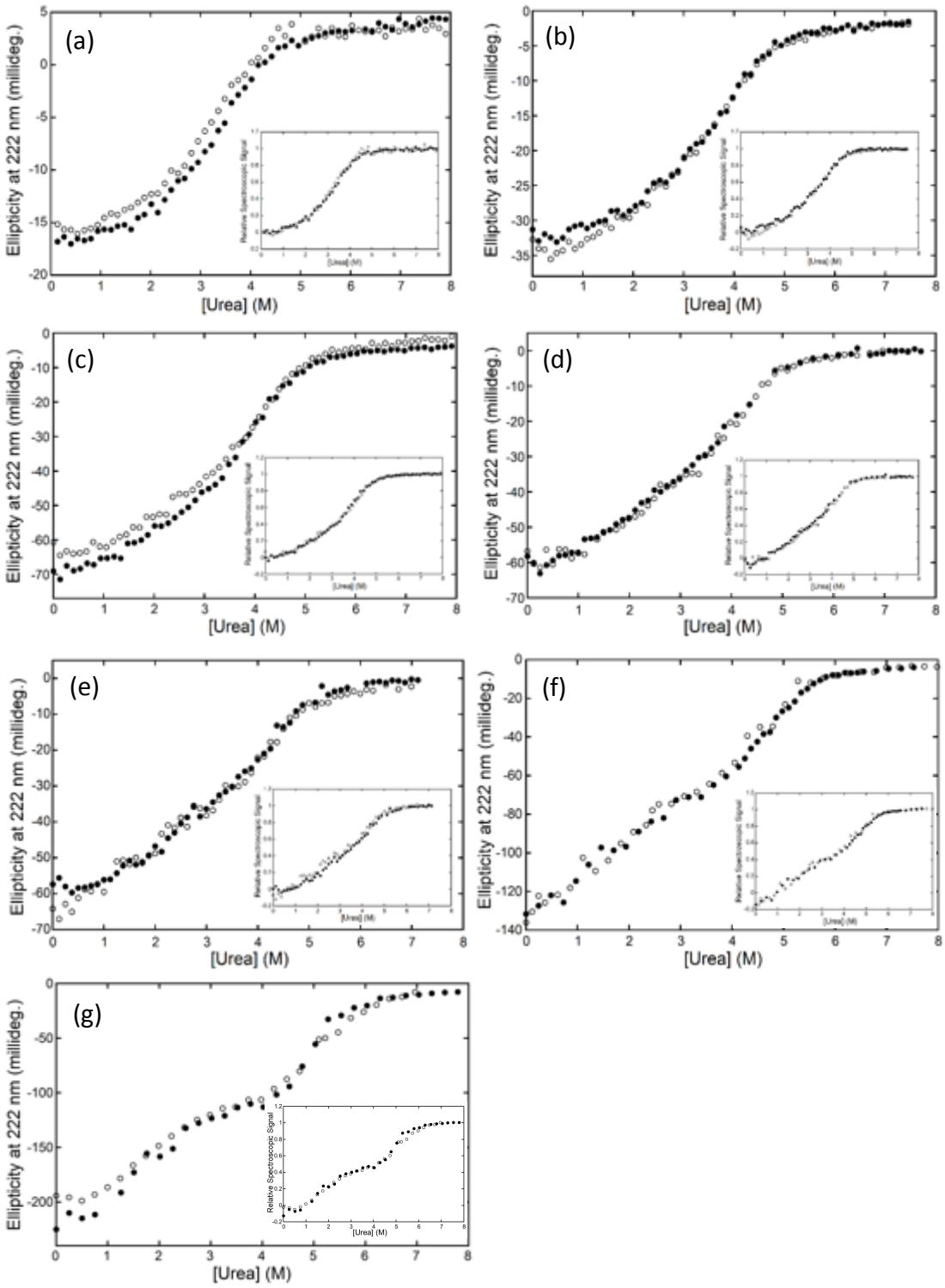

Figure 4.14 Urea induced unfolding of tr-LcrH monitored by change in far-UV CD at 222 nm at protein concentrations: (a) 1 µM (1 cm path length), (b) 3 µM (5 mm path length), (c) 6 µM (5 mm path length), (d) 12 µM (2 mm path length), (e) 25 µM (1 mm path length), (f) 50 µM (1 mm path length) and (g) 80 µM (1 mm path length). The inset figures are the denaturation profiles at respective concentrations with the CD signal changed to relative spectroscopic signal (fraction unfolded) for ease of comparison. Each experiment was repeated at least once to confirm reproducibility and shown by black open and filled circles. Figure was prepared using KALEIDAGRAPH 4.0.

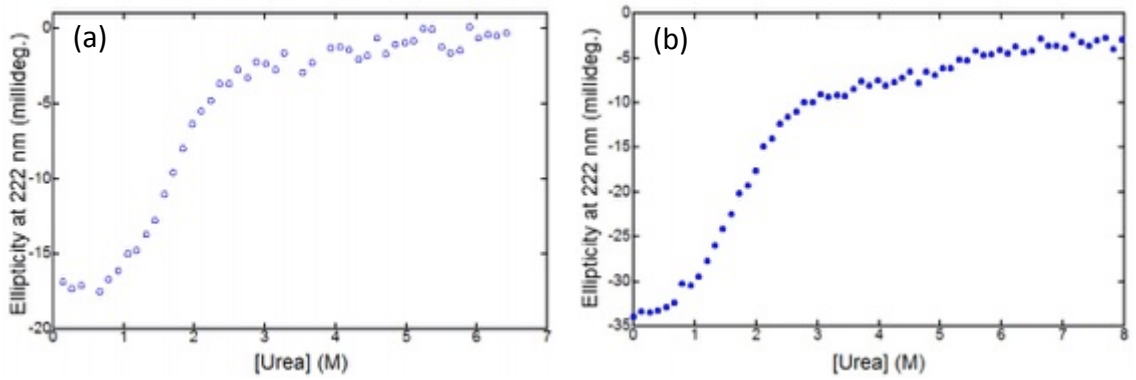

Figure 4.15 Urea induced equilibrium chemical denaturation of monomeric mutant L65E tr-LcrH at protein concentrations of (a) 1.5 µM shown by open blue circles and (b) 3 µM shown by closed blue circles. Far-UV CD measurements were taken using a 5 mm path length quartz cuvette at 25 ± 0.2°C. Figure was prepared using KALEIDAGRAPH 4.0.

For ease of comparison, each denaturation was converted from ellipticity at 222 nm vs urea to relative spectroscopy signal vs urea (Equation 2.9, Materials & Methods). Figure 4.16 shows fl-LcrH overlaid with tr-LcrH and the overlaid plots tr-LcrH from 1 µM to 80 µM, respectively. From these graphs the following features and trends were immediately apparent.

4.3.5.1 Biphasic Denaturations Show LcrH Unfolds via Partially Folded Dimeric Intermediate

The profile of each equilibrium denaturation and its protein concentration dependence delineates the mechanism by which oligomeric proteins unfold. Such concentration dependence is a unique characteristic of oligomeric protein systems and is a direct consequence of protein unfolding being coupled with oligomeric dissociation. Once determined, the data can be fit to the correct dimer denaturation model and thus obtain thermodynamic stability of the protein. Figure 4.16 shows that for both forms of LcrH the denaturation profile of each protein concentration consists of two transitions which becomes clearer with the increase in protein concentrations.

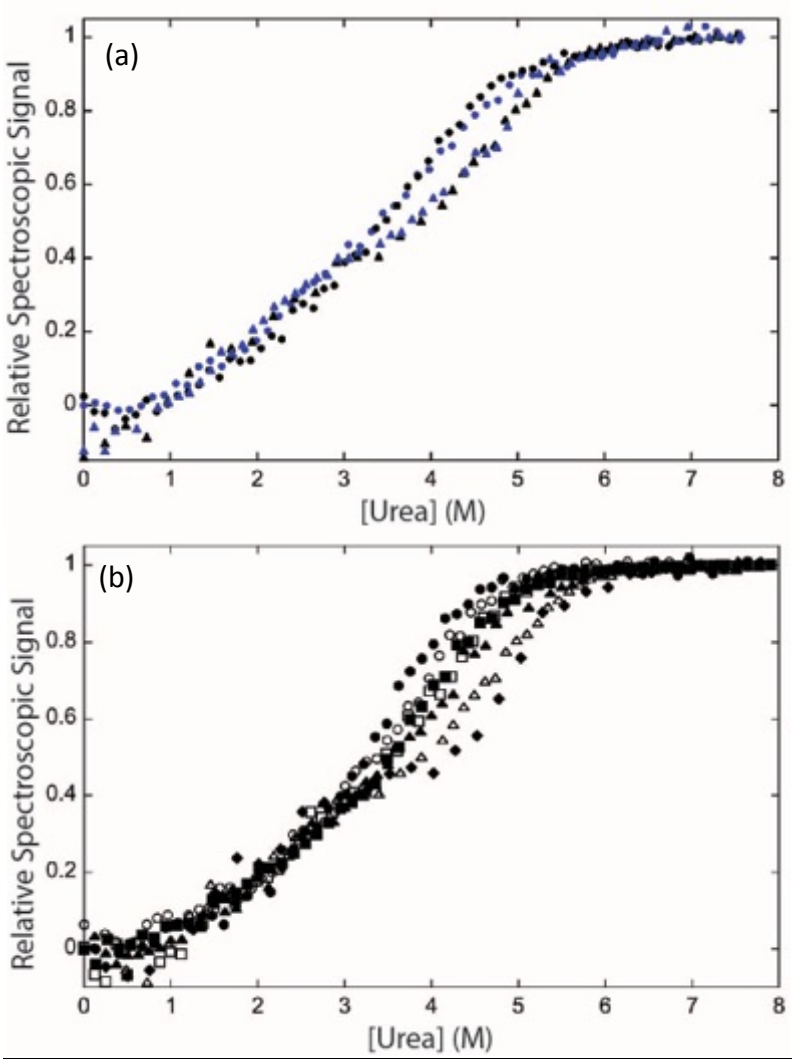

Figure 4.16 Urea denaturations monitored by changes in far-UV CD at 222 nm and converted to relative spectroscopic signal (see Equation 2.9) for (a) fl-LcrH and tr-LcrH. For clarity, only one denaturation is shown per concentration: 3 µM (fl-LcrH, blue-filled circles; tr-LcrH, black-filled circles) and 50 µM (fl-LcrH, blue-filled triangles; tr-LcrH, black-filled triangles). (b) tr-LcrH For ease of observation only one denaturation is shown per concentration – 1 µM (filled circles), 3 µM (open circles), 6 µM (filled squares), 12 µM (open squares), 25 µM (filled triangles), 50 µM (open triangle) and 80 µM (filled diamonds). Figure was prepared using KALEIDAGRAPH 4.0.

The initial unfolding produces a first sloping transition that accounts for the loss of approximately one third of the native α-helical signal. This ends at a saddle point at ≈ 3 M urea. At higher denaturant concentrations, a second sharper transition was observed. This results in the complete unfolding of the protein at urea concentrations of greater than 6 M. The biphasic unfolding pattern showed that a stable, partially structured intermediate is populated during the unfolding of LcrH. Significantly, the first transition is concentration-independent, and the second transition is

concentration-dependent (the midpoint '$[D]_{50\%}$' shifts to higher urea concentration with an increase in protein concentration). The observed pattern of unfolding (protein concentration-independent first transition to a stable partially folded intermediate followed by a protein concentration-dependent second transition) is consistent with a scheme where native dimer (N_2) partially unfolds to a dimeric intermediate (I_2), which then unfolds to a denatured monomer (2D), $N_2 \rightleftharpoons I_2 \rightleftharpoons 2\mathrm{D}$ (Figure 4.17). Moreover, it is important to note that the shallow nature of the first unfolding transition, native dimer to partially unfolded intermediate, shows a lack of co-operative unfolding. This indicates the structure of LcrH is particularly flexible and can easily adopt partially unfolded confirmations.

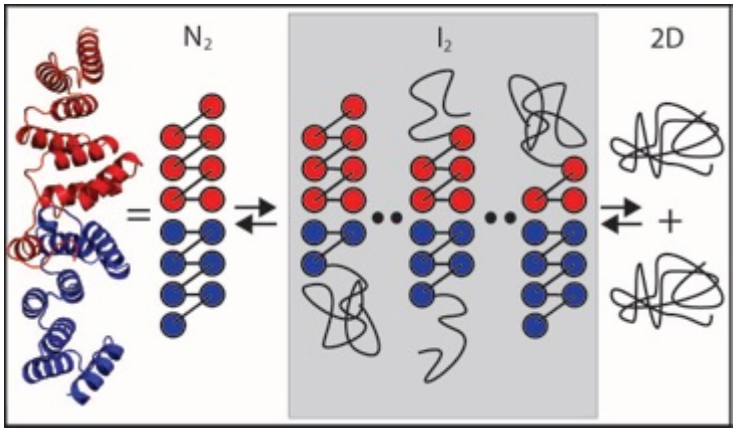

Figure 4.17 Schematic illustration of the proposed equilibrium unfolding pathway of LcrH. A head-to-head dimeric structure of SycD (PDB entry: 2VGX) is shown next to a topological map of the fold for reference (helices are shown as *circles* with the individual protein chains coloured *red* and *blue*). During unfolding, the native state (N_2) non-cooperatively frays through unfolding of C-terminal helices. This leaves an N-terminal dimeric intermediate (I_2). We note that various partially unfolded dimeric intermediate conformations could be populated during the unfolding transition. These are presented by showing the two extreme possible examples (one monomer of the dimer fully folded and the other mostly unfolding) and a third that is the median (both subunits partially unfolded to the same extent). These possible intermediate structures are shown in the *grey* box. At higher concentrations of urea the intermediate dissociates and denatures to a monomeric denatured state (2D, where D is the denatured state).

To confirm the dimeric intermediate unfolding mechanism, analytical SEC and dynamic light scattering of tr-LcrH at 50 µM were performed in urea concentrations of 0 – 6 M urea. Both methods showed that there was an increase in the size of tr-LcrH on increasing urea concentrations (Figure 4.18). In particular, the size of tr-LcrH was

similar from 0 to 2 M urea but then significantly increased in 3 M urea as observed from the analytical SEC profile of tr-LcrH (Figure 4.18 (b)). In order to investigate LcrH's increase in molecular size, the hydrodynamic radii at respective denaturant concentrations were plotted against the urea concentrations used for unfolding (Figure 4.18 (a) inset). It was revealed that tr-LcrH increased in size until 5 M urea and a reduction in hydrodynamic radius was observed in 6 M urea. It can be inferred that the first unfolding transition of LcrH involves partial unfolding to an expanded dimeric intermediate. By 6 M urea, tr-LcrH undergoes complete denaturation, with the shape of the peak by SEC becoming more symmetric. At, 0 M urea, tr-LcrH elutes at ~ 10.2 ml near the elution volume of 10.55 ml of the monomeric sized TPR standard CTPR3 which elutes at 10.55 ml (Figure 4.18 (b) and section 4.3.1). At 6 M urea, tr-LcrH elutes at ~ 8.6 ml in comparison to the dimeric TPR standard CTPRa6's elution volume of 9.6 ml (Figure 4.18 (b) and section 4.3.1). Thus, from the Figure 4.18 below, it can be seen that further unfolding of tr-LcrH produced an expanded monomeric species, which was greater in size than the dimeric TPR standard CTPRa6.

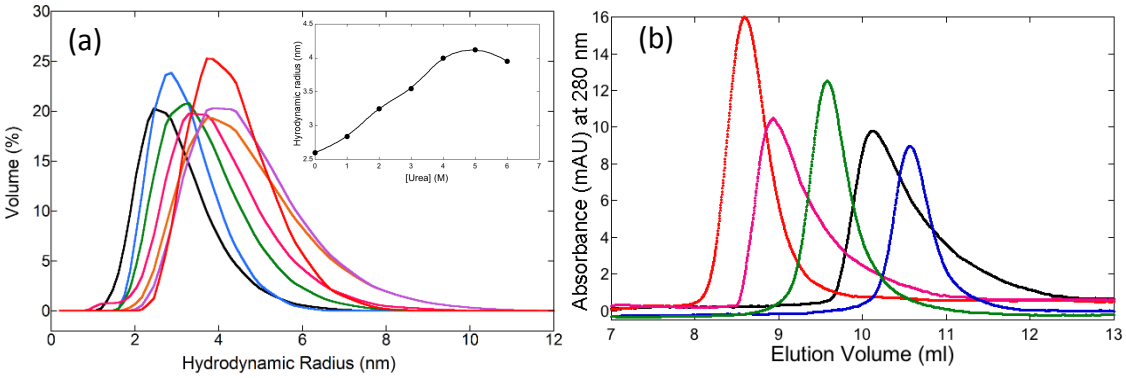

Figure 4.18 (a) Dynamic light scattering [volume of protein (%) against the hydrodynamic radius (nm)] of 50 µM tr-LcrH when in 0 M urea (black), 1 M urea (blue), 2 M urea (green), 3 M urea (pink), 4 M urea (orange), 5 M urea (purple), 6 M urea (red) and inset: Hydrodynamic radius (nm) against Urea concentration (M), smooth curve plotted in black. (b) Analytical SEC using S75 HR 10/30 column: 50 µM tr-LcrH in 0 M urea (black), 3 M urea (pink), 6 M urea (red), TPR standards - CTPR3 (blue) and CTPRa6 (green). Figure was prepared using KALEIDAGRAPH 4.0.

4.3.5.2 Deletion of N-terminus Causes No Change in Equilibrium Unfolding

When the equilibrium denaturations of fl-LcrH and tr-LcrH are compared at 3 and 50 µM, their profiles are indistinguishable (Figure 4.16). It is therefore clear that fl-LcrH and tr-LcrH have identical thermodynamic equilibrium unfolding and thus must infold via the same mechanism and have the same stability. This shows that although, the N-terminus of LcrH may possess some α-helical content, it does not alter the conformational stability or the nature of equilibrium unfolding of the protein.

4.3.6 Thermodynamic stability of LcrH

Having delineated the precise mechanism of LcrH's unfolding, the thermodynamic stabilities of the intermediate and native states were obtained by globally fitting the chemical denaturations performed at 50 and 80 µM for tr-LcrH and 50 µM for fl-LcrH to a three-state unfolding model with a dimeric intermediate (Figure 4.19). The derivation of the three-state unfolding model and Equations used to fit the data are described in detail in the following data analysis section. Lower protein concentration denaturations were excluded, as the intermediate state was not sufficiently populated to enable explicit fitting.

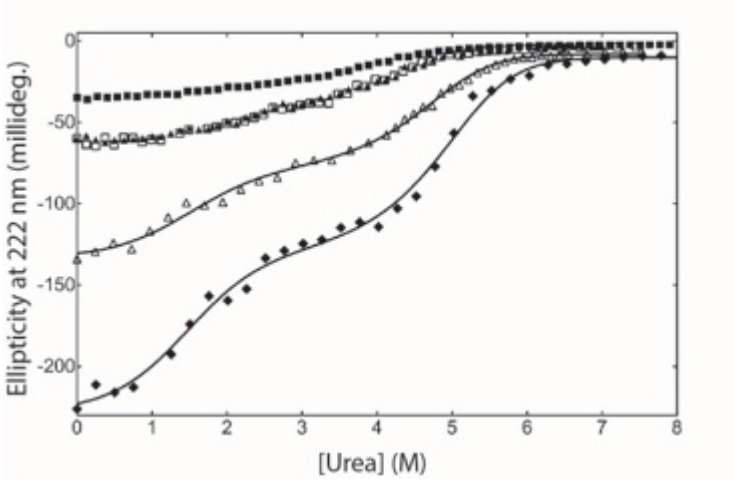

Figure 4.19 Urea denaturation of tr-LcrH monitored by changes in far-UV CD at 222 nm showing the global fit of the 50 and 80 µM data sets to a three-state model with a dimeric intermediate (Equation 4.4). For clarity, only one denaturation is shown per concentration: 6 µM (*filled squares*), 12 µM (*open squares*), 25 µM (*filled triangles*), 50 µM (*open triangle*) and 80 µM (*filled diamonds*). Figure was produced using GraphPad Prism 6.0.

4.3.6.1 Data analysis

In this study the unfolding of LcrH was fitted to a three-state model, which involves a dimeric intermediate (scheme 1)

$$N_2 \overset{K_1}{\rightleftharpoons} I_2 \overset{K_2}{\rightleftharpoons} 2\mathrm{D}$$ Scheme 1

where N_2 is the native dimer, I_2 is the intermediate dimer and D is the denatured state. In this model the equilibrium constants for the first (K_1) and second (K_2) transitions can be defined, respectively, as $K_1 = [I_2]/[N_2]$ and $K_2 = [D]^2/[I_2]$. The total protein concentration is $P_t = 2[N_2] + 2[I_2] + [D]$, and the sum of the fractions of individual species is equal to 1: $f_N + f_I + f_D = 1$, where f_I represents the fraction of monomeric subunits involved in the intermediate state. Combining these relationships gives:

Equation 4.9
$$K_1 = \frac{f_I}{f_N}$$

and

Equation 4.10
$$K_2 = \frac{2P_t f_D^2}{f_I}$$

Rearranging and substitution of the above Equations in terms of f_D (fraction of denatured protein) allows f_D to be expressed in terms of K_1, K_2 and P_t:

Equation 4.11
$$\boldsymbol{f_D} = \frac{-K_1K_2+\sqrt{(K_1K_2)^2+8(1+K_1)(K_1K_2)P_t}}{4P_t(1+K_1)}$$

In this model the spectroscopic signal obtained becomes:

Equation 4.12
$$\boldsymbol{\lambda_{obs} = \lambda_N f_N + \lambda_I f_I + \lambda_D f_D}$$

Where λ_{obs} is the spectroscopic signal, λ_N is the signal of the native state, λ_I is the signal of the intermediate state and λ_D is the signal of the native state. Substituting Equation 4.9 and Equation 4.10 into Equation 4.12 gives the final fitting Equation:

Equation 4.13 $$\boldsymbol{\lambda_{obs} = \lambda_N \frac{2P_t f_D^2}{K_1 K_2} + \lambda_I \frac{2P_t f_D^2}{K_2} + \lambda_D f_{\mathrm{D}}}$$

Global fitting to the three-state dimer denaturation model

To fit the denaturant dependent data and obtain ΔG values of each step in the unfolding, K_1 and K_2 can be defined according to the linear free energy model, which states that the free energy of each unfolding process varies linearly with the concentration of denaturant [196-198]:

Equation 4.14 $$\boldsymbol{\Delta G_x = -RT \ln K_x = \Delta G^x_{H_2O} - m[\text{denaturant}]}$$

Where ΔG_x is the free energy of the process x at a specific denaturant concentration, K_x is the equilibrium constant of the process x (in this case K_1 and K_2), ΔG^x_{H20} is the free energy of process x in the absence of denaturant and m is a constant that is proportional to the solvent exposure difference between the initial and end state of unfolding process x.

Equation 4.11, with f_D, K_1 and K_2 defined by Equation 4.9 and Equation 4.10 (respectively), was then used to globally fit the LcrH denaturations of differing concentrations using the non-linear, least-squares fitting programme *Prism*. This gave global thermodynamic parameters $\Delta G^1_{H_2O}$, $\Delta G^2_{H_2O}$ (stabilities of the first and second unfolding transitions, respectively) and m_1, m_2 (the m-values for the first and second unfolding transitions, respectively). λ_N, λ_I and λ_D (the spectral signals of the native, intermediate and denatured states respectively) were allowed to vary independently with each dataset. λ_I was assumed not to vary with denaturant concentration to minimize the number of parameters needed. Further, to reduce any baseline artifacts, the baselines (λ_N and λ_D) were constrained to zero slope. The thermodynamic

parameters obtained are presented in Table 4.2 and confirm the identical stabilities of fl-LcrH and tr-LcrH.

Table 4.2 Thermodynamic parameters for the global fitting of fl-LcrH & tr-LcrH at 25 °C using the three state dimer model with a dimeric intermediate

Global parameters

Protein	$\Delta G_{H_2O}^{N_2 \rightleftharpoons I_2}$ (kcal mol^{-1})	$m_{N_2 \rightleftharpoons I_2}$ (kcal mol^{-1} M^{-1})	$\Delta G_{H_2O}^{I_2 \rightleftharpoons 2D}$ (kcal mol^{-1})	$m_{I_2 \rightleftharpoons 2D}$ (kcal mol^{-1} M^{-1})	$^{a}\Delta G_{H_2O}^{N_2 \rightleftharpoons 2D}$ (kcal mol^{-1})
fl-LcrH	1.7 ± 0.5	1.0 ± 0.3	5.6 ± 1.8	1.7 ± 0.4	7.3 ± 1.9
tr-LcrH	1.7 ± 0.4	1.1 ± 0.2	5.7 ± 1.2	1.7 ± 0.2	7.4 ± 1.3

Individual parameters

Protein	[Total Protein] (μM)	$^{b}\lambda_N$ (millideg.)	$^{c}\lambda_I$ (millideg.)	$^{d}\lambda_D$ (millideg.)	Cuvette pathlength (cm)
fl-LcrH	50 * 1	-99 ± 5	54 ± 6	-5 ± 2	0.05
fl-LcrH	50 * 2	-95 ± 5	54 ± 6	-5 ± 2	0.05
tr-LcrH	50 * 1	-132 ± 5	-73 ± 6	-4 ± 2	0.1
tr-LcrH	50 * 2	-133 ± 5	-70 ± 6	-3 ± 2	0.1
tr-LcrH	80 * 1	-226 ± 8	-126 ± 9	-9 ± 3	0.1
tr-LcrH	80 * 2	-206 ± 7	-122 ± 8	-14 ± 4	0.1

Errors given are from the fit of all the data and are quoted at a 95 % confidence level (2 standard errors). $^{a}\Delta G_{H_2O}^{N_2 \rightleftharpoons 2D} = \Delta G_{H_2O}^{N_2 \rightleftharpoons I_2} + \Delta G_{H_2O}^{I_2 \rightleftharpoons 2D}$, with the error calculated by propagating the fitting errors. $^{b}\lambda_N$, $^{c}\lambda_I$ and $^{d}\lambda_D$ are the CD spectroscopic signals for native, intermediate and denatured LcrH, respectively, at 222 nm.

These show that the initial unfolding step ($N_2 \rightleftharpoons I_2$) has a $\Delta G_{H_2O}^{N_2 \rightleftharpoons I_2}$ of only 1.7 ± 0.4 kcal mol^{-1}. Thus, the majority of LcrH's stability resides in the dimerization structure ($I_2 \rightleftharpoons 2D$) as it requires an extra 5.7 ± 1.2 kcal mol^{-1} to unfold. This means the total stability of the protein ($\Delta G_{H_2O}^{N_2 \rightleftharpoons 2D}$) is 7.4 ± 1.3 kcal mol^{-1}. Interestingly, LcrH's stability ($\Delta G_{H_2O}^{N_2 \rightleftharpoons 2D}$) is less than many other dimeric proteins that have been shown to unfold via dimeric intermediate (Table 4.3). In particular, the first transition ($N_2 \rightleftharpoons I_2$) of LcrH was significantly lower than, for example, eAATase, Ure2p, SecA, OPH and AAO proteins. This confirms the non-cooperative and labile nature of LcrH's initial unfolding.

Table 4.3 Thermodynamic parameters characteristic of chemical induced unfolding of dimeric proteins by a three-state transition with dimeric intermediate

Protein	Temp. (°C)	$\Delta G_{H_2O}^{N_2 \rightleftharpoons I_2}$ (kcal mol^{-1})	$m_{N_2 \rightleftharpoons I_2}$ (kcal mol^{-1} M^{-1})	$\Delta G_{H_2O}^{I_2 \rightleftharpoons 2D}$ (kcal mol^{-1})	$m_{I_2 \rightleftharpoons 2D}$ (kcal mol^{-1}M^{-1})	[a]$\Delta G_{H_2O}^{N_2 \rightleftharpoons 2D}$ (kcal mol^{-1})
tr-LcrH	25	1.7	1.1	5.7	1.7	7.4
[b]eAATase	25	12.0	4.8	24.4	3.4	36.4
[c]SecA	20	8.4	4.1	14.1	1.5	22.5
[d]OPH	25	4.3	1.0	36.1	4.3	40.4
[e]AAO	10	3.5	1.7	13.6	1.2	17.1

[a]$\Delta G_{H_2O}^{N_2 \rightleftharpoons 2D} = \Delta G_{H_2O}^{N_2 \rightleftharpoons I_2} + \Delta G_{H_2O}^{I_2 \rightleftharpoons 2D}$. To give the best comparison with our data on LcrH the proteins chosen in this table were selected as the experimental conditions used to obtain them were similar to ours. i.e. urea as chemical denaturant, CD or fluorescence globally fitted, temperature between 10 – 25 °C and pH of between 7-8. The values quoted above are from the following studies: [b]eAATase -[198,199], [c]SecA -[199,200], [d]OPH -[200,201] and [e]AAO -[201-203].

An apparent K_D (K_D^{app}) for the dissociation of the intermediate to denatured monomer can also be calculated from the equilibrium data. As $\Delta G_{H_2O}^{I_2 \rightleftharpoons 2D}$ (from the seconds unfolding transition) is the free energy of unfolding and dissociation of the intermediate LcrH to denatured monomeric LcrH, it is related to the K_D^{app} by $\Delta G_{H_2O}^{I_2 \rightleftharpoons 2D} = -RT\ln K_D^{app}$. Thus, K_D^{app} can be simply obtained by rearranging this Equation. However, two caveats need to be considered before delineating its true significance.

(i) K_D^{app} corresponds to both unfolding and dissociation of the intermediate state of LcrH. This is not exactly equivalent to the $K_D$value obtained from the SEC and AUC data, which correspond to the dissociation of folded dimeric LcrH to folded monomeric LcrH. (ii) the K_D^{app} obtained in different solution conditions (high urea concentration). Given these caveats, the K_D^{app} calculated was 65 ± 65 µM and is consistent with the K_D calculated from AUC data and inferred from SEC data.

4.3.6.2 Proposed equilibrium unfolding pathway:

The ability of LcrH to easily fray into partially folded structures is facilitated by its modular tetratricopeptide repeat (TPR) structure. Unlike globular proteins, TPR and other repeat containing proteins are formed from the stacking of modular secondary structure motifs [202-206]. This causes their native structures to be dominated and

stabilized by interactions from amino acid residues that are close in primary sequence, whereas globular proteins have many stabilizing interactions from amino acids that are distant in primary sequence. This arrangement can enable sections of repeat proteins to unravel without unfolding the complete structure. We have studied the folding of a number of designed TPR proteins and shown that when partial unfolding occurs the proteins tend to unravel from the less stable outer repeats first [168,204-206]. As the N-termini of LcrH form the dimeric interface (which our results show is the most thermodynamically stable part of the structure), the unraveling must occur mainly from the C-terminus. A schematic diagram of the equilibrium-unfolding pathway proposed by our results is shown in Figure 4.17.

4.3.6.3 Thermodynamic Stability of Monomeric vs Dimeric LcrH

To complete the stability studies conducted on LcrH, the stability and flexibility of the monomeric mutant L65E LcrH was investigated. *In vivo* studies have shown that when SycD is made monomeric through the L65E mutation, non-invasive bacteria are produced [168,207]. This suggests that the dimeric interface is important for function. When we produced L65E tr-LcrH, we also obtained a monomer (at 50 µM there is a single SEC elution peal of 10.7 ml, which is similar to an elution peak of 10.55 ml obtained for a monomeric designed TPR protein of similar dimensions (3.5 stacked TPRs, Figure 4.2). Furthermore at 25 °C, L65E has the same α-helicity by CD to dimeric tr-LcrH (Figure 4.20a). However, chemical denaturation of L65E shows that the mutant was substantially destabilised compared to dimeric tr-LcrH with a single sharp transition between native and denatured states and little native baseline (Figure 4.20b). This was confirmed, as fitting the data to a two-state model showed the midpoint of the transition ($[D]_{50\%}$) is only 1.6 ± 0.1 M urea, the m-value of the transition is 1.4 ± 0.1 kcal mol^{-1} M^{-1} and thus its stability ($\Delta G_{H_2O}^{\mathrm{N}\rightleftharpoons\mathrm{D}}$) is 2.1 ± 0.2 kcal mol^{-1} ($\Delta G_{H_2O}^{\mathrm{N}\rightleftharpoons\mathrm{D}} = m.[D]_{50\%}$).

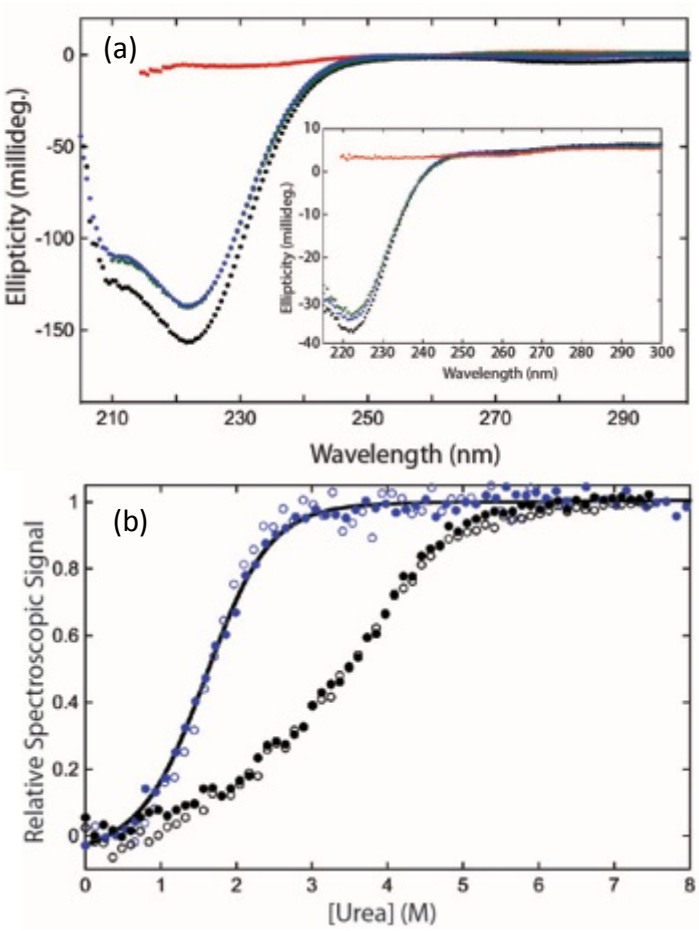

Figure 4.20 (a) Far-UV CD spectra comparing native fl-LcrH (*black*), tr-LcrH (*blue*), L65E tr-LcrH (*green*), and denatured L65E tr-LcrH in 8 M urea (*red*). A protein concentration of 50 µM in a 1-mm path length quartz cuvette was used in each experiment. The inset figure shows the same experiments conducted at a protein concentration of 3 µM in a 5-mm path length cuvette. Note that fl-LcrH has ~10% greater α-helical signal to tr-LcrH and L65E tr-LcrH at 222 nm. (b) Urea denaturation of L65E mutant of tr-LcrH (*open blue circles*, 1.5 µM, and *filled blue circles*, 3 µM) and tr-LcrH at 3 µM (*black open* and *filled circles* for comparison) monitored by changes in far-UV CD at 222 nm and converted to relative spectroscopic signal (see Equation 2.12). The best fit for L65E to a two state folding model is shown (*black*). Figure was prepared using KALEIDAGRAPH 4.0.

This stability is similar to the initial unfolding of the dimer tr-LcrH, but is substantially more cooperative and results in a complete loss of structure. Moreover, the low stability of L65E indicates that the *in vivo* results may well be caused by the destabilisation of LcrH to the extent that the monomers produced are unfolded and thus non-functional.

4.3.7 Conclusion

The results in this chapter show that LcrH is a weak dimer (K_D ~ 15 μM) that readily unfolds in a non-cooperative manner to a partially unravelled dimeric intermediate. In contrast, the monomeric mutant L65E tr-LcrH unfolds more cooperatively on chemical denaturation, resulting in a complete loss of structure. Thus, confirming the significance of the dimerization interface of LcrH for thermodynamic stability. Furthermore, the chapter shows that although deletion of the N terminus does remove some α-helical structure (10%), it does not affect either its stability or dimerization equilibrium. Excitingly, the energy barrier for the partial unravelling of dimeric LcrH is low (ΔG_{H2O} ~ 1.7 kcal mol^{-1} at 25 °C), suggesting that partially unfolded states of LcrH (held together at the dimeric interface) are present at physiological conditions. It is therefore proposed that such a loosely folded structure has biological relevance, at the very least, when binding its cognate protein partners (the far larger membrane inserting translocator proteins).

Chapter 5 Conclusions

The Black Death was one of the most devastating pandemics in the history of human kind. It resulted in the death of nearly 50 million people in Asia, Africa and Europe in the 14th century AD [7,207]. The pathogen responsible for this deadly infection was the bacterium *Yersinia pestis* which causes several forms of plague [7,208]. On infection by *Y. pestis*, the host's defences are overcome by a combination of stealth and active immune suppression targeting innate immune mechanisms. The type three secretion system (T3SS) of *Y. pestis* is crucial to the suppression arm of this strategy. This system injects a set of effector (virulent) proteins into the host cell cytoplasm when coming in contact with the bacteria compromising the host's immune system by affecting phagocytosis and cytokine production[208,209]. Thus, T3SS provides the key virulence factor in pathogens like *Y. pestis.* Furthermore, the T3SS is found in over two dozen infectious Gram-negative bacteria such as various strains of *E. coli* and *Pseudomonas aeruginosa*, a potent biofilm former with a strong connection to cystic fibrosis. Without T3SS, many pathogenic bacteria are unable to cause disease [209]. This makes the T3SS an attractive target for novel antimicrobial drugs.

Recently, the World Health Organisation (WHO) published a report on antibiotic resistance and highlighted that it is an imminent threat and needs to be immediately addressed [5,210]. According to the WHO, the true cost of antimicrobial resistance will be 300 million premature deaths and up to $100 trillion (£64 trillion) lost to the global economy by 2050. This will severely impact the world's GDP, which would be 0.5 % smaller by 2020 and 1.4 % smaller by 2030 [211]. Approximately 10 % of the microbes that would be linked to these deaths employ the T3SS making it an extremely attractive target for antimicrobial agents. In order to develop drugs more efficiently, a complete biochemical understanding of the T3SS, such as the formation of the infection machinery and the mechanism of infection are required.

To do this, I began studying the T3SS in *Y. pestis* and more specifically the class II chaperone LcrH to fully understand the conformational stability and biochemical behaviour of this protein. LcrH is critical for the formation of a fully functional T3SS and so too the infection process of mammalian cells by *Y. pestis*. Consequently, any

information regarding the biochemical characteristics of such a significant protein can provide a potential therapeutic drug target.

In order to gain insight into the protein's behaviour, the full length sequence encoding for the protein LcrH was cloned for protein production and purification. Despite being able to produce and purify LcrH to >95 % the protein proved extremely prone to aggregation. In order to overcome this problem, a construct was created with the N-terminal 20 amino acids and the last 5 amino acids removed (tr-LcrH). Here, the protein proved to be significantly less prone to aggregation. CD studies showed that the removal of the N-terminus of LcrH caused some loss in α-helical content but had no effect on the stability of the protein.

In order to determine the oligomeric state of both forms of LcrH and thus obtain a K_D value for dimersation, SEC and equilibrium sedimentations were performed. These showed that both full-length and truncated LcrH possess the same weak monomer-dimer equilibrium (low μM K_D), thermodynamic and conformational stability. Importantly, chemical denaturation revealed that both full length and truncated forms of LcrH unfolded in a 3-state transition, the states being (i) folded, (ii) partially folded dimeric intermediate and (iii) unfolded. This was initially surprising as most proteins in the TPR family, of which LcrH is one, unfold in a cooperative manner. Such non-cooperative behaviour must be due to the dimerisation interface. The dimer is created through interaction between the N-terminus thus the weakly folded intermediate transition must be caused by fraying at the C-terminus; as the C-terminus begins to unfold, the protein loses integrity before completely unfolding.

Next, a mutation was introduced that has been shown to disrupt the dimerisation interface and create a protein that was solely monomeric. This protein was termed LE65-tr-LcrH and was produced, purified and characterised using identical biochemical and biophysical methods as the dimer. This revealed that the mutant had the same α-helical content as dimeric tr-LcrH but, as expected, did not exist as a dimer. Furthermore, chemical denaturation studies revealed that the mutant was substantially destabilised compared to tr-LcrH with a single sharp transition between the native folded and the denatured states, a classic 2-state transition. Taken in

conjunction with the information gathered from the dimer, it is therefore evident that the dimer interface provides additional thermodynamic stability to the global structure. Consequently, some structures close to the interface (N-terminus) remains folded at equilibrium while other parts of the structure are unfolded (C-terminus).

Previous studies have illustrated the significance of the N-terminus in determining the arrangement of the subunits within the dimeric structure of class II chaperones. For example, $IpgC_{10-151}$ produces head to head dimers whereas full length IpgC forms a back to head dimer [169]. However, the results presented here clearly show that removal of the first 20 N-terminal amino acids have no effect on stability of LcrH and therefore it is unlikely that these residues are directly involved in subunit positioning within the dimer.

Within the T3SS in *Y. pestis*, LcrH interacts with the large membrane translocator proteins YopB and YopD. However, the mechanism by which these small chaperones find their cognate sequences within the large membrane proteins remains unclear. Excitingly, the results presented here support one possible mechanism, termed “fly-casting”. Here, the weakly folded C-terminal repeats of the chaperone adopt a partially folded conformation allowing it to more easily find the target peptide on the translocator protein. The chaperone then refolds and remains attached to the translocator, producing a more rigid structure. It is important that the integrity of the N-terminus is retained during this process as *in vivo* studies have shown that a monomeric LE65 LcrH homologue in SycD renders the bacteria non-invasive [168]. Such a scenario is not without precedent. For example, the three TPR motif-containing domain of PP5 has been shown to become more structured when bound to its cognate binding partner, the C terminus of Hsp90 [212]. Moreover, studies on the six ankyrin repeat protein IκBα show it also has a weakly folded C terminus. Here, repeats five and six fold upon binding to their cognate partner, the transcription factor NF-κB [198,213]. It has been shown that the function and lifetime within the cell of IκBα is critically linked to whether this region is structured via ligand binding or not [199]. This has yet to be explored for the translocator chaperones.

In summary, this result shows that the chaperone LcrH has a very flexible and weakly folded C-terminus and forms a dimer that is held together by the dimerisation interface at the N-terminus. We propose that such a flexible structure has biological relevance that is important in binding its cognate protein partners. These results should be generally applicable to all translocator chaperones, as they all contain the same TPR motif fold. Furthermore, both the interaction between the N-terminal dimerisation interface and the C-terminus with its cognate-binding partners are potential molecular targets as an alternative to broad-spectrum antibiotic therapy.

5.1 Future work

The future work in this area must surely focus on the protein-protein interaction between the chaperone LcrH and its cognate binding partner YopB or YopD. YopB and YopD are large transmembrane proteins. So, to characterise the interaction it would be the right step forward to create a peptide of the binding domain.

To our advantage, crystallographic studies have been carried out characterising peptides binding to various domains of the cognate binding partners in *P. aeruginosa* and *Shigella flexneri* but the K_D values have been weak. Therefore, the design of peptides that bind more strongly is the next step. Indeed, the ability to disable binding of the translocator to the chaperone through competitive inhibition is a key area of research.

Such studies employing the T3SS from *Y. pestis* as a model system will surely provide an excellent molecular understanding that could lead to molecularly targeted treatment. With so many potent pathogenic Gram-negative bacteria that employ the T3SS, the significance of this system cannot be ignored.

Chapter 6 Bibliography

1 Eckburg, P. B., Bik, E. M., Bernstein, C. N., Purdom, E., Dethlefsen, L., Sargent, M., Gill, S. R., Nelson, K. E. and Relman, D. A. (2005) Diversity of the human intestinal microbial flora. Science **308**, 1635–1638.

2 Berg, J. M., Tymoczko, J. L. and Stryer, L. (2002) Biochemistry, Fifth Edition: International Version, Granite Hill Publishers.

3 Hooper, L. V. and Gordon, J. I. (2001) Commensal host-bacterial relationships in the gut. Science **292**, 1115–1118.

4 Curtis, M. M. and Sperandio, V. (2011) A complex relationship: the interaction among symbiotic microbes, invading pathogens, and their mammalian host. Mucosal Immunol **4**, 133–138.

5 Snyderman, M. and Wiseman, C. (1996) Guide to Marine Life: Caribbean, Bahamas, Florida. Aqua Quest Publications, Inc. New York.

6 Bäckhed, F., Ley, R. E., Sonnenburg, J. L., Peterson, D. A. and Gordon, J. I. (2005) Host-bacterial mutualism in the human intestine. Science **307**, 1915–1920.

7 Perry, R. D. and Fetherston, J. D. (1997) Yersinia pestis--etiologic agent of plague. Clinical Microbiology Review. **10**, 35-66.

8 Traa, B. S., Walker, C., Munos, M. and Black, R. E. (2010) Antibiotics for the treatment of dysentery in children. International journal of epidemiology. **9**(Suppl 1): i70–74.

9 Hogan, C. M. Types of commensal relationships. Available from <www.eoearth.org/view/article/156381>. [14th July 2015].

10 Tlaskalová-Hogenová, H., Stepánková, R., Hudcovic, T., Tucková, L., Cukrowska, B., Lodinová-Zádníková, R., Kozáková, H., Rossmann, P., Bártová, J., Sokol, D., et al. (2004) Commensal bacteria (normal microflora), mucosal immunity and chronic inflammatory and autoimmune diseases. Immunol. Lett. **93**, 97–108.

11 Schramm, G. E., Johnson, J. A., Doherty, J. A., Micek, S. T. and Kollef, M. H. (2006) Methicillin-resistant Staphylococcus aureus sterile-site infection: The importance of appropriate initial antimicrobial treatment. Crit. Care Med. **34**, 2069–2074.

12 Purves, W. K., Orians, G. H., Sadava, D. and Heller, H. C. (2003) Life: The Science of Biology: Volume III: Plants and Animals 7 ed., Sinauer Associates and W. H. Freeman, Sunderland, USA.

13 Rahal, J. J. (2009) Antimicrobial resistance among and therapeutic options against gram-negative pathogens. Clin. Infect. Dis. **49 Suppl 1**, S4–S10.

14 Henderson, I. R., Navarro-Garcia, F., Desvaux, M., Fernandez, R. C. and Ala'Aldeen, D. (2004) Type V protein secretion pathway: the autotransporter story. Microbiol. Mol. Biol. Rev. **68**, 692–744.

15 Kudva, R., Denks, K., Kuhn, P., Vogt, A. and Müller, M. (2013) Protein translocation across the inner membrane of Gram-negative bacteria: the Sec and Tat dependent protein transport pathways. Research in microbiology. **164**, 505-534.

16 Greenfield, J. J. and High, S. (1999) The Sec61 complex is located in both the ER and the ER-Golgi intermediate compartment. J. Cell. Sci. **112 (Pt 10)**, 1477–1486.

17 Natale, P., Brüser, T. and Driessen, A. J. M. (2008) Sec- and Tat-mediated protein secretion across the bacterial cytoplasmic membrane--distinct translocases and mechanisms. Biochim. Biophys. Acta **1778**, 1735–1756.

18 Mao, C., Cheadle, C. E. and Hardy, S. (2013) Stoichiometry of SecYEG in the active translocase of Escherichia coli varies with precursor species. Proc. Natl. Acad. Sci. U.S.A. **110**, 11815-20.

19 Akopian, D., Dalal, K., Shen, K., Duong, F. and Shan, S.-O. (2013) SecYEG activates GTPases to drive the completion of cotranslational protein targeting. The Journal of cell biology. **200**, 397-405.

20 Walter, P. (1981) Translocation of proteins across the endoplasmic reticulum. I. Signal recognition protein (SRP) binds to in-vitro-assembled polysomes synthesizing secretory protein. The Journal of Cell Biology **91**, 545–550.

21 Cross, B. C. S., Sinning, I., Luirink, J. and High, S. (2009) Delivering proteins for export from the cytosol. Nat. Rev. Mol. Cell Biol. **10**, 255–264.

22 Valent, Q. A. (1998) The Escherichia coli SRP and SecB targeting pathways converge at the translocon. EMBO J. **17**, 2504–2512.

23 Angelini, S., Deitermann, S. and Koch, H.-G. (2005) FtsY, the bacterial signal-recognition particle receptor, interacts functionally and physically with the SecYEG translocon. EMBO Rep, EMBO Press **6**, 476–481.

24 Palmer, T. and Berks, B. C. (2012) The twin-arginine translocation (Tat) protein export pathway. Nat. Rev. Microbiol. **10**, 483–496.

25 Jongbloed, J. D., Martin, U., Antelmann, H., Hecker, M., Tjalsma, H., Venema, G., Bron, S., van Dijl, J. M. and Müller, J. (2000) TatC is a specificity determinant for protein secretion via the twin-arginine translocation pathway. J. Biol. Chem. **275**, 41350–41357.

26 Delepelaire, P. (2004) Type I secretion in gram-negative bacteria. Biochim. Biophys. Acta **1694**, 149–161.

27 Dawson, R. J. P. and Locher, K. P. (2006) Structure of a bacterial multidrug ABC transporter. Nature **443**, 180–185.

28 Murakami, S., Nakashima, R., Yamashita, E. and Yamaguchi, A. (2002) Crystal structure of bacterial multidrug efflux transporter AcrB. Nature **419**, 587–593.

29 Binet, R. and Wandersman, C. (1995) Protein secretion by hybrid bacterial ABC-transporters: specific functions of the membrane ATPase and the membrane fusion protein. EMBO J. **14**, 2298–2306.

30 Thanabalu, T., Koronakis, E., Hughes, C. and Koronakis, V. (1998) Substrate-induced assembly of a contiguous channel for protein export from E.coli: reversible bridging of an inner-membrane translocase to an outer membrane exit pore. EMBO J. **17**, 6487–6496.

31 Sharff, A., Fanutti, C., Shi, J., Calladine, C. and Luisi, B. (2001) The role of the TolC family in protein transport and multidrug efflux. From stereochemical certainty to mechanistic hypothesis. Eur. J. Biochem. **268**, 5011–5026.

32 Graham WV, Turner JR. Introduction to the host and bacterial pathogens-Homeland security: Epithelia as first line defenders. In Bacterial-Epithelial Cell Cross-Talk: Molecular Mechanisms in Pathogenesis. McCormick, BA (Ed.).

2006. Cambridge: Cambridge University Press.

33 Koronakis, V., Sharff, A., Koronakis, E., Luisi, B. and Hughes, C. (2000) Crystal structure of the bacterial membrane protein TolC central to multidrug efflux and protein export. Nature. **405**, 914-19.

34 Touzé, T., Eswaran, J. and Bokma, E. (2004) Interactions underlying assembly of the Escherichia coli AcrAB–TolC multidrug efflux system. Molecular Microbiology. **53**(2), 697-706.

35 Guzzo, J., Duong, F., Wandersman, C., Murgier, M. and Lazdunski, A. (1991) The secretion genes of Pseudomonas aeruginosa alkaline protease are functionally related to those of Erwinia chrysanthemi proteases and Escherichia coli alpha-haemolysin. Mol. Microbiol. **5**, 447–453.

36 Létoffé, S., Delepelaire, P. and Wandersman, C. (1991) Cloning and expression in Escherichia coli of the Serratia marcescens metalloprotease gene: secretion of the protease from E. coli in the presence of the Erwinia chrysanthemi protease secretion functions. J. Bacteriol. **173**, 2160–2166.

37 Duong, F., Lazdunski, A. and Murgier, M. (1996) Protein secretion by heterologous bacterial ABC-transporters: the C-terminus secretion signal of the secreted protein confers high recognition specificity. Mol. Microbiol. **21**, 459–470.

38 Filloux, A. (2004) The underlying mechanisms of type II protein secretion. Biochimica et Biophysica Acta (BBA)-Molecular Cell Research. **1694**, 163-179.

39 Sandkvist, M. (2001) Biology of type II secretion. Mol. Microbiol. 271–283.

40 Camberg, J. L. and Sandkvist, M. (2005) Molecular analysis of the Vibrio cholerae type II secretion ATPase EpsE. J. Bacteriol. **187**, 249–256.

41 Camberg, J. L., Johnson, T. L., Patrick, M., Abendroth, J., Hol, W. G. J. and Sandkvist, M. (2007) Synergistic stimulation of EpsE ATP hydrolysis by EpsL and acidic phospholipids. EMBO J. **26**, 19–27.

42 Sandkvist, M., Bagdasarian, M., Howard, S. P. and DiRita, V. J. (1995) Interaction between the autokinase EpsE and EpsL in the cytoplasmic membrane is required for extracellular secretion in Vibrio cholerae. EMBO J. **14**, 1664–1673.

43 Sandkvist, M., Hough, L. P., Bagdasarian, M. M. and Bagdasarian, M. (1999) Direct interaction of the EpsL and EpsM proteins of the general secretion apparatus in Vibrio cholerae. J. Bacteriol. **181**, 3129–3135.

44 Daefler, S., Guilvout, I., Hardie, K. R., Pugsley, A. P. and Russel, M. (1997) The C-terminal domain of the secretin PulD contains the binding site for its cognate chaperone, PulS, and confers PulS dependence on pIVf1 function. Mol. Microbiol. **24**, 465–475.

45 Shevchik, V. E. and Condemine, G. (1998) Functional characterization of the Erwinia chrysanthemi OutS protein, an element of a type II secretion system. Microbiology (Reading, Engl.) **144 (Pt 11)**, 3219–3228.

46 Nouwen, N., Ranson, N., Saibil, H., Wolpensinger, B., Engel, A., Ghazi, A. and Pugsley, A. P. (1999) Secretin PulD: association with pilot PulS, structure, and ion-conducting channel formation. Proc. Natl. Acad. Sci. U.S.A. **96**, 8173–8177.

47 Cornelis, G. R. (2006) The type III secretion injectisome. Nat. Rev. Microbiol. **4**, 811–825.

48 Mota, L. J. and Cornelis, G. R. (2005) The bacterial injection kit: type III

secretion systems. Ann. Med. **37**, 234–249.

49 Grant, S. R., Fisher, E. J., Chang, J. H. and Mole, B. M. (2006) Subterfuge and manipulation: type III effector proteins of phytopathogenic bacteria. Annu Rev Microbiol. **60**, 425-49.

50 Lindeberg, M., Biehl, B. S., Glasner, J. D., Perna, N. T., Collmer, A. and Collmer, C. W. (2009) Gene Ontology annotation highlights shared and divergent pathogenic strategies of type III effector proteins deployed by the plant pathogen Pseudomonas syringae pv tomato DC3000 and animal pathogenic Escherichia coli strains. BMC Microbiol. **9 Suppl 1**, S4.

51 Torto-Alalibo, T., Collmer, C. W. and Lindeberg, M. (2009) Common and contrasting themes in host cell-targeted effectors from bacterial, fungal, oomycete and nematode plant symbionts described using the Gene Ontology BMC **9 Suppl 1**, S3.

52 Christie, P. J. and Cascales, E. (2005) Structural and dynamic properties of bacterial type IV secretion systems (review). Mol. Membr. Biol. **22**, 51–61.

53 Walldén, K., Williams, R., Yan, J., Lian, P. W., Wang, L., Thalassinos, K., Orlova, E. V. and Waksman, G. (2012) Structure of the VirB4 ATPase, alone and bound to the core complex of a type IV secretion system. Proc. Natl. Acad. Sci. U.S.A. **109**, 11348–11353.

54 Fronzes, R., Christie, P. J. and Waksman, G. (2009) The structural biology of type IV secretion systems. Nat. Rev. Microbiol. **7**, 703–714.

55 Costa, T. R. D., Felisberto-Rodrigues, C., Meir, A., Prevost, M. S., Redzej, A., Trokter, M. and Waksman, G. (2015) Secretion systems in Gram-negative bacteria: structural and mechanistic insights. Nat. Rev. Microbiol. **13**, 343–359.

56 Chagnot, C., Zorgani, M. A., Astruc, T. and Desvaux, M. (2013) Proteinaceous determinants of surface colonization in bacteria: bacterial adhesion and biofilm formation from a protein secretion perspective. Front Microbiol **4**, 303.

57 Jacob-Dubuisson, F., Fernandez, R. and Coutte, L. (2004) Protein secretion through autotransporter and two-partner pathways. Biochim. Biophys. Acta **1694**, 235–257.

58 Dautin, N. and Bernstein, H. D. (2007) Protein secretion in gram-negative bacteria via the autotransporter pathway. Annu. Rev. Microbiol. **61**, 89–112.

59 Bernstein, H. D. (2007) Are bacterial “autotransporters” really transporters? Trends in Microbiology, Elsevier **15**, 441–447.

60 Leininger, E., Roberts, M., Kenimer, J. G., Charles, I. G., Fairweather, N., Novotny, P. and Brennan, M. J. (1991) Pertactin, an Arg-Gly-Asp-containing Bordetella pertussis surface protein that promotes adherence of mammalian cells. Proc. Natl. Acad. Sci. U.S.A. **88**, 345–349.

61 Hoiczyk, E., Roggenkamp, A., Reichenbecher, M., Lupas, A. and Heesemann, J. (2000) Structure and sequence analysis of Yersinia YadA and Moraxella UspAs reveal a novel class of adhesins. EMBO J. **19**, 5989–5999.

62 Pukatzki, S., Ma, A. T., Sturtevant, D., Krastins, B., Sarracino, D., Nelson, W. C., Heidelberg, J. F. and Mekalanos, J. J. (2006) Identification of a conserved bacterial protein secretion system in Vibrio cholerae using the Dictyostelium host model system. Proc. Natl. Acad. Sci. U.S.A. **103**, 1528–1533.

63 Mougous, J. D., Cuff, M. E., Raunser, S., Shen, A., Zhou, M., Gifford, C. A., Goodman, A. L., Joachimiak, G., Ordoñez, C. L., Lory, S., et al. (2006) A

virulence locus of Pseudomonas aeruginosa encodes a protein secretion apparatus. Science **312**, 1526–1530.

64 Dudley, E. G., Thomson, N. R., Parkhill, J., Morin, N. P. and Nataro, J. P. (2006) Proteomic and microarray characterization of the AggR regulon identifies a pheU pathogenicity island in enteroaggregative Escherichia coli. Mol. Microbiol. **61**, 1267–1282.

65 Wu, H.-Y., Chung, P.-C., Shih, H.-W., Wen, S.-R. and Lai, E.-M. (2008) Secretome analysis uncovers an Hcp-family protein secreted via a type VI secretion system in Agrobacterium tumefaciens. J. Bacteriol. **190**, 2841–2850.

66 Bartonickova, L., Sterzenbach, T., Nell, S., Kops, F., Schulze, J., Venzke, A., Brenneke, B., Bader, S., Gruber, A. D., Suerbaum, S., et al. (2013) Hcp and VgrG1 are secreted components of the Helicobacter hepaticustype VI secretion system and VgrG1 increases the bacterial colitogenic potential. Cellular Microbiology **15**, 992–1011.

67 Pallen, M., Chaudhuri, R. and Khan, A. (2002) Bacterial FHA domains: neglected players in the phospho-threonine signalling game? Trends in Microbiology **10**, 556–563.

68 Schlieker, C., Zentgraf, H., Dersch, P. and Mogk, A. (2005) ClpV, a unique Hsp100/Clp member of pathogenic proteobacteria. Biol. Chem. **386**, 1115–1127.

69 Cascales, E. (2008) The type VI secretion toolkit. EMBO Rep **9**, 735–741.

70 Records, A. R. (2011) The type VI secretion system: a multipurpose delivery system with a phage-like machinery. Mol. Plant Microbe Interact. **24**, 751–757.

71 Kanamaru, S. (2009) Structural similarity of tailed phages and pathogenic bacterial secretion systems. Proc. Natl. Acad. Sci. U.S.A. **106**, 4067–4068.

72 Chatterjee, S. N. and Chaudhuri, K. (2011) Outer Membrane Vesicles of Bacteria which are internalised by intestinal epithelial cells. FEBS letters. **585**, 1357-1362.

73 Ho, B. T., Dong, T. G. and Mekalanos, J. J. (2014) A view to a kill: the bacterial type VI secretion system. Cell Host Microbe **15**, 9–21.

74 Felisberto-Rodrigues, C., Durand, E., Aschtgen, M.-S., Blangy, S., Ortiz-Lombardia, M., Douzi, B., Cambillau, C. and Cascales, E. (2011) Towards a structural comprehension of bacterial type VI secretion systems: characterization of the TssJ-TssM complex of an Escherichia coli pathovar. PLoS Pathog. **7**, e1002386.

75 Boyer, F., Fichant, G., Berthod, J., Vandenbrouck, Y. and Attree, I. (2009) Dissecting the bacterial type VI secretion system by a genome wide in silico analysis: what can be learned from available microbial genomic resources? BMC Genomics **10**, 104.

76 Zheng, J., Ho, B. and Mekalanos, J. J. (2011) Genetic analysis of anti-amoebae and anti-bacterial activities of the type VI secretion system in Vibrio cholerae. PLoS ONE **6**, e23876.

77 Zheng, J. and Leung, K. Y. (2007) Dissection of a type VI secretion system in Edwardsiella tarda. Mol. Microbiol. **66**, 1192–1206.

78 Silverman, J. M., Brunet, Y. R., Cascales, E. and Mougous, J. D. (2012) Structure and regulation of the type VI secretion system. Annu. Rev. Microbiol. **66**, 453–472.

79 Ruiz, F. M., Santillana, E., Spínola-Amilibia, M., Torreira, E., Culebras, E. and Romero, A. (2015) Correction: Crystal Structure of Hcp from Acinetobacter baumannii: A Component of the Type VI Secretion System. PLoS ONE **10**, e0136978.

80 Galindo, C. L., Rosenzweig, J. A., Kirtley, M. L. and Chopra, A. K. (2011) Pathogenesis of Y. enterocolitica and Y. pseudotuberculosis in Human Yersiniosis. J Pathog **2011**, 182051.

81 Schroeder, G. N. and Hilbi, H. (2008) Molecular pathogenesis of Shigella spp.: controlling host cell signaling, invasion, and death by type III secretion. Clin. Microbiol. Rev. **21**, 134–156.

82 Agbor, T. A. and McCormick, B. A. (2011) Salmonella effectors: important players modulating host cell function during infection. Cellular Microbiology **13**, 1858–1869.

83 Dean, P. (2011) Functional domains and motifs of bacterial type III effector proteins and their roles in infection. FEMS Microbiol. Rev. **35**, 1100–1125.

84 Wong, A. R. C., Pearson, J. S., Bright, M. D., Munera, D., Robinson, K. S., Lee, S. F., Frankel, G. and Hartland, E. L. (2011) Enteropathogenic and enterohaemorrhagic Escherichia coli: even more subversive elements. Mol. Microbiol. **80**, 1420–1438.

85 Bush, K., Courvalin, P., Dantas, G., Davies, J., Eisenstein, B., Huovinen, P., Jacoby, G. A., Kishony, R., Kreiswirth, B. N., Kutter, E., et al. (2011) Tackling antibiotic resistance. Nat. Rev. Microbiol. **9**, 894–896.

86 Trosky, J. E., Liverman, A. and Orth, K. (2008) Yersinia outer proteins: Yops. Cellular Microbiology **10**, 557–565.

87 Sample, A. K., Fowler, J. M. and Brubaker, R. R. (1987) Modulation of the low-calcium response in Yersinia pestis via plasmid-plasmid interaction. Microb. Pathog. **2**, 443–453.

88 Mehigh, R. J., Sample, A. K. and Brubaker, R. R. (1989) Expression of the low calcium response in Yersinia pestis. Microb. Pathog. **6**, 203–217.

89 Michiels, T., Wattiau, P. and Brasseur, R. (1990) Secretion of Yop proteins by Yersiniae. Infection and Immunity. **58**, 2840-2849.

90 Straley, S. C., Plano, G. V., Skrzypek, E., Haddix, P. L. and Fields, K. A. (1993) Regulation by Ca2+ in the Yersinia low-Ca2+ response. Mol. Microbiol. **8**, 1005–1010.

91 Koster, M., Bitter, W., de Cock, H., Allaoui, A., Cornelis, G. R. and Tommassen, J. (1997) The outer membrane component, YscC, of the Yop secretion machinery of Yersinia enterocolitica forms a ring-shaped multimeric complex. Mol. Microbiol. **26**, 789–797.

92 Diepold, A., Amstutz, M., Abel, S., Sorg, I., Jenal, U. and Cornelis, G. R. (2010) Deciphering the assembly of the Yersinia type III secretion injectisome. EMBO J. **29**, 1928–1940.

93 Spreter, T., Yip, C. K., Sanowar, S., André, I., Kimbrough, T. G., Vuckovic, M., Pfuetzner, R. A., Deng, W., Yu, A. C., Finlay, B. B., et al. (2009) A conserved structural motif mediates formation of the periplasmic rings in the type III secretion system. Nat. Struct. Mol. Biol. **16**, 468–476.

94 Ross, J. A. and Plano, G. V. (2011) A C-terminal region of Yersinia pestis YscD binds the outer membrane secretin YscC. J. Bacteriol. **193**, 2276–2289.

95 Yip, C. K., Kimbrough, T. G., Felise, H. B., Vuckovic, M., Thomas, N. A., Pfuetzner, R. A., Frey, E. A., Brett Finlay, B., Miller, S. I. and Strynadka, N. C. J. (2005) Structural characterization of the molecular platform for type III secretion system assembly. Nature **435**, 702–707.

96 Hodgkinson, J. L., Horsley, A., Stabat, D. and Simon, M. (2009) Three-dimensional reconstruction of the Shigella T3SS transmembrane regions reveals 12-fold symmetry and novel features throughout. Nature structural & molecular biology. **16**, 477-85.

97 Dewoody, R. S. and Merritt, P. M. (2013) Regulation of the Yersinia type III secretion system: traffic control. Frontiers in cellular and infection microbiology. **3**: 4.

98 Allaoui, A., Woestyn, S., Sluiters, C. and Cornelis, G. R. (1994) YscU, a Yersinia enterocolitica inner membrane protein involved in Yop secretion. Journal of ….

99 Fields, K. A., Plano, G. V. and Straley, S. C. (1994) A low-Ca2+ response (LCR) secretion (ysc) locus lies within the lcrB region of the LCR plasmid in Yersinia pestis. J. Bacteriol. **176**, 569-79.

100 Minamino, T., Iino, T. and Kutuskake, K. (1994) Molecular characterization of the Salmonella typhimurium flhB operon and its protein products. J. Bacteriol. **176**, 7630–7637.

101 Creasey, E. A., Delahay, R. M., Daniell, S. J. and Frankel, G. (2003) Yeast two-hybrid system survey of interactions between LEE-encoded proteins of enteropathogenic Escherichia coli. Microbiology (Reading, Engl.) **149**, 2093–2106.

102 Melén, K., Krogh, A. and Heijne, von, G. (2003) Reliability measures for membrane protein topology prediction algorithms. J. Mol. Biol. **327**, 735–744.

103 Ghosh, P. (2004) Process of protein transport by the type III secretion system. Microbiology and molecular biology reviews. **62**, 379-433.

104 Berger, C., Robin, G. P., Bonas, U. and Koebnik, R. (2010) Membrane topology of conserved components of the type III secretion system from the plant pathogen Xanthomonas campestris pv. vesicatoria. Microbiology (Reading, Engl.) **156**, 1963–1974.

105 Diepold, A., Wiesand, U. and Cornelis, G. R. (2011) The assembly of the export apparatus (YscR,S,T,U,V) of the Yersinia type III secretion apparatus occurs independently of other structural components and involves the formation of an YscV oligomer. Mol. Microbiol. **82**, 502–514.

106 Day, J. B. and Plano, G. V. (2000) The Yersinia pestis YscY protein directly binds YscX, a secreted component of the type III secretion machinery. J. Bacteriol. **182**, 1834–1843.

107 Blaylock, B., Berube, B. J. and Schneewind, O. (2010) YopR impacts type III needle polymerization in Yersinia species. Mol. Microbiol. **75**, 221–229.

108 Agrain, C., Sorg, I. and Paroz, C. (2005) Secretion of YscP from Yersinia enterocolitica is essential to control the length of the injectisome needle but not to change the type III secretion substrate specificity. Mol. Microbiol.

109 Payne, P. L. and Straley, S. C. (1998) YscO of Yersinia pestis is a mobile core component of the Yop secretion system. J. Bacteriol. **180**, 3882–3890.

110 Payne, P. L. and Straley, S. C. (1999) YscP of Yersinia pestis is a secreted component of the Yop secretion system. J. Bacteriol. **181**, 2852–2862.

111 Wood, S. E., Jin, J. and Lloyd, S. A. (2008) YscP and YscU switch the substrate specificity of the Yersinia type III secretion system by regulating export of the inner rod protein YscI. J. Bacteriol. **190**, 4252-62.

112 Marlovits, T. C., Kubori, T., Sukhan, A., Thomas, D. R., Galán, J. E. and Unger, V. M. (2004) Structural insights into the assembly of the type III secretion needle complex. Science **306**, 1040–1042.

113 Blocker, A., Jouihri, N., Larquet, E., Gounon, P., Ebel, F., Parsot, C., Sansonetti, P. and Allaoui, A. (2001) Structure and composition of the Shigella flexneri "needle complex," a part of its type III secreton. Mol. Microbiol. **39**, 652–663.

114 Hoiczyk, E. and Blobel, G. (2001) Polymerization of a single protein of the pathogen Yersinia enterocolitica into needles punctures eukaryotic cells. Proc. Natl. Acad. Sci. U.S.A. **98**, 4669–4674.

115 Journet, L., Agrain, C., Broz, P. and Cornelis, G. R. (2003) The needle length of bacterial injectisomes is determined by a molecular ruler. Science **302**, 1757–1760.

116 Kubori, T., Matsushima, Y., Nakamura, D., Uralil, J., Lara-Tejero, M., Sukhan, A., Galán, J. E. and Aizawa, S. I. (1998) Supramolecular structure of the Salmonella typhimurium type III protein secretion system. Science. **280**, 602–605.

117 Allaoui, A., Schulte, R. and Cornelis, G. R. (1995) Mutational analysis of the Yersinia enterocolitica virC operon: characterization of yscE, F, G, I, J, K required for Yop secretion and yscH encoding YopR - Allaoui (2004). Molecular Microbiology. **18**, 343-355.

118 Lee, V. T. and Schneewind, O. (1999) Type III machines of pathogenic yersiniae secrete virulence factors into the extracellular milieu. Mol. Microbiol. **31**, 1619–1629.

119 Mueller, C. A., Broz, P., Müller, S. A., Ringler, P., Erne-Brand, F., Sorg, I., Kuhn, M., Engel, A. and Cornelis, G. R. (2005) The V-antigen of Yersinia forms a distinct structure at the tip of injectisome needles. Science **310**, 674–676.

120 Costa, T. R. D., Amer, A. A. A., Farag, S. I., Wolf-Watz, H., Fällman, M., Fahlgren, A., Edgren, T. and Francis, M. S. (2013) Type III secretion translocon assemblies that attenuate Yersinia virulence. Cellular Microbiology **15**, 1088–1110.

121 Schubot FD, Jackson MW, Penrose KJ, et al. Three-dimensional structure of a macromolecular assembly that regulates type III secretion in Yersinia pestis. (2005). Journal of Molecular Biology. **346**, 1147–1161.

122 Kleiner, M., Young, J. C., Shah, M., VerBerkmoes, N. C. and Dubilier, N. (2013) Metaproteomics reveals abundant transposase expression in mutualistic endosymbionts. MBio **4**, e00223–13.

123 Du, D., Wang, Z., James, N. R., Voss, J. E., Klimont, E., Ohene-Agyei, T., Venter, H., Chiu, W. and Luisi, B. F. (2014) Structure of the AcrAB-TolC multidrug efflux pump. Nature **509**, 512–515.

124 Mikolosko, J., Bobyk, K., Zgurskaya, H. I. and Ghosh, P. (2006) Conformational flexibility in the multidrug efflux system protein AcrA. Structure **14**, 577–587.

125 Pei, X.-Y., Hinchliffe, P., Symmons, M. F., Koronakis, E., Benz, R., Hughes, C. and Koronakis, V. (2011) Structures of sequential open states in a symmetrical opening transition of the TolC exit duct. Proc. Natl. Acad. Sci. U.S.A. **108**, 2112–2117.

126 Lu, C., Turley, S., Marionni, S. T., Park, Y.-J., Lee, K. K., Patrick, M., Shah, R.,

Sandkvist, M., Bush, M. F. and Hol, W. G. J. (2013) Hexamers of the type II secretion ATPase GspE from Vibrio cholerae with increased ATPase activity. Structure **21**, 1707–1717.

127 Korotkov, K. V., Johnson, T. L., Jobling, M. G., Pruneda, J., Pardon, E., Héroux, A., Turley, S., Steyaert, J., Holmes, R. K., Sandkvist, M., et al. (2011) Structural and functional studies on the interaction of GspC and GspD in the type II secretion system. PLoS Pathog. **7**, e1002228.

128 Abendroth, J., Mitchell, D. D., Korotkov, K. V., Johnson, T. L., Kreger, A., Sandkvist, M. and Hol, W. G. J. (2009) The three-dimensional structure of the cytoplasmic domains of EpsF from the type 2 secretion system of Vibrio cholerae. J. Struct. Biol. **166**, 303–315.

129 Abendroth, J., Kreger, A. C. and Hol, W. G. J. (2009) The dimer formed by the periplasmic domain of EpsL from the Type 2 Secretion System of Vibrio parahaemolyticus. J. Struct. Biol. **168**, 313–322.

130 Abendroth, J., Murphy, P., Sandkvist, M., Bagdasarian, M. and Hol, W. G. J. (2005) The X-ray structure of the type II secretion system complex formed by the N-terminal domain of EpsE and the cytoplasmic domain of EpsL of Vibrio cholerae. J. Mol. Biol. **348**, 845–855.

131 Abendroth, J., Rice, A. E., McLuskey, K., Bagdasarian, M. and Hol, W. G. J. (2004) The crystal structure of the periplasmic domain of the type II secretion system protein EpsM from Vibrio cholerae: the simplest version of the ferredoxin fold. J. Mol. Biol. **338**, 585–596.

132 Korotkov, K. V., Gray, M. D., Kreger, A., Turley, S., Sandkvist, M. and Hol, W. G. J. (2009) Calcium is essential for the major pseudopilin in the type 2 secretion system. J. Biol. Chem. **284**, 25466–25470.

133 Raghunathan, K., Vago, F. S., Grindem, D., Ball, T., Wedemeyer, W. J., Bagdasarian, M. and Arvidson, D. N. (2014) The 1.59Å resolution structure of the minor pseudopilin EpsH of Vibrio cholerae reveals a long flexible loop. Biochim. Biophys. Acta **1844**, 406–415.

134 Korotkov, K. V. and Hol, W. G. J. (2008) Structure of the GspK-GspI-GspJ complex from the enterotoxigenic Escherichia coli type 2 secretion system. Nat. Struct. Mol. Biol. **15**, 462–468.

135 Korotkov, K. V., Pardon, E., Steyaert, J. and Hol, W. G. J. (2009) Crystal structure of the N-terminal domain of the secretin GspD from ETEC determined with the assistance of a nanobody. Structure. **17**, 255–265.

136 Korotkov, K. V. and Hol, W. G. J. (2013) Crystal structure of the pilotin from the enterohemorrhagic Escherichia coli type II secretion system. J. Struct. Biol. **182**, 186–191.

137 Gamez, A., Mukerjea, R., Alayyoubi, M., Ghassemian, M. and Ghosh, P. (2012) Structure and interactions of the cytoplasmic domain of the Yersinia type III secretion protein YscD. J. Bacteriol. **194**, 5949–5958.

138 Wiesand, U., Sorg, I., Amstutz, M., Wagner, S., van den Heuvel, J., Lührs, T., Cornelis, G. R. and Heinz, D. W. (2009) Structure of the type III secretion recognition protein YscU from Yersinia enterocolitica. J. Mol. Biol. **385**, 854–866.

139 Sun, P., Tropea, J. E., Austin, B. P., Cherry, S. and Waugh, D. S. (2008) Structural characterization of the Yersinia pestis type III secretion system needle protein

YscF in complex with its heterodimeric chaperone YscE/YscG. J. Mol. Biol. **377**, 819–830.

140 Schubot, F. D., Cherry, S., Austin, B. P., Tropea, J. E. and Waugh, D. S. (2005) Crystal structure of the protease-resistant core domain of Yersinia pestis virulence factor YopR. Protein Sci. **14**, 1679–1683.

141 Derewenda, U., Mateja, A., Devedjiev, Y., Routzahn, K. M., Evdokimov, A. G., Derewenda, Z. S. and Waugh, D. S. (2004) The structure of Yersinia pestis V-antigen, an essential virulence factor and mediator of immunity against plague. Structure **12**, 301–306.

142 Schreiner, M. and Niemann, H. H. (2012) Crystal structure of the Yersinia enterocolitica type III secretion chaperone SycD in complex with a peptide of the minor translocator YopD. BMC Struct Biol **12**, 13.

143 Hare, S., Bayliss, R., Baron, C. and Waksman, G. (2006) A large domain swap in the VirB11 ATPase of Brucella suis leaves the hexameric assembly intact. J. Mol. Biol. **360**, 56–66.

144 Smith, M. A., Coinçon, M., Paschos, A., Jolicoeur, B., Lavallée, P., Sygusch, J. and Baron, C. (2012) Identification of the binding site of Brucella VirB8 interaction inhibitors. Chem. Biol. **19**, 1041–1048.

145 Chandran, V., Fronzes, R., Duquerroy, S., Cronin, N., Navaza, J. and Waksman, G. (2009) Structure of the outer membrane complex of a type IV secretion system. Nature **462**, 1011–1015.

146 Rivera-Calzada, A., Fronzes, R., Savva, C. G., Chandran, V., Lian, P. W., Laeremans, T., Pardon, E., Steyaert, J., Remaut, H., Waksman, G., et al. (2013) Structure of a bacterial type IV secretion core complex at subnanometre resolution. EMBO J. **32**, 1195–1204.

147 Durand, E., Zoued, A., Spinelli, S., Watson, P. J. H., Aschtgen, M.S., Journet, L., Cambillau, C. and Cascales, E. (2012) Structural characterization and oligomerization of the TssL protein, a component shared by bacterial type VI and type IVb secretion systems. J. Biol. Chem. **287**, 14157–14168.

148 Pietrosiuk, A., Lenherr, E. D., Falk, S., Bönemann, G., Kopp, J., Zentgraf, H., Sinning, I. and Mogk, A. (2011) Molecular basis for the unique role of the AAA+ chaperone ClpV in type VI protein secretion. J. Biol. Chem. **286**, 30010–30021.

149 Kudryashev, M., Wang, R. Y.-R., Brackmann, M., Scherer, S., Maier, T., Baker, D., DiMaio, F., Stahlberg, H., Egelman, E. H. and Basler, M. (2015) Structure of the type VI secretion system contractile sheath. Cell **160**, 952–962.

150 Shneider, M. M., Buth, S. A., Ho, B. T., Basler, M., Mekalanos, J. J. and Leiman, P. G. (2013) PAAR-repeat proteins sharpen and diversify the type VI secretion system spike. Nature **500**, 350–353.

151 Button, J. E. and Galán, J. E. (2011) Regulation of chaperone/effector complex synthesis in a bacterial type III secretion system. Mol. Microbiol. **81**, 1474–1483.

152 Feldman, M. F. and Cornelis, G. R. (2003) The multitalented type III chaperones: all you can do with 15 kDa. FEMS Microbiol. Lett. **219**, 151–158.

153 Parsot, C., Hamiaux, C. and Page, A.-L. (2003) The various and varying roles of specific chaperones in type III secretion systems. Curr. Opin. Microbiol. **6**, 7–14.

154 Wilharm, G., Dittmann, S. and Schmid, A. (2007) On the role of specific

chaperones, the specific ATPase, and the proton motive force in type III secretion. International journal of medical microbiology. **297**, 27-36.

155 Trame, C. B. and McKay, D. B. (2003) Structure of the Yersinia enterocolitica molecular-chaperone protein SycE. Acta Crystallogr. D Biol. Crystallogr. **59**, 389–392.

156 Phan, J., Tropea, J. E. and Waugh, D. S. (2004) Structure of the Yersinia pestis type III secretion chaperone SycH in complex with a stable fragment of YscM2. Acta Crystallogr. D Biol. Crystallogr. **60**, 1591–1599.

157 Schubot, F. D., Jackson, M. W., Penrose, K. J., Cherry, S., Tropea, J. E., Plano, G. V. and Waugh, D. S. (2005) Three-dimensional structure of a macromolecular assembly that regulates type III secretion in Yersinia pestis. J. Mol. Biol. **346**, 1147–1161.

158 Locher, M., Lehnert, B., Krauss, K., Heesemann, J., Groll, M. and Wilharm, G. (2005) Crystal structure of the Yersinia enterocolitica type III secretion chaperone SycT. J. Biol. Chem. **280**, 31149–31155.

159 Büttner, C. R., Cornelis, G. R., Heinz, D. W. and Niemann, H. H. (2005) Crystal structure of Yersinia enterocolitica type III secretion chaperone SycT. Protein Sci. **14**, 1993–2002.

160 Luo, Y., Bertero, M. G., Frey, E. A., Pfuetzner, R. A., Wenk, M. R., Creagh, L., Marcus, S. L., Lim, D., Sicheri, F., Kay, C., et al. (2001) Structural and biochemical characterization of the type III secretion chaperones CesT and SigE. Nat. Struct. Biol. **8**, 1031–1036.

161 Johnson, S., Deane, J. E. and Lea, S. M. (2005) The type III needle and the damage done. Curr. Opin. Struct. Biol. **15**, 700–707.

162 Birtalan, S. C., Phillips, R. M. and Ghosh, P. (2002) Three-dimensional secretion signals in chaperone-effector complexes of bacterial pathogens. Mol. Cell **9**, 971–980.

163 Stebbins, C. E. and Galán, J. E. (2001) Maintenance of an unfolded polypeptide by a cognate chaperone in bacterial type III secretion. Nature **414**, 77–81.

164 Birtalan, S. and Ghosh, P. (2001) Structure of the Yersinia type III secretory system chaperone SycE. Nat. Struct. Biol. **8**, 974–978.

165 Costa, S. C. P., Schmitz, A. M., Jahufar, F. F., Boyd, J. D., Cho, M. Y., Glicksman, M. A. and Lesser, C. F. (2012) A new means to identify type 3 secreted effectors: functionally interchangeable class IB chaperones recognize a conserved sequence. MBio **3**(1), e00243-11.

166 Job, V., Matteï, P.-J., Lemaire, D., Attree, I. and Dessen, A. (2010) Structural basis of chaperone recognition of type III secretion system minor translocator proteins. J. Biol. Chem. **285**, 23224–23232.

167 Lunelli, M., Lokareddy, R. K., Zychlinsky, A. and Kolbe, M. (2009) IpaB-IpgC interaction defines binding motif for type III secretion translocator. Proc. Natl. Acad. Sci. U.S.A. **106**, 9661–9666.

168 Büttner, C. R., Sorg, I., Cornelis, G. R., Heinz, D. W. and Niemann, H. H. (2008) Structure of the Yersinia enterocolitica type III secretion translocator chaperone SycD. J. Mol. Biol. **375**, 997–1012.

169 Barta, M. L., Zhang, L., Picking, W. L. and Geisbrecht, B. V. (2010) Evidence for alternative quaternary structure in a bacterial Type III secretion system chaperone. BMC Struct Biol **10**, 21.

170 Blatch, G. L. and Lässle, M. (1999) The tetratricopeptide repeat: a structural motif mediating protein-protein interactions. Bioessays. **21**, 932-9.

171 Das, A. K., Cohen, P. and Barford, D. (1998) The structure of the tetratricopeptide repeats of protein phosphatase 5: implications for TPR-mediated protein–protein interactions. EMBO J. **17**, 1192-1199.

172 D'Andrea, L. D. and Regan, L. (2003) TPR proteins: the versatile helix. Trends in biochemical sciences. **28**, 655-662.

173 Quinaud, M., Plé, S., Job, V., Contreras-Martel, C., Simorre, J.-P., Attree, I. and Dessen, A. (2007) Structure of the heterotrimeric complex that regulates type III secretion needle formation. Proc. Natl. Acad. Sci. U.S.A. **104**, 7803–7808.

174 Tan, Y. W., Yu, H. B., Sivaraman, J., Leung, K. Y. and Mok, Y.-K. (2009) Mapping of the chaperone AcrH binding regions of translocators AopB and AopD and characterization of oligomeric and metastable AcrH-AopB-AopD complexes in the type III secretion system of Aeromonas hydrophila. Protein Sci. **18**, 1724–1734.

175 Adam, P. R., Patil, M. K., Dickenson, N. E., Choudhari, S., Barta, M., Geisbrecht, B. V., Picking, W. L. and Picking, W. D. (2012) Binding affects the tertiary and quaternary structures of the Shigella translocator protein IpaB and its chaperone IpgC. Biochemistry **51**, 4062–4071.

176 Lokareddy, R. K., Lunelli, M., Eilers, B., Wolter, V. and Kolbe, M. (2010) Combination of two separate binding domains defines stoichiometry between type III secretion system chaperone IpgC and translocator protein IpaB. J. Biol. Chem. **285**, 39965–39975.

177 Quinaud, M., Chabert, J., Faudry, E., Neumann, E., Lemaire, D., Pastor, A., Elsen, S., Dessen, A. and Attree, I. (2005) The PscE-PscF-PscG complex controls type III secretion needle biogenesis in Pseudomonas aeruginosa. J. Biol. Chem. **280**, 36293–36300.

178 Miroux, B. and Walker, J. E. (1996) Over-production of proteins in Escherichia coli: mutant hosts that allow synthesis of some membrane proteins and globular proteins at high levels. J. Mol. Biol. **260**, 289–298.

179 Dumon-Seignovert, L., Cariot, G. and Vuillard, L. (2004) The toxicity of recombinant proteins in Escherichia coli: a comparison of overexpression in BL21(DE3), C41(DE3), and C43(DE3). Protein Expr. Purif. **37**, 203–206.

180 Studier, F. W. (2005) Protein production by auto-induction in high density shaking cultures. Protein Expr. Purif. **41**, 207–234.

181 Sambrook, J. and Russell, D. W. (1989) SDS-polyacrylamide gel electrophoresis of proteins. Molecular cloning: a laboratory manual, Third edition. Cold Spring Harbor Laboratory Press.

182 Laemmli, U. K. (1970) Cleavage of structural proteins during the assembly of the head of bacteriophage T4. Nature. **227**, 680-685.

183 Gill, S. C. and Hippel, von, P. H. (1989) Calculation of protein extinction coefficients from amino acid sequence data. Anal. Biochem. **182**, 319–326.

184 Scott, D. J., Harding, S. E. and Rowe, A. J. (2005) Analytical Ultracentrifugation, Royal Society of Chemistry.

185 Dynamic Light Scattering: an Important Tool for Protein Crystallography and Nanotechnology, Viscotek Europe Ltd. Available from: <http://www.chemeurope.com>.[3 September 2015].

186 Dynamic light scattering (DLS) for particle size characterization of proteins, Malvern Instruments Ltd. Available from: <http://www.malvern.com>. [4 September 2015].

187 ISA - ASTRID2 and the Rosetta Mission, Aarhus University. Available from: <http://www.isa.au.dk >.[5 September 2015].

188 Gore, M. G. (2000) Spectrophotometry and Spectrofluorimetry, Oxford University Press.

189 Greenfield, N. J. (2006) Using circular dichroism spectra to estimate protein secondary structure. Nat Protoc **1**, 2876–2890.

190 Principles of fluorescence, Edinburgh Super-resolution Imaging Consortium. Available from: <http://www.esric.org/education/fluorescence>. [5 September 2015].

191 Creighton, T. E. (1997) Protein Function: A Practical Approach, Second edition. Oxford University Press.

192 Fluorescence Spectroscopy, University of Warwick Business Facilities - Analytical Equipment. Available from: <http://www2.warwick.ac.uk/services/ris/business/analyticalguide/fluorescence>. [5 September 2015].

193 Privalov, P. L., Gill, S. J. (1988) Stability of Protein Structure. Adv. Protein Chem. **39**, 191-234.

194 Wilkins, M. R., Gasteiger, E., Bairoch, A., Sanchez, J. C., Williams, K. L., Appel, R. D. and Hochstrasser, D. F. (1999) Protein identification and analysis tools in the ExPASy server. Methods Mol. Biol. **112**, 531–552.

195 Walters, J., Milam, S. L. and Clark, A. C. (2009) Practical approaches to protein folding and assembly: spectroscopic strategies in thermodynamics and kinetics. Meth. Enzymol. **455**, 1–39.

196 Pace, C. N. (1986) Determination and analysis of urea and guanidine hydrochloride denaturation curves. Meth. Enzymol. **131**, 266–280.

197 Tanford, C. (1970) Protein denaturation. C. Theoretical models for the mechanism of denaturation. Adv. Protein Chem. **24**, 1–95.

198 Truhlar, S. M. E., Torpey, J. W. and Komives, E. A. (2006) Regions of IkappaBalpha that are critical for its inhibition of NF-kappaB.DNA interaction fold upon binding to NF-kappaB. Proc. Natl. Acad. Sci. U.S.A. **103**, 18951–18956.

199 O'Dea, E. L., Barken, D., Peralta, R. Q., Tran, K. T., Werner, S. L., Kearns, J. D., Levchenko, A. and Hoffmann, A. (2007) A homeostatic model of IkappaB metabolism to control constitutive NF-kappaB activity. Mol. Syst. Biol. **3**, 111.

200 Deu, E. and Kirsch, J. F. (2007) The unfolding pathway for Apo Escherichia coli aspartate aminotransferase is dependent on the choice of denaturant. Biochemistry **46**, 5810–5818.

201 Doyle, S. M., Braswell, E. H. and Teschke, C. M. (2000) SecA folds via a dimeric intermediate. Biochemistry **39**, 11667–11676.

202 Main, E. R. G., Lowe, A. R., Mochrie, S. G. J., Jackson, S. E. and Regan, L. (2005) A recurring theme in protein engineering: the design, stability and folding of repeat proteins. Curr. Opin. Struct. Biol. **15**, 464–471.

203 Main, E. R. G., Jackson, S. E. and Regan, L. (2003) The folding and design of repeat proteins: reaching a consensus. Curr. Opin. Struct. Biol. **13**, 482–489.

204 Phillips, J. J., Javadi, Y., Millership, C. and Main, E. R. G. (2012) Modulation of the multistate folding of designed TPR proteins through intrinsic and extrinsic factors. Protein Sci. **21**, 327–338.

205 Javadi, Y. and Main, E. R. G. (2009) Exploring the folding energy landscape of a series of designed consensus tetratricopeptide repeat proteins. Proc. Natl. Acad. Sci. U.S.A. **106**, 17383–17388.

206 Main, E. R. G., Stott, K., Jackson, S. E. and Regan, L. (2005) Local and long-range stability in tandemly arrayed tetratricopeptide repeats. Proc. Natl. Acad. Sci. U.S.A. **102**, 5721–5726.

207 Cohn, S. K. (2008) 4 Epidemiology of the Black Death and Successive Waves of Plague. Medical History, Cambridge University Press **52**, 74–100.

208 Matsumoto, H. and Young, G. M. (2009) Translocated effectors of Yersinia. Curr. Opin. Microbiol. **12**, 94–100.

209 Gong, H., Vu, G.-P., Bai, Y., Yang, E., Liu, F. and Lu, S. (2010) Differential expression of Salmonella type III secretion system factors InvJ, PrgJ, SipC, SipD, SopA and SopB in cultures and in mice. Microbiology (Reading, England) **156**, 116–127.

210 Smith, R. D. and Coast, J. (2002) Antimicrobial resistance: a global response. Bull. World Health Organization. **80**, 126–133.

211 Anthony King & ChemistryWorld, Antibiotic resistance will kill 300 million people by 2050. Available from: <www.scientificamerican.com>.[2 September 2015].

212 Cliff, M. J., Williams, M. A., Brooke-Smith, J., Barford, D. and Ladbury, J. E. (2005) Molecular recognition via coupled folding and binding in a TPR domain. J. Mol. Biol. **346**, 717–732.

213 Lamboy, J. A., Kim, H., Lee, K. S. and Ha, T. (2011) Visualization of the nanospring dynamics of the IκBα ankyrin repeat domain in real time.